On Pattern-Switching Phenomena in Complex Elastic Structures

A thesis submitted to the University of Manchester for the degree of

Doctor of Philosophy

in the Faculty of Engineering and Physical Sciences

2012

Stephen Willshaw

School of Physics and Astronomy

Contents

wordcount: 27175

List of Tables

List of Figures

Abstract

We investigate global pattern-switching effects in 2D cellular solids in which the voids are arranged in a square lattice. Uniaxial compression of these structures triggers an elastic instability which brings about a period-doubling transformation of the void shapes at a critical strain ϵ_{cr}. Specifically, a square array of circular voids forms a pattern of mutually orthogonal ellipses and a similar effect is observed for diamond-shaped voids. The onset of instability is governed by the *void fraction* Φ and size-effects are found for the experimental samples. We establish empirical laws ($\epsilon_{cr} \propto (\Phi_{max} - \Phi)^2$, for example) which characterise the stiffness, strength and stability of cellular structures comprising square arrays of circular voids. A comparison of these with predictions from a discrete model implies underestimation of the resistance of the lattice to buckling, although the size effects are replicated. We find similar pattern-switching effects in the *cubic lattice*, which is a three-dimensional porous cube. The effect of buckling in this system is to produce a 2D pattern in one plane of voids. In two-phase *granular crystals*, rearrangement of a square lattice of particles results in a new, period-doubled, structural pattern. This switch can occur via an intermediate phase depending on the size ratio of the particles as shown in experiments and numerical simulations.

Declaration

No portion of the work referred to in this thesis has been submitted in support of an application for another degree or qualification of this or any other university or other institution of learning.

Stephen Willshaw
School of Physics and Astronomy
University of Manchester
Oxford Road
Manchester
M13 9PL
March 2012

Copyright

The Author

The author attended James Gillespie's High School, Edinburgh, between 1997 and 2003. This was followed by undergraduate study at the University of Manchester and the Freie Universität, Berlin en route to obtaining a first class MPhys degree entitled Physics with Study in Europe. The work presented in this thesis was undertaken in the period October 2008 to March 2012 under the supervision of Professor Tom Mullin at the University of Manchester.

Acknowledgements

There are an unfathomable number of people who have helped me through the course of my PhD. Tom, thank you for giving me this project and providing your expert advice and support throughout. I have learned a lot from you in the last three and a half years and I hope this has not been just a one way process! Thanks go to Andrew, Katia, Pedro, Fatih, Carl, Draga, Anne, Paul and Gyorgy for the discussions, collaborations and conversations. It has been a great privilege and pleasure to work with such clever people and I hope I've helped you in some way too. Thanks of course to João Fonseca for the Instron machine, without which I would not be writing this. A special mention goes to Paul Tip and Stuart Morse for their technical support, especially in my formative days when I was intent on breaking everything.

The LMC and Jazzy Paddy, lunch with you has been a highlight of the past eight years or so. Our chats have always made me smile and l hope our friendship lasts a long, long time. Finn, drinking tea is always more fun when you are talking rubbish with someone. Keep up the good work and the positive attitude and you'll be reet. My great friends Nick, TKB, Tomos, Claudia, Roland, Rob, Ben Moore (WoWoWo), Claire and Rowlands, you have reminded me that there is an outside world and put up with all of my

blabbering/blubbering. Isabel, Sal, Ian, Gavin and Chris aka My Family, I can only tell you how fantastic you are for being there at all times. To everyone above, I seriously, seriously appreciate everything you have done for me. I look up to you all.

There are two special people I feel deserve their own paragraph here. Dad, I cannot thank you enough for all of the help you have given me, not just in the past couple of months but throughout my education. You are an inspiration to your boys and if I turn out half as clever as you, I'll know I've succeeded in life. I could never end this section without mentioning my wonderful girlfriend, Nicole. You have put up with so much - so many sleepless nights, lost evenings and weekends, infuriating one-track conversations and, despite this, kept me sane and I can't thank you enough. I love you B, and I look forward to our adventures together.

Chapter 1

Introduction

The results of experimental investigations into the response of complex elastic structures to compression are presented in this thesis. The ideas which have inspired this work are highlighted here, and this is followed by an overview of the subsequent chapters.

1.1 Cellular Structures

One of the simplest, and indeed most powerful, approaches to scientific research is to first develop an understanding of naturally-made physical systems and then use this knowledge to drive innovation. Research into *cellular solids*, which comprise a network of enclosed spaces separated by material boundaries, provides an excellent test case for this approach. There are, for example, interesting similarities between the polystyrene foam used to minimise heat loss in a take-away coffee cup and the complex network of struts and nodes which make up cancellous bone [3].

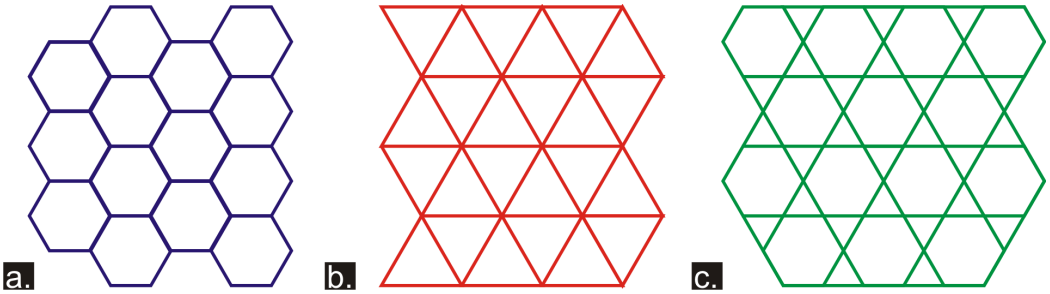

Figure 1.1: Examples of regular 2D cellular structures. The hexagonal (a), triangular (b) and Kagomé (c) lattices have been the basis of a range of experimental and numerical studies.

The focus of this study is an altogether simpler system than those listed above, namely a *regular two-dimensional (2D) cellular structure*. Some examples of these systems have been sketched in Figure 1.1. Arguably the most familiar is the hexagonal-celled honeycomb (Figure 1.1 (a)) which has attracted the attention of scientists within research fields ranging from biology to engineering [3, 5, 7–13] . Strikingly regular in form, the bee's habitat is a strong, lightweight structure [3], and the tesselation of cells is an efficient packing arrangement in the 2D plane [14]. There is a significant amount of research into this class of materials [3], with lattices of hexagonal, triangular (Figure 1.1 (b)) or square cells forming the basis of many numerical and experimental studies [15–19]. More complex structures such as the Kagomé lattice, which comprises a mixture of hexagonal and triangular cells arranged in the regular, repeating pattern shown in Figure 1.1 (c), have also been comprehensively studied [20, 21].

1.2 Deformation Mechanisms

A particular feature of the mechanics of two-dimensional cellular structures which has been extensively researched is their behaviour under deviatoric (uniaxial) and hydrostatic (biaxial) loading conditions [3, 5, 13, 22]. The response of these systems to compression can be divided into two sub-classes [3, 23]. In *bending-dominated* cellular structures, compression causes the relative rotation of the struts about the node at which they meet. *Stretching-dominated* structures differ in that the macroscopic deformation manifests itself as the axial compression of the struts. These contrasting mechanisms have consequences for the elastic properties of the lattice, where stretching-dominated structures are generally observed to be the stronger and stiffer of the two [3].

According to the Maxwell criterion for rigidity in two-dimensional structures [24] the connectivity Z - the number of struts meeting at each node - is definitive in distinguishing between bending- and stretching-dominated structures. A simple demonstration of the role played by connectivity in this context has been given by Deshpande et al [1] where the action of load F on the top and bottom vertices of a diamond-shaped frame is considered. The addition of a transverse strut to the frame as shown in Figure 1.2 prevents its collapse by rotation about the joints, and instead the structure must deform via axial compression.

In two-dimensional structures, $Z = 4$ is a significant connectivity value and provides a necessary condition for rigidity in frames, however it is not a

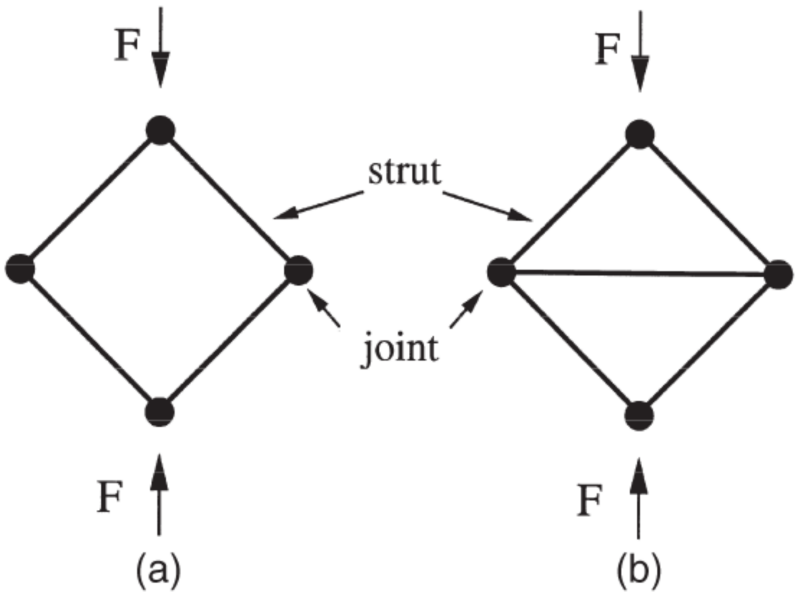

Figure 1.2: The end loaded frame. The struts will undergo relative rotation when a load F is applied to the frame (a). Addition of the transverse strut (b) prevents this from occurring and as such the frame is stronger and stiffer. This image has been reproduced from [1].

sufficient condition as states of self-stress, for example, must be accounted for [1]. Generally, in cellular solids with $Z < 4$ (e.g. hexagonal-celled lattices), bending of the cell walls tends to dominate, and where $Z \geq 4$ (triangular-celled lattices) the structure will preominantly deform via axial stretching and thus be more rigid in comparison to the former. The elastic properties of the Kagomé lattice ($Z = 4$) are highly sensitive to imperfections such as missing struts [21] which reduce the average connectivity and therefore cause the system to switch from a stretching- to a bending-dominated structure.

1.3 Pattern-Switching in Cellular Structures

As discussed in Section 1.2, the shape of the cells in a 2D cellular structure plays a a key role in determining its response to compression. Indeed, shape is one of three variables which do so; the remaining two are the size of the cell relative to its spacing from its nearest neighbours (Gibson and Ashby highlight this as *the* defining variable [3]) and the material used to construct the solid walls. It is cell shape which is the focus of the research presented here. Specifically, we consider the effect of *uniaxial* compression on cellular structures which possess *circular, diamond* or *square* cells arranged on a *square* lattice.

The cellular geometries described above have received increasing attention in the last decade. In 2006[1], Mullin et al [2] showed that uniaxial compression

[1]In the same year, Triantifyllidis et al showed in simulations that this pattern switch can be caused by triggering a microscopic instability in the porous structure when it is loaded biaxially [22].

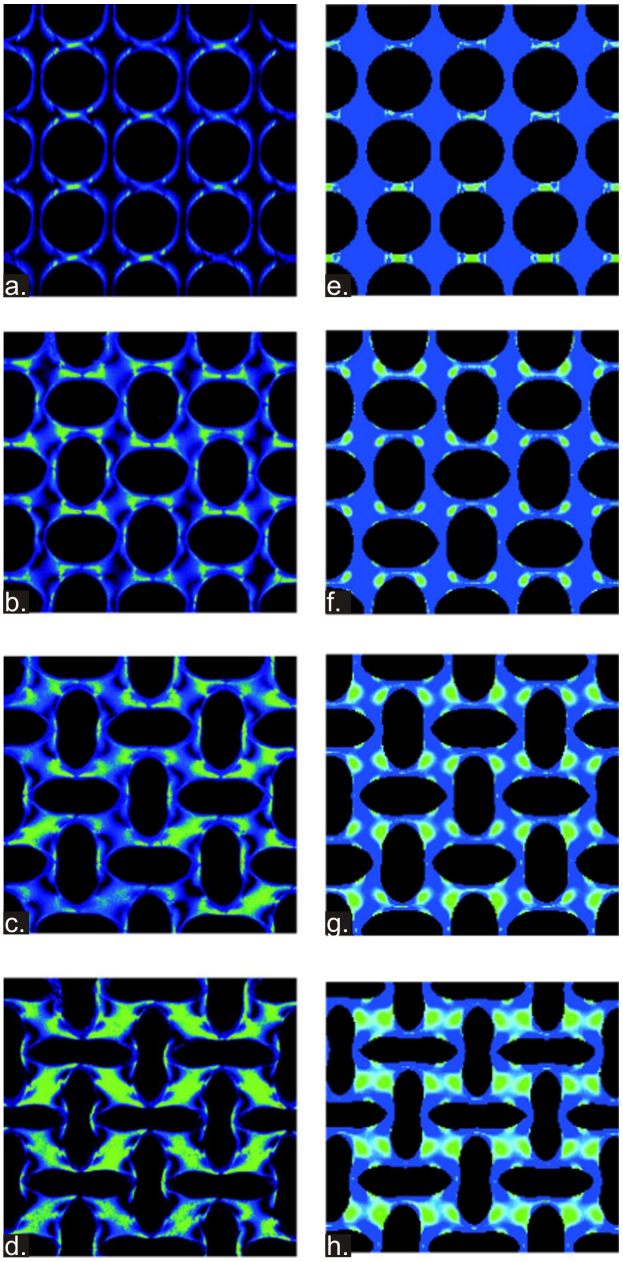

Figure 1.3: Pattern-switching in the square lattice of circular voids. In the experimental (a - d) and numerical (e - h) images the cellular structure is shown to undergo a novel pattern transformation. The sample is compressed along its vertical axis and increased deformation results first in the onset of the pattern and then its accentuation at higher strain. These images are reproduced from [2].

of a square lattice of circular voids brings about a pattern-switching effect which is both reversible and repeatable. Interestingly, the initial experiments were conducted as a by-product of an unconnected piece of work. The authors manufactured cylindrical discs of a photoelastic polymer in order to assess the pressure distribution under piles of grains [25]. As a result of this, they were left with an intact porous frame which, when compressed, showed novel and eye-catching behaviour.

The pattern switch in the cellular structure is illustrated in Figure 1.3. The images were taken from experiments (left-hand column) and finite element simulations (right-hand column) and are of the central section of the sample at increasing amounts of macroscopic deformation. The voids were initially circular (Figure 1.3 (a) and (e) respectively) and formed a diamond plate pattern of mutually orthogonal ellipses which became further accentuated with increased compression. The qualitative experimental features were also captured in two simulations using the nonlinear finite element software ABAQUS [26]. The first was of the finite sample, for which boundary effects were included. The second was of a representative volume element (RVE) using periodic boundaries and plane strain condition. The pattern onset was found at a higher degree of compression in the former simulation type [2].

The switch in the structural geometry was a result of an elastic instability [26] triggered by the action of load on the top surface of the structure. The instability onset occured above a critical load value and the switch in the geometry was rapid and global. Mullin et al showed that the same pattern-

switching effect occurs when the shape of the voids is changed to an ellipse, although the onset was associated with a different degree of compression depending on the aspect ratio of the voids and the direction of compression [2].

The quantitative data recorded by Mullin et al is presented in Figure 1.4. There are two distinct compression regimes in the plot and these can be linked to the shape of the cells during the experiment. The first is a linear stress-strain phase, during which the cellular pattern was homogeneous throughout the sample (A in Figure 1.4). The onset of the elliptical pattern (B in Figure 1.4) was in turn associated with a plateau regime of near constant stress. This two-phase behaviour is commonly found in studies of cellular structures under compression [3, 5]. During the initial phase of compression, cellular structures undergo uniform deformation which manifests itself as Hookean stress-strain behaviour [3, 27] and this is true regardless of the dominant observed deformation mechanism. The levelling-off of the data results from the collapse or *failure* of the structure, either in the form of plastic effects (i.e. permanent stretching of the ligaments or rotation at the nodes), brittle failure (breaking of the ligaments) or, as was the case here, *elastic buckling* (reversible deformation).

1.4 Elastic Buckling

According to Von Mises [28] a circular void in an elastic sheet will form either a vertical or horizontal ellipse upon its collapse under hydrostatic loading. The square lattice of circular voids is a coupled system which forms a periodic mixture of these two states upon buckling. The instability which gives rise

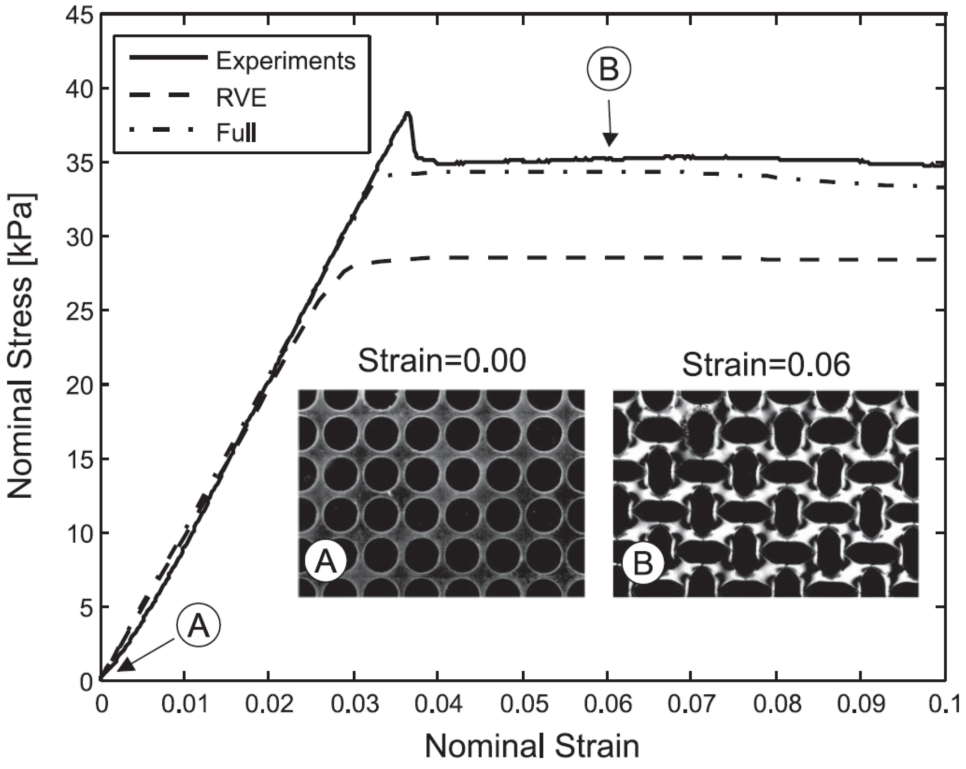

Figure 1.4: The stress-strain curves taken by Mullin et al. In both the experiments (bold line) and the simulations (dashed), the data can be broken up into two phases which were associated with the cellular pattern. The qualitative features are characteristic of those found in compression experiments performed on cellular structures [3] and the inset images of are the experimental sample before (A) and after (B) the pattern switch. This figure is reproduced from [2].

to this is similar to that found in the classical problem of the end-loaded Euler-Bernoulli column [3, 29]. In this, an initially upright column (length L) becomes unstable at a critical value of the applied load called the Euler buckling load F_{CR} [30] which is given by

$$F_{CR} = \frac{\pi^2 EI}{(kL)^2} \tag{1.1}$$

In equation (1.1) E is the Young's modulus of the column (Pa) and I is its second moment of inertia about its central axis (kgm^2). The constant k specifies the boundary conditions (e.g. if the column is pinned at one/both end(s)), and is used to define the *effective length* of the column, kL. The onset of instability causes the column to assume a new stable state - a half-wave - which is its first buckling mode as illustrated in Figure 1.5 (a). Theoretically, there are an infinite number of solutions to the Euler-Bernoulli problem [30]. The first mode has the largest spatial wavelength and the lowest associated critical load; it is therefore the first to be triggered when the applied load F is incremented from zero. As such, the new buckled state of the column is observed when $F > F_{cr}$.

The Euler-Bernoulli column is a common example of a system which undergoes a symmetry-breaking pitchfork bifurcation from its initial stable configuration. The perfect pitchfork bifurcation diagram is shown in Figure 1.6 (a) where the variable x represents the state of a nonlinear system and r is a control parameter. The stable states of the system are marked by the bold lines in Figure 1.6 and the unstable ones by dashed lines.

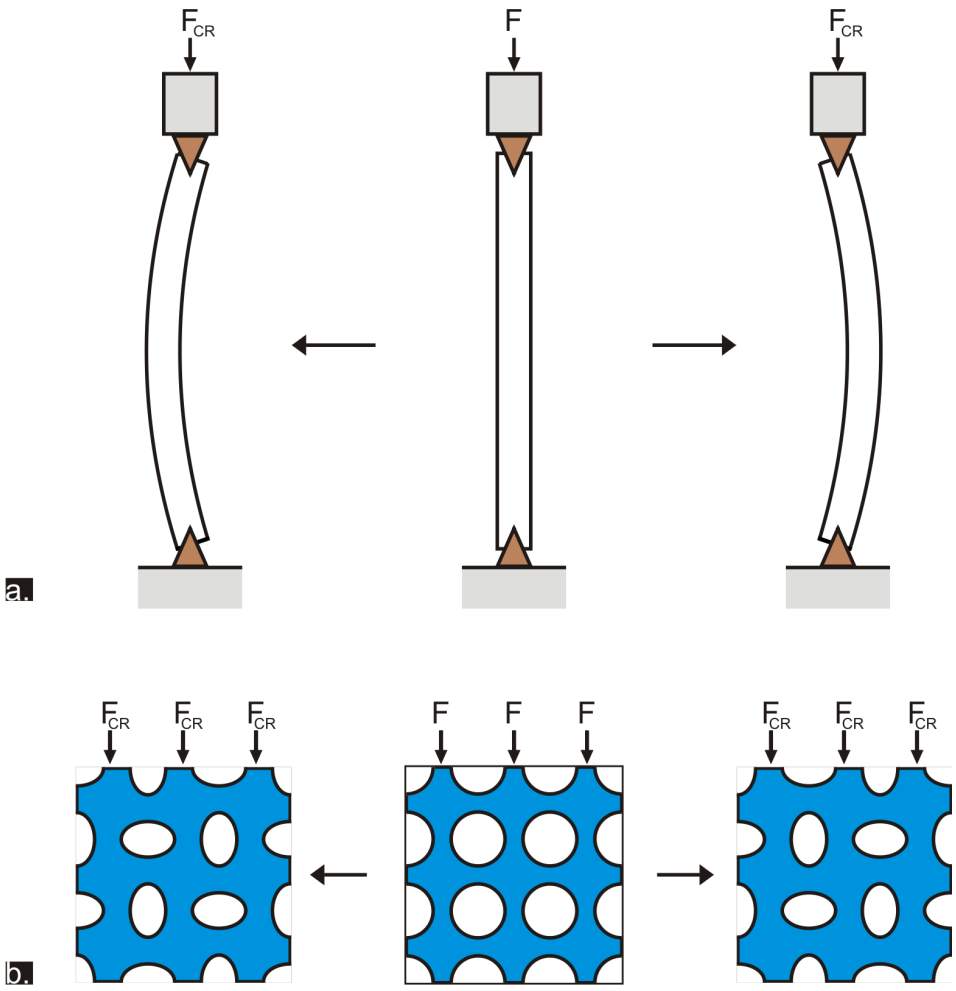

Figure 1.5: The buckling states of nonlinear systems. The end-loaded Euler-Bernoulli column (a) will buckle either to the left or to the right above a critical load. Triggering the elastic instability in the square lattice (b) causes the circular voids to transform into either horizontally- or vertically-aligned ellipses.

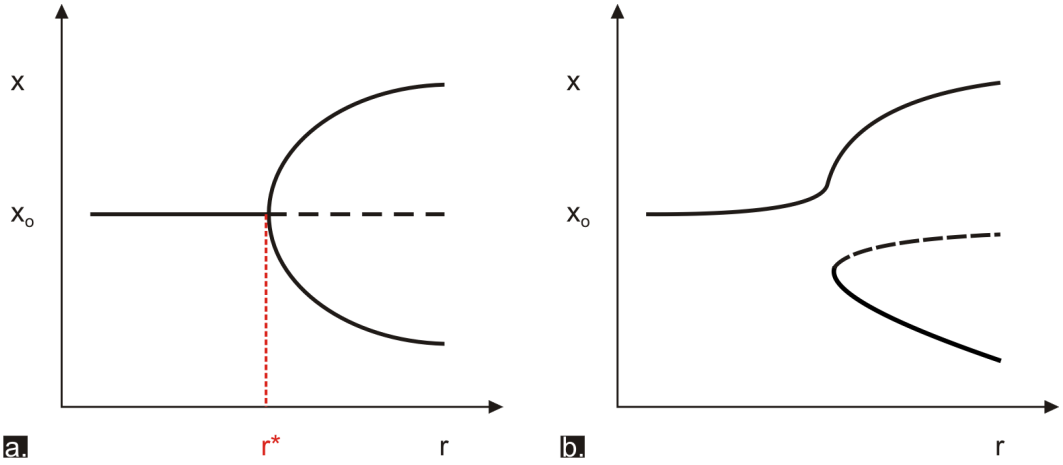

Figure 1.6: Perfect (a) vs imperfect (b) pitchfork bifurcation diagrams. The bold black lines in each panel represent the stable states of the system and the dashed black lines the unstable states. The effect of the perturbation is to disconnect the branches in (a) such that they form one continuous branch and a saddle-node. This figure has been reproduced from [4].

The trival stable state ($x = x_o$) of the system exchanges stability with two nontrivial equilibrium states when the control parameter r attains the critical value r^*. The nontrivial branches of the system are the possible stable states of the system with $r > r^*$ and these are symmetric. The effect of a perturbation on the perfect pitchfork bifurcation diagram is shown in Figure 1.6 (b). The perturbation causes the stable branches of the system to become disconnected and there exists one primary state which forms along a continuous branch as r is increased. The other state is terminated by a saddle node which connects one unstable and one stable branch [4, 29, 31]. The sharp transition from the x_o state to the nontrivial branch in the perfect system is smoothed out by this effect, and the larger the magnitude of the

perturbation, the greater the extent of the disconnection.

In the Euler-Bernoulli problem, the state variable x is the deflection of the column from its central axis and the control parameter r is the applied load F. The column is upright (i.e. undeflected) in the trivial state, whereas in the untrivial states the structure buckles either to the left or to the right as shown in Figure 1.5 (a). For a perfect column, there is an equal probability that it will buckle to either the left or the right. In the real world, however, the column will buckle to one side, meaning that it has a preferred buckling state. This effect is brought about by imperfections in the column which have the same effect as a perturbation in the pitchfork bifurcation problem. The cumulative effect of imperfections is to create a pair of states, one continuous and one disconnected.

1.4.1 Elastic Buckling in Square Arrays

It is possible to compare the behaviour of the square lattice of circular voids under compression with that of the Euler-Bernoulli column. The similarities between the systems are clear; both structures become unstable above a critical load and this causes a marked change in their respective geometries. In the cellular structure, the pattern of mutually orthogonal ellipses represents its first buckling mode. Other modes exist and these are triggered at higher values of the applied load [26], resulting in the onset of patterns other than the repeating arrangement of orthogonal ellipses.

In the first elastic buckling mode,the cellular structure must assume one

of the states illustrated in Figure 1.5 (b). This has been shown by modelling the voids in the cellular structure as dislocation dipoles which interact through linear elastic forcing [32]. The onset of instability neccessitates that in the new cellular pattern the voids must be oriented by a rotation of 90^o relative to their immediate neighbours. This therefore allows for two possible states, in which an initially circular void will become either a vertical or horizontal ellipse when the pattern is formed. In experiments there are numerous sources of imperfection in the manufacturing (e.g. hole size distribution) and testing (uneven application of applied load) processes. The cumulative effect of these is to bias the system to one orientation of the pattern in the buckled state, just as the Euler-Bernoulli column will buckle to one particular side.

1.4.2 Global and Local Modes

Whilst the pattern-switched state was experimentally observed by Mullin et al, other buckling modes exist and these have been explored using numerical simulations. Triantifyllidis et al [22] and later Boyce and Bertoldi [26] have demonstrated the existence of both global and local buckling modes of the porous structure. In the former, the onset of instability leads to a new equilibrium state characterised by a large wavelength compared to the unit cell of the trivial equilibrium state. In one such global state the whole structure forms a half-wave pinned at its top and bottom edges and no elliptical pattern formation. Where such an instability occurs, this results from *macroscopic* failure of the structure, whereas the pattern formation described in Section 1.3 results from its *microscopic* failure under compression [22]. Both events are caused by the attainment of a critical loading and there is a competition

between these; whichever critical load value is attained first in the monotonic compression process will lead to the associated state.

By using distinct techniques it has been possible in numerical studies to distinguish between the two aforementioned buckling types. The macroscopic buckling point can be calculated in FEM studies by detecting the point at which the homogenised tangent moduli of the structure lose ellipticity [22, 26]. This approach involves performing a classical eigenvalue analysis of the finite elastic structure and therefore incorporates boundary effects. More recently, a Bloch wave analysis method has been developed which can be used to predict the microscopic failure point, and this involves considering the evolution of the *unit cell* as opposed to the whole structure. The Bloch method uses the assumption that, in its compressed state any spatial function Ψ of the structure evalulated at point X will be symmetric under translation i.e.

$$\Psi(X) = \Psi(X + p_i \mathbf{a_i}); i = 1, 2 \tag{1.2}$$

where in equation (1.2) p_i are indices which describe the translational periodicity of the structure as it undergoes deformation and $\mathbf{a_i}$ are the basis vectors of the structure. According to the Bloch condition [33], the spatial function is associated to a wavelength k_0 (and hence an energy) which is calculated by assuming that

$$e^{[i\mathbf{k_0}.\mathbf{p_i}\mathbf{a_i}]} = 1 \tag{1.3}$$

The periodicity of the structure is calculated by solving an eigenvalue problem in $\mathbf{k_0}$. Bertoldi and Boyce have shown [26] that, the $k_0 = 0$ state is associated with unitary periodicity in both planar directions i.e. $p_1 = p_2 = 1$. This is the case found to be prior to the bifurcation, meaning that the periodicity of the lattice remains constant as the compression continues. At the bifurcation point, post bifurcation, a new state emerges with $p_1 = p_2 = 2$, and this is the lowest energy stable solution for the structure. This new periodicity characterises the state observed by Mullin et al [2].

It has been possible to compare the predictions of micro- and macroscopic approaches described above. For finite arrays of two-dimensional square arrays of circular voids, Triantyfillidis et al [22] have shown that microscopic instabilities dominate the structure. The shorter wavelength instability comes in at a lower critical load than te long wavelength solution, and the critical points associated with the respective buckling types diverge as the compressibility of the material increases. By considering the effect of biaxial loading, 2D macroscopic and microscopic failure surfaces have been constructed, with the latter lying within the former, i.e. the micro-buckled state occurs first.

For infinite arrays of square voids, Bertoldi and Boyce [26] have demonstrated the strength of the Bloch method for predicting the equilibrium state post-bifurcation. In their study, two different approaches to modelling infinite structures were used. In the first (a refined Eigen Analysis, in which macroscopic instabilities were monitored), several $n \times n$ RVE square arrays

were simulated and periodic boundary conditions applied to these. It was found that for even n values, the first bifurcation led to the familiar elliptical pattern observed by Mullin; for odd-n values, new modes with inconsistent wavelength values were activated. In addition to this, the critical load value fluctuated as the size of the RVE was changed, meaning that the form taken by the structure as a result of the instability onset was dependent on how the the smallest repeating unit of the structure was defined when formulating the problem. Whilst this was an issue when considering the homogenised approach, it was not a factor in the Bloch analysis as only the evolution of the unit cell of the trivial state needs to be considered. It remains to be seen how size effects effect experimental pattern formation, however it should be assumed that simply increasing a structure size should not affect the dominant buckling mode, and in that case the Bloch wave analysis appears to be best suited to the study of this system.

1.4.3 Buckling in Other Cellular Structures

In hexagonal cell honeycombs, the collapse of the lattice has been observed to occur locally within one band of cells and then spread throughout the remainder of the structure [5, 13, 34]. An example of localised buckling in a honeycomb is shown in Figure 1.7 where the data taken by Papka et al has been plotted [5]. It is highlighted here that the effects observed by Papka were induced plastically in an aluminium honeycomb structure and the original lattice geometry was not recovered upon relaxation. Howver, these experiments provide an excellent example of the phenomena of localisation, which

is not exclusively a symptom of plastic deformation.

Whilst the main features of the quantitative data are similar to those measured by Mullin et al [2, 26], the buckling initialises in one of the middle rows of cells and is not a global feature. The localised effect results from imperfections in the construction of experimental samples which cause local weakened resistance to buckling, and hence localised deformation patterns. The same effect has been found by Chung and Waas [35] in hexagonal packed arrays of cylinders. The cells become sheared from side-to-side in a herring bone pattern [26, 36] which propagates from row to row as the structure is compressed [35, 37]. By incorporating the imperfections distributed in the experimental system into simulations (each "circle" had an aspect ratio of approximately 1.10 as opposed to 1.00 in the perfect system), localised onset of the pattern was observed and good qualitative agreement with the experiments was found.

In experiments conducted in parallel to those on the square array of circular cells, Bertoldi et al [26] showed that the herring bone pattern can be induced globally. Localisation of the pattern occurred in the experiments after the buckling event, which may have been because the strains associated with the pattern onset were high (approximately 12 % compared to 4 % for the square lattices [26]). The instability in both systems was the same, although in the oblique lattice this initiated shearing of the cells. As with the square lattice, the new cellular pattern in the oblique system could take one of two possible forms, with a row of cells sheared either to the left or to the

right.

As discussed above, imperfections are always present in experimental systems. It has been found that in commercially-made honeycombs, imperfections (missing/wavy cell walls, blocked cells, for example) of the order 5% are required in order to accurately simulate these materials using numerical models [12]. These imperfections tend to cause localisation of the patterns which form. Therefore, the novelty of the pattern switch described by Mullin et al lies in the global nature of the switch observed in the structure [2,26,32]. All of the ligaments in the structure buckle in the same *sense*, with the result that, under uniaxial loading conditions, no localised pattern formation is observed. There must be imperfections in the system in order to determine the preferred buckling state of the structure. However, the highly connected geometry appears to reduce the likelihood of localisation in this system.

1.4.4 Pattern-Switching as a Useful Tool

Whilst the initial studies of the square lattice of circular cells were conducted at the millimeter length scale, the pattern-switching phenomenon discovered by Mullin et al has been shown to persist over a range of length scales [2, 38, 39]. This has, for example, been achieved by swelling circular pores on a polydimethylsiloxane (PDMS) substrate upon exposure to tuolene [38]. This, along with the robust nature of the switch as highlighted above, has encouraged studies which have assessed the application of the pattern switch in practical devices such as phononic [40] and photonic [41] crystals. In both of these system types, the pass band structure is governed

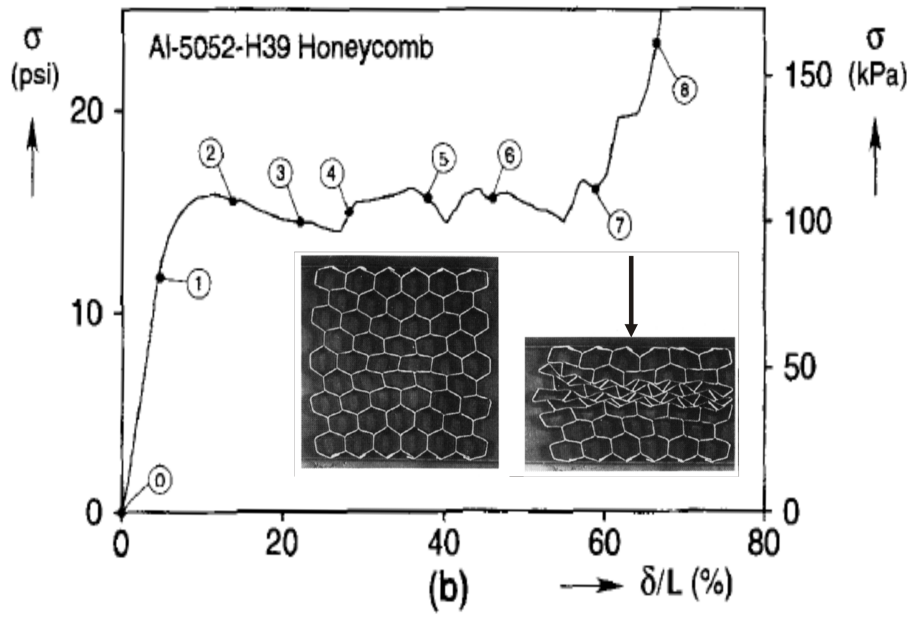

Figure 1.7: The stress-strain data taken by Papka et al on a hexagonal-cell honeycomb. The same qualitative trends are shown as found in Figure 1.4, however the buckling of the structure was characterised by local effects. The inset images show the spreading of buckling through the rows of the honeycomb sample, which causes the small bumps in the stress-strain data in the plateau phase of compression. This figure has been reproduced from [5].

by their structural geometry. Bertoldi and Boyce [40] have shown that the switch in cellular geometry can open new band gaps in porous acoustic devices, whereas enhanced transmission has been reported in optical devices comprising columns of orthogonal elliptical voids [42].

There is great potential for exploiting the instability-driven pattern switch because it is straightforward to control; it can be locked in by using elasto-plastic coatings [43], or locally imprinted by partial exposure of microframes

to acrylic acid [36]. The switching mechanism has also been used as a patterning tool, depositing nanoparticles onto photoresist substrates using the swelling techniques described above, as shown by Zhang et al [44]. The application in these systems is, therefore, two-fold: it can be used to imprint patterns on the surfaces of structures possessing dimensions on a wide range of length scales [39], or to create tunable devices which respond to an external stimulus by changing their geometry in a global, predictable manner.

One avenue of research which has sparked particular interest is the effect of the pattern switch on the width of the structure cellular structure. Whereas typically solids *expand* transversally a a result of axial compression, there is a class of materials which counter-intuitively *contract* under the same loading conditions. These materials are called *auxetics* and are notable as they possess a *negative Poisson's ratio*, which leads to high fracture strengths and indentation resistances [45]. Since the discovery of the auxetic effect by Lakes [46], negative Poisson's ratios have been shown to be associated with complex structural geometries or multi-staged manufacturing techniques.

Bertoldi et al [6] have shown in both experiments and simulations that the onset of the pattern in the square lattice of circular cells is linked to an auxetic effect in the structure as shown in Figure 1.8. During the linear compression regime the structure behaves as a conventional solid with Poisson's ratio $\approx$ 0.2 [47][2] but this rapidly decreases to a negative value when buckling occurs. In practice, the cellular structure can be viewed as an interpretation of the

[2]For the purpose of comparison, steel has a Poisson's ratio of 0.3 [46]. In cork $\nu = 0.0$, which makes it able to withstand high pressures in bottles

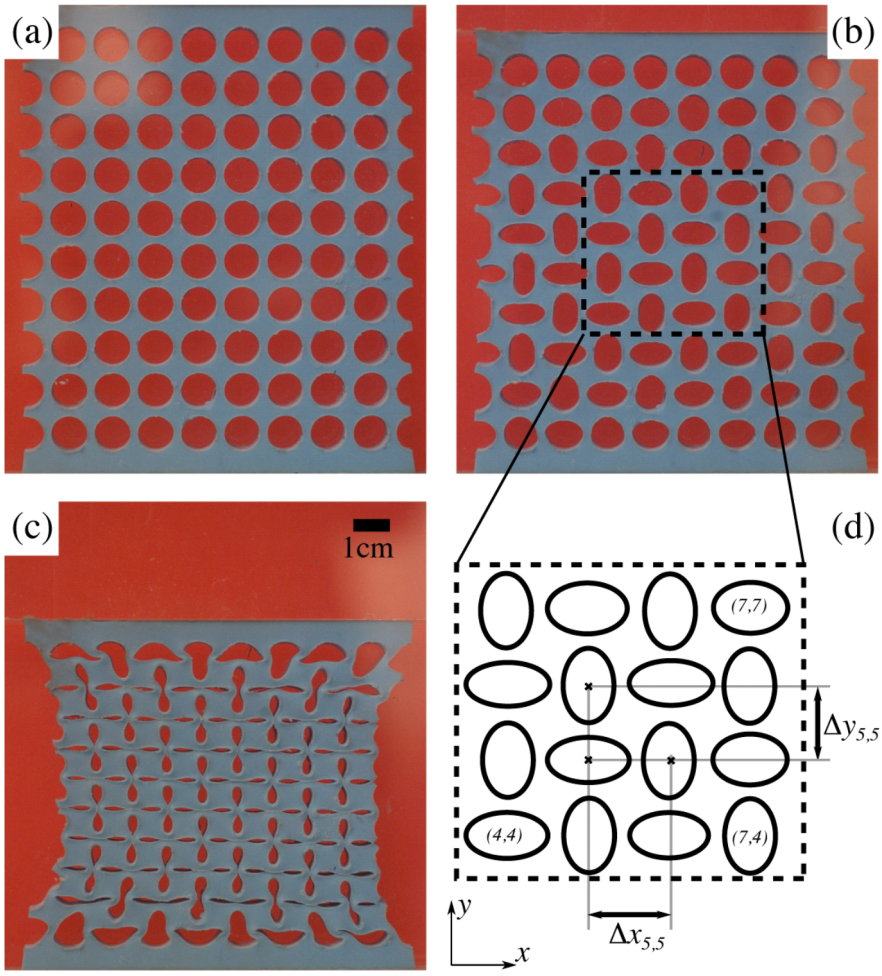

Figure 1.8: The auxetic effect. In (a - c) the experimental sample is shown at increased degrees of compression. The onset of a negative Poisson's ratio is directly linked to the pattern transformation and this was calculated by measuring the inter-void distances as shown in (d). This figure is reproduced from [6].

hinged models used to explain this counterintuitive effect, which rely on the interplay between rotating rectangular units [48, 49]. The effect comes about from the coupling of the inter-ligament connectors and no advanced manufacturing techniques are required to achieve this. The images in Figure 1.8 illustrate the simplicity of the structure required to create the auxetic effect.

1.5 Structure of the Thesis

Whilst the square lattice of circular voids is an apparently simple system, it shows striking behaviour which has application in various fields. In this thesis, the fundamental properties of the pattern switch are explored using primarily experimental techniques. The work is presented with the following structure:

The apparatus used in compression experiments is described in **Chapter 2** alongside examples of the measurements made using it. Particular emphasis is placed on the procedures followed in obtaining estimates of the elastic properties of the bulk material used in the manufacture of the experimental samples.

In **Chapter 3**, the results of experiments performed on a square lattice of circular cells are documented. An image analysis method is described which allowed the aspect ratio of voids in the experimental sample to be monitored, thus providing a microscopic measure of the effect of compression on the structure. Analysis of the variation of this parameter with strain

allowed the identification of a critical point at which the cellular pattern changed. This, combined with the stress-strain data, enabled information to be gathered as to the *stability, strength* and *stiffness* of the structure. A stable secondary state is also shown to exist and this became unstable on unloading. In **Chapter 4**, the analysis of **Chapter 3** is expanded to further experimental samples and in particular the effect of the size of the voids relative to their spacing on the critical point was analysed. The experimental data is compared with predictions of a discrete model and we establish empirical stability, stiffness and strength relationships which suggest that the square array of circular cells is a stretching-dominated structure. This part of the study is concluded by considering the role played by void shape on porous 2D structures under compression.

The focus of **Chapter 5** is on the buckling of three-dimensional cellular structures whose geometry comprised the superposition of two square lattices of circular cells onto one another. The results of this study implied that the two-dimensional instability dominated the structure and resulted in the formation of a planar pattern regardless of the relative sizes of the two sets of voids within the lattice. The instability of a secondary state in these structures was investigated and it is demonstrated that the effect of imperfections in this system is similar to in the 2D case although the extent is greater.

The final results chapter is **Chapter 6**, where we present the research conducted on a 2D granular crystal. This system, which was made up of discrete grains of contrasting size and elastic properties arranged on a regu-

lar lattice, exhibited similar pattern-switching phenomena as in the cellular structures described in the previous chapters and so provides an interesting foil to fully connected cellular systems.

The research is summarised in **Chapter 7** and a description of potential routes of further work is given. Three **Appendices** are included in order to add completeness to this piece of work. In **Appendix A**, the paper "Negative Poissons Ratio Resulting from an Elastic Instability" has been included. This is one of three publications which have stemmed from the research presented here. In **Appendix B** the manufacturing techniques used in making the experimental samples are given. Lastly, in **Appendix C** the mathematical formulation of the discrete model described in Chapter 4 is fully detailed.

Chapter 2

Experimental Method

A description of the apparatus used to collect experimental data is presented. Experimental samples were uniaxially compressed using one of two loaders attached to a compression machine. The load-displacement data recorded by the machine was converted into stress and strain measures and the effects of the compliance of the machine and offset load calculations were included. The materials used to make the cellular structures were addition-curing elastomers. In tests on calibration samples these were shown to exhibit negligible rate dependence under uniaxial loading conditions but significant hysteresis when unloaded. This effect was reduced by applying a lubricating layer of Vaseline to the top and bottom surfaces of the samples. The stress-strain behaviour of the material was shown to be well approximated by the Mooney-Rivlin elasticity model and its Young's modulus E_s was determined by fitting this model to experimental data.

2.1 Experimental Samples

The goal of the experiments was to assess the behaviour of various elastic structures under uniaxial loading conditions. The structural geometries and typical dimensions of the experimental samples are summarised in Table 2.1 and more in-depth descriptions of these structures can be found in the results chapters which follow. The samples were made using moulds on the millimetre scale. A description of the manufacturing process for each structure type is presented in Appendix B. The calibration samples described in the bottom line of Table 2.1 were used to determine the elastic properties of the bulk material used to make the cellular structures. Further details of this aspect of the experimental work are given in Section 2.4.

2.2 Compression Setup

2.2.1 Compression Machine and Load Cell

An Instron 5569[1] machine was used to perform controlled compression tests on the experimental samples. A 2525-806 Series Drop-through load cell capable of measuring applied loads up to 1kN was slotted into a platform on the compression machine and fastened into place using three screws. An external loader was attached to the chassis of the load cell. The platform was raised and lowered by means of a motor-driven pulley system within the compression machine and its location could be adjusted by using the control panel on the machine. *Loading tests* were performed by lowering the platform at a constant speed from its initial position; *unloading tests* consisted of the same process in the reverse direction. It was possible to conduct *cyclic* tests which comprised both of these processes.

[1]Instron, High Wycombe, UK

Name	Description (*Typical Dimensions)*
csa-lattice	n × m square array of circular cells cut from 2D sheet of elastomer (*50 mm × 50 mm × 8 mm)*
dsa-lattice	n × m square array of diamond cells cut from 2D sheet of elastomer (*50 mm × 50 mm × 12 mm)*
ssa-lattice	n × m square array of square cells cut from 2D sheet of elastomer (*50 mm × 50 mm × 12 mm)*
cubic lattice	Two sets of cylindrical voids arranged on a square lattice aligned to cross one another within a 3D cube of elastomer (*70 mm × 70 mm × 70 mm)*
granular crystal	Ordered arrangement of soft and rigid cylindrical particles (*100 mm × 100 mm × 10 mm)*
calibration sample	Cylindrical block of elastomer (*10 mm × 10 mm × 10 mm)*

Table 2.1: Description of the experimental samples. The aim of the study was to determine the compression behaviour of the structures described here.

The load cell measured the load applied by the compression machine in order to compress the sample at a constant displacement speed. This was calculated according to the change in output voltage across a Wheatstone Bridge electrical circuit bonded to strain gauges within the cell. The load values were measured once every 100 ms during experiments and logged, along with the instantaneous displacement of the platform from its starting position, using the Bluehill software on a PC connected to the machine.

2.2.2 Perspex Loader and Housing

During the initial tests the loader consisted of a Perspex sheet (width 100.10 $\pm$ 0.05 mm, thickness 9.68 $\pm$ 0.09 mm) attached to an aluminium clamp. When using the Perspex loader the samples were placed in a housing rig to ensure that they stood upright throughout the tests. The housing comprised an aluminium U-shaped frame and base which attached to the compression machine using four screws. Two Perspex plates were screwed to the frame. These were the front and back plates of the housing and the spacing between them was 10.1 $\pm$ 0.1 mm. There was a clearance of 0.7 $\pm$ 0.1 mm between the loader and housing when the setup was assembled and the front plate was removable to allow access to the experimental sample where necessary. The experimental samples were dusted with flour prior to the test so as to reduce frictional effects.

A schematic of the experimental setup incorporating the loader (transparent), platform (dark grey), load cell (black) and the frame (light grey) is shown in Figure 2.1. The Perspex loader and housing were used for all experiments on csa-lattices and for the experiments conducted on granular crystals described in Chapter 6. Where the Perspex loader is referred to it is implied that the experimental samples

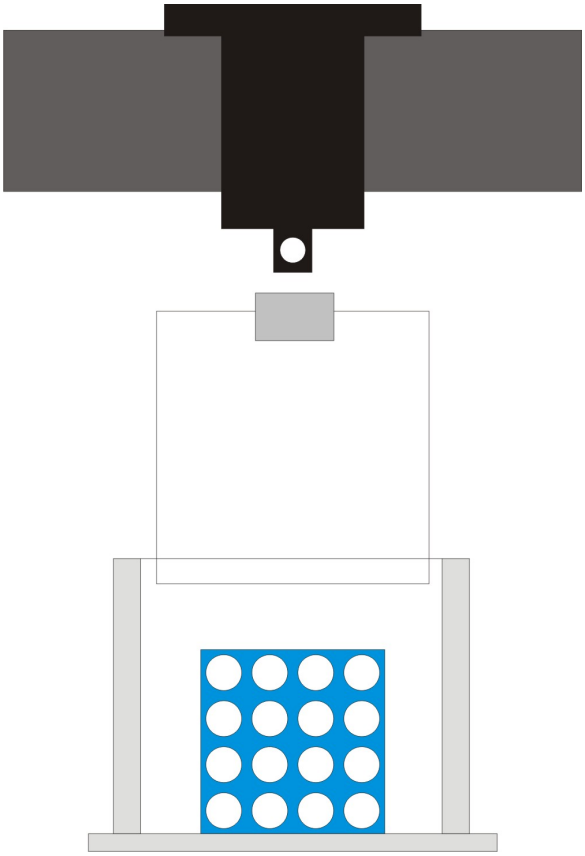

Figure 2.1: Schematic of the experimental setup used to test a csa-lattice (not to scale). The sample (blue) sat in the housing during testing and the Perspex loader (transparent) was used to transmit load across its top surface. This was attached by means of a clamp to the chassis of the load cell (black). The load cell was fastened to the movable platform (dark grey) on the 5569 machine (not shown).

stood in the Perspex housing during that test.

2.2.3 Aluminium Loader and Base

An alternative loader was manufactured to accommodate free-standing experimental samples which possessed a greater surface area than the csa-lattices. This was a circular aluminium loader (radius 91.53 ± 0.05 mm) which was used when conducting experiments on the dsa-, ssa-lattices, cubic lattices and calibration samples. During these tests the samples stood on a flat aluminium base. Both of these components attached to the compression machine in the same manner as those described in Section 2.2.2. Where the aluminium loader is referred to it is implied that the experimental samples stood on the aluminium plate throught the test. An image of the aluminium loader and base taken during a test on a calibration sample is shown in Figure 2.2.

2.2.4 Camera

Images were taken of the experimental samples during tests using a Nikon D100 digital camera (resolution 6.1MP). The camera was synchronised to the compression machine such that images were taken at regular successive displacement intervals, typically 0.1 mm. A red laminate screen was placed behind the experimental sample when images were taken. The contrast between the sample and its surroundings as well as the high resolution of the images taken allowed image analysis using edge detection algorithms from the MATLAB: Image Processing Toolbox. This aspect of the work is described in Chapter 3.

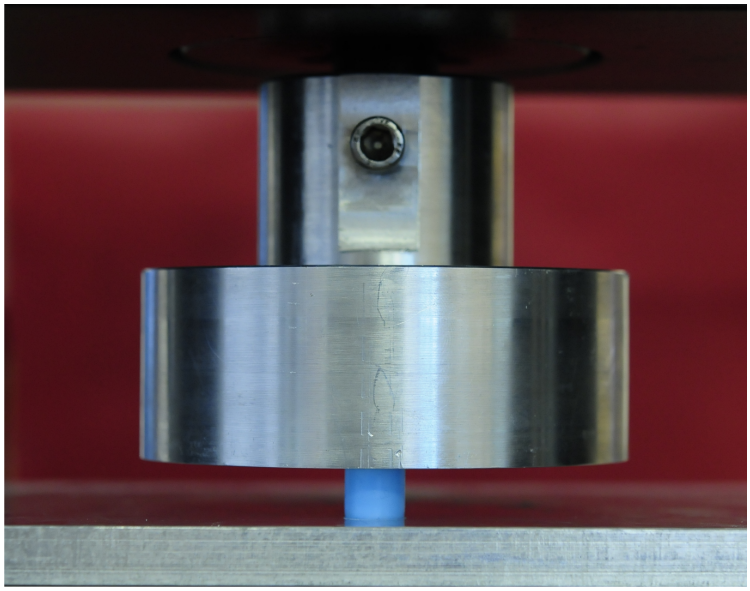

Figure 2.2: The aluminium loader. This component of the experimental apparatus had a circular cross section and was used in the calibration experiments as shown here.

2.3 Data Acquisition and Analysis

The load-displacement data recorded during compression experiments was converted into stress and strain measures respectively. The steps and precautions taken during this process are described in the following sections.

2.3.1 Alignment and Positioning

The compression setup was assembled for each test such that the loader was level and covered the surface area of the experimental sample, which ensured that during tests the load was distributed evenly across the surface of the sample. When using the Perspex loader, care was taken such that no contact was made between the loader and the housing as friction between these two surfaces would affect the experimental readings. Before commencing the test the equilibrium position of the

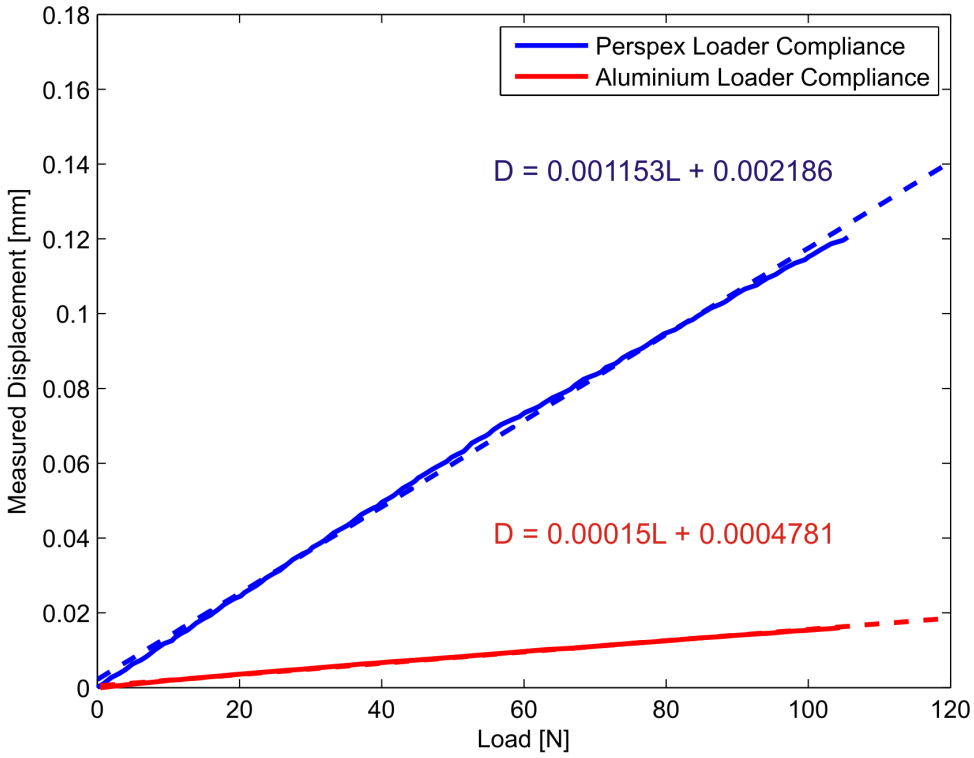

Figure 2.3: The compliance curves for the Perspex (blue) and aluminium (red) loaders. These were measured by compressing the rigid bottom surface of the experimental setup. The bold curves are the experimental data and the dashed ones are the fits of equation (2.1) to this.

platform was set such that the bottom of the loader was situated approximately 1 mm above the top of the sample. This region of space is referred to here as the *offset region*. Beginning the compression test at a point where the loader was visibly above the surface of the sample ensured that the sample was not pre-strained prior to recording the data and allowed checking for frictional effects.

2.3.2 Compliance Correction

The reaction force exerted by the experimental sample on the loader during the test necessitated a correction to the displacement readings recorded by the load cell. This was calculated by considering the *compliance* of the experimental setup, which was obtained by running a compression test without any experimental sample in place. The loader was lowered such that it came into contact with the bottom surface of the apparatus. A compression test was initiated and the displacement-load data taken during this constituted the *compliance curve* of the experimental setup. By compressing the rigid bottom surface of the apparatus it was ensured that the loader was not displaced during the test. Non-zero displacement values observed in the test arose from bending of the strain elements within the load cell as well as compression of the loader itself.

It was necessary to perform compliance tests for both of the loaders used in the experiments. Compliance curves taken using the Perspex (blue) and aluminium (red) loaders respectively are plotted in Figure 2.3. In both cases a linear increase in measured displacement D with applied load L was observed. The loading range was restricted to 100 N as this was the maximum load value reached during the experiments on the elastic structures. The dashed lines are least-square fits to each data set of the form

$$D = cL + d_0 \tag{2.1}$$

where c is the compliance of the setup (mmN^{-1}) and d_0 (mm) is the offset contact term. As shown in Figure 2.3 the Perspex loader ($c = 1.153 \times 10^{-3}$ mmN^{-1}) was approximately an order of magnitude more compliant than the aluminium loader for which $c = 0.15 \times 10^{-3}$ mmN^{-1}. This is because the former is made from a

material with Young's modulus $E \approx 0.3$ GPa which is less stiff than the latter ($E \approx 50$ GPa). For both loaders it was observed that the contact offset term was non-zero ($d_0 \approx 2.2 \times 10^{-3}$ mm and 0.5×10^{-3} mm for the Perspex and alumnium loaders respectively). This meant that the compliance corrections were taken into consideration even when only slight contact is made between the loader and experimental sample.

The adustment to the displacement readings arising from compliance effects within the compression setup was typically between 0.001 and 0.100 mm. This was less than 1 % of the typical sample height. However, it was necessary to subtract the compliance readings from the output of the load cell when conducting the compression tests in order to give the true extent of the compression of the sample.

2.3.3 Offset Load

The data taken within the offset region was used to define the *offset load* l_0 which was a systematic non-zero load reading detected by the load cell. This resulted from small vibrations from the experimental apparatus, residual dust on the surface of the loader or incorrect calibration of the load cell. Calculation of l_0 was required in order to calibrate the load readings and determine the precise point at which contact between the loader and experimental sample was made. The data taken during this region also gave an indication of the extent of the noise fluctuations within the readings given by the load cell.

The load-displacement data taken during the first 1.5 mm of a sample compression test is shown in Figure 2.4. When viewed on a scale appropriate for the entire range used, the load values measured in the offset region are nearly con-

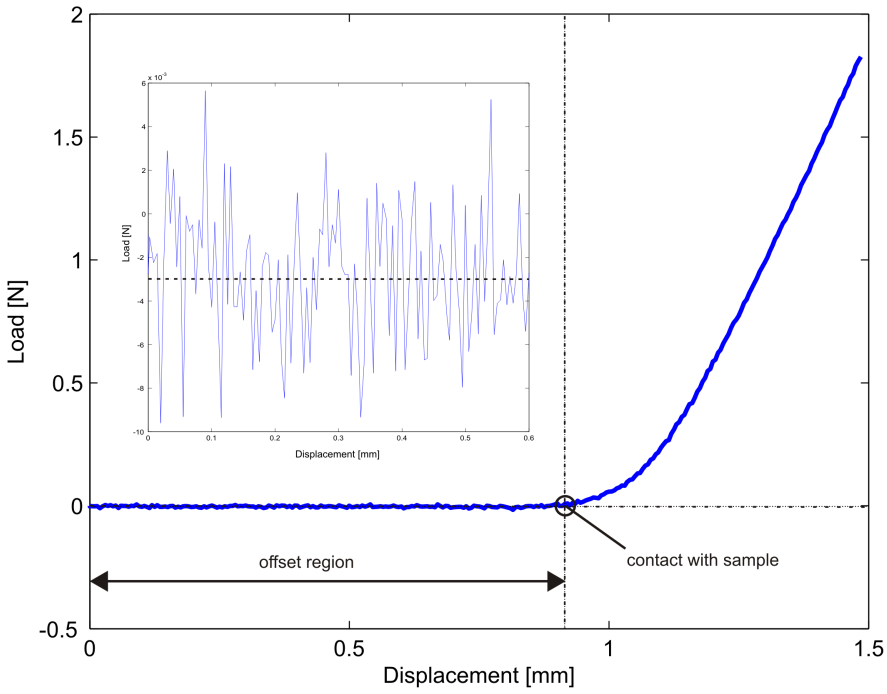

Figure 2.4: The load-displacement data taken during the offset region. This was used to identify background loading effects and determine the precise starting point of the compression test. The initial load values (inset) show a noisy signal l_0 = -0.0030 $\pm$ 0.0037 N which originated from mechanical vibrations in the experimental setup. The axis labels on the inset plot are the same as the larger plot. The black circle marks the point at which contact with the sample was made.

stant and approximately equal to zero. The load values shown in the inset figure, which is plotted on an expanded scale, indicate that they actually fluctuate about a non-zero average value during the initial compression range. For this data set the mean offset load was $l_0 = -3.0 \times 10^{-3}$ N and the standard deviation from this value was 3.7×10^{-3} N. As no contact was made between the loader and sample during this phase of loading, l_0 was subtracted from the load readings to give a more accurate load value and it is assumed that this effect was systematic throughout the loading process.

The point of contact with the sample was deemed to be the true starting point of the experimental test. This was calculated by considering the least-square fit of the load data to a constant l_0 value and inferring that contact was made at the point where the deviation of the load value from this l_0 exceeded the aforementioned standard deviation. In the data set shown in Figure 2.4 this was observed at a displacement of 0.92 mm from the starting position. All load values measured from this point on were considered to represent the region of contact between the sample and the loader.

2.3.4 Stress and Strain

The experimental load-displacement data was corrected by including the effects of the compliance and offset loads. This was then converted into the nominal stress σ and strain ϵ according to the definitions shown below.

$$\epsilon = \frac{\Delta h}{h} \tag{2.2}$$

$$\sigma = \frac{L}{A} \tag{2.3}$$

In equation (2.2) Δh (mm) is the magnitude of the displacement of the top surface of the structure and h is its original height (mm). In equation (2.3) L (N) is the load applied to the top surface of the experimental sample and A (m^2) is the undeformed area of its top surface.

In the data sets reported in this thesis compressive strain and stress measures are defined as positive values. The stress values are typically expressed in units of kPa and are normalised by the Youngs modulus E_s of the material from which the sample was made. This was performed in order to allow comparison of the strengths and stiffness of experimental samples made from different types or batches of material. Although the strain and normalised stress are dimensionless quantities, their units shall be expressed as mm/mm and kPa/kPa respectively so as to preserve their meaning.

2.4 Elastic Materials

The experimental samples were manufactured using the elastic materials[2] Sil AD Spezial, which was blue in colour, and Sil AD Soft (pink). The materials differed in their elastic properties but were prepared in exactly the same way: by mixing two fluids, a polyvinyl base and a siloxane catalyst in a 50:50 volume ratio. The fluids were separately decanted into 10 ml syringes to allow accurate measurement of their respective volumes, injected into a glass beaker and mixed using an aluminium stirrer. In order to manufacture the experimental samples, the fluid mixtures were allowed to set for an hour in the moulds described in Appendix B.

[2]Feguramed GmbH, Buchen, Germany

As stated in Section 2.3, the stress values were normalised by the Young's modulus of the bulk material E_s. It was necessary to determine this from experiments on the calibration samples using the aluminium loader. It was also possible from these tests to assess the sensitivity of the material's response to the speed at which compression tests were performed, material hysteresis effects and the influence of lubrication on the stress values.

2.4.1 Calibration Samples

Three calibration samples were made each time a new batch of the material was prepared. The manufacturing process consisted of pouring the fluid elastomer into cylindrical aluminium moulds (diameter 10.00 $\pm$ 0.05 mm, height 10.03 $\pm$ 0.06 mm) and allowing this to set for the same time as the main sample. This was deemed necessary as, although care was taken to ensure the correct measurement and thorough mixing of the fluid volumes, it was found that batches of material were not identical. Hence, the stiffness of the bulk material varied slightly between batches.

2.4.2 Rate Dependence and Hysteresis

Each calibration sample was compressed to a strain of approximately 0.25 mm/mm as this encompassed the strain ranges considered during tests on the main experimental samples. The stress-strain data taken during cyclic compression tests performed at 1.00 mms^{-1} (blue), 0.10 mms^{-1} (red) and 0.01 mms^{-1} (black) on a calibration sample of Sil AD Spezial have been plotted in Figure 2.5 (a). The arrows above and below the data sets indicate the loading (increasing ϵ) and unloading (decreasing ϵ) phases of the tests. The materials showed a rate-dependence which decreased as the compression speed was decreased; reducing the speed by a factor of 100 caused an average reduction of the σ values by 15 %. However, there

is a 3 % discrepancy between the loading phases of the red and black data sets. This observation is consistent with experimental observations that there is a finite response time in rubbery materials to high strain compression. This manifests itself as increased stress when compressed at high speeds [50, 51]. Another notable feature in the data taken at high speeds was a slight increase in σ as the direction changed, an effect which was not observed at lower speeds.

It is noteworthy that during the unloading phase of each of the data sets the stress values lie below those values recorded during the loading phase. These effects were reduced by applying a layer of Vaseline to the top and bottom surfaces of the calibration sample. In Figure 2.5 (b) a comparison between the calibration sample with unlubricated (green) and lubricated (pink) boundaries loaded and unloaded at a compression speed of 0.01 mms^{-1} has been presented. The hysteresis in the data taken on the lubricated sample has reduced from $\approx$ 10 % to less than 2 %, and the stress values have been reduced by approximately 20 %. This implies that the friction between the top and bottom surfaces of the sample and the loader and base served to stiffen the structure by restricting its transverse expansion as it was compressed.

Throughout the course of the experimental study, the compression tests were generally performed at slow speeds between 0.001 and 0.010 mms^{-1} to allow the acquisition of a large number of data points and to simplify sychronisation with the camera. Where loading-unloading experiments were conducted, Vaseline was applied to the sample as described in this section to allow accurate comparison between the data taken in the loading and unloading phases. The calibration tests for each test were performed at the same speed as the main test so as to completely replicate the experimental conditions.

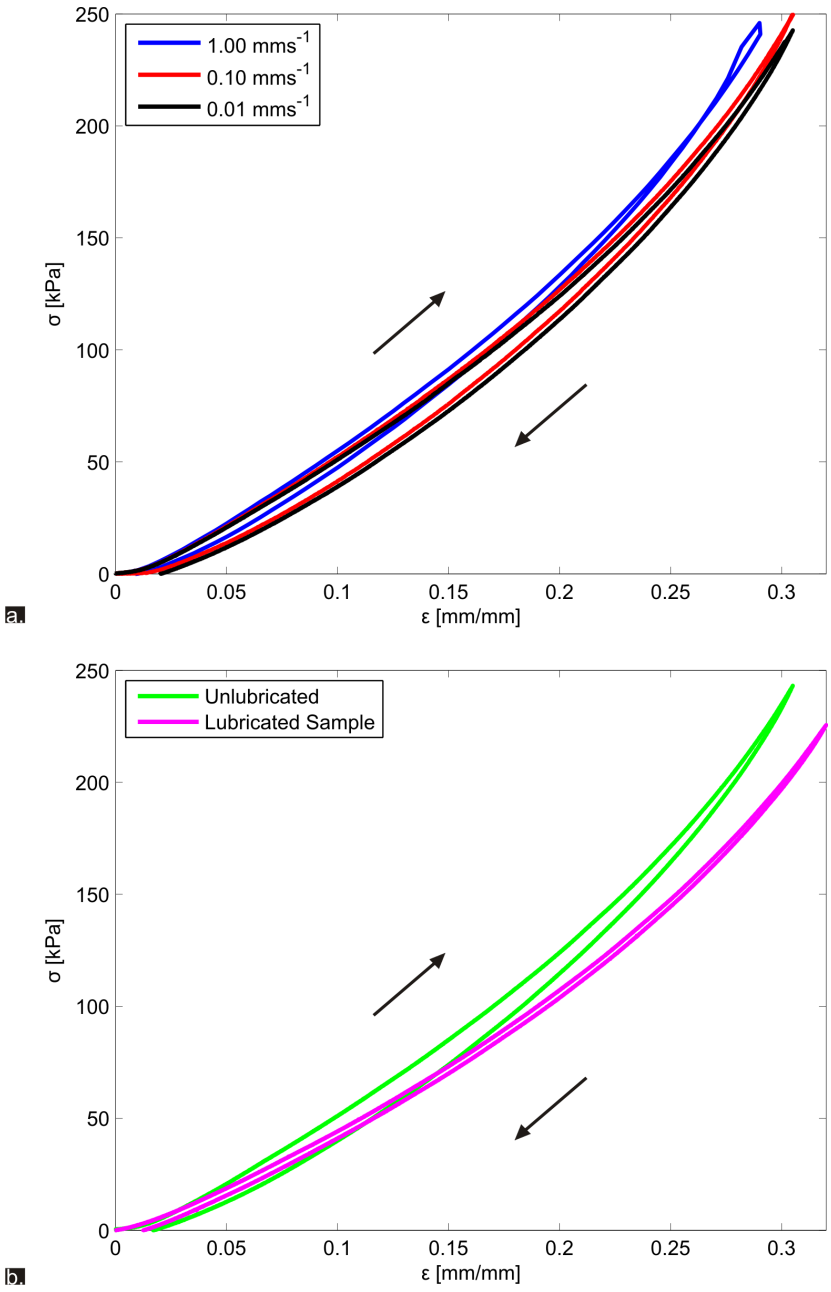

Figure 2.5: The stress-strain behaviour of the calibration samples under uniaxial compression. In (a) the data was taken at compression speeds 1.00 mms^{-1} (blue), 0.10 mms^{-1} (red) and 0.01 mms^{-1} (black). The two data sets plotted in (b) were taken on an unlubricated (green) and a lubricated sample at 0.10 mms^{-1} (pink).

2.4.3 Elastic Modulus

A standard technique for obtaining the Young's modulus of elastic materials is the fitting of stress-strain data to predictions arising from theoretical models of elastic structures [30]. The data taken during tests on the calibration samples was used to do this. Here, a comparison of three models - *Hookean* elasticity, *neo-Hookean* elasticity and the two-term *Mooney-Rivlin* model - is presented. A relationship between the axial stress σ and one-dimensional strain ϵ for isotropic, homogenous, nearly incompressible elastic materials under uniaxial compression has been derived from each model. The stress-strain relationship from the Hookean (equation (2.4a)), neo-Hookean (equation (2.4b)) and Mooney-Rivlin (equation (2.4c)) models are expressed as [30, 52]

$$\sigma = E\epsilon \tag{2.4a}$$

$$\sigma = 2C_1(1 - \epsilon - \frac{1}{(1-\epsilon)^2}) \tag{2.4b}$$

$$\sigma = (2C_1 + 4C_2(1 - \epsilon + \frac{1}{(1-\epsilon)^2} - 3))((1-\epsilon)^2 - \frac{1}{1-\epsilon}) \tag{2.4c}$$

In equation (2.4) E (Pa) is the Young's modulus which, along with C_1 (Pa) and C_2 (Pa), was determined by fitting equations (2.4) to experimental data. By considering the behaviour of equations (2.4b) and (2.4c) as $\epsilon \to 0$, the neo-Hookean and Mooney-Rivlin models reduce to

$$\sigma = 6C_1\epsilon \tag{2.5}$$

and the Young's modulus E is derived from both according to

$$E = 6C_1 \tag{2.6}$$

The Young's modulus was extracted from the calibration data by fitting equations (2.4) to the experimental stress-strain data collected during the tests on the calibration samples using GnuPlot. Here, the results of fitting equations (2.4) to the loading data for the unlubricated and lubricated calibration sample described in Section 2.4.2 are considered to show the effect of the lubrication layer on the stiffness of the material. The compression test was performed at 0.01 mms^{-1}.

The plots in Figure 2.6 are used to demonstrate the range across which each of the three proposed models replicates the experimental data, which is blue in each plot. The top data set has been collected on the unlubricated sample and the bottom on the lubricated sample. The results of fitting these data sets to equations (2.4a, red), (2.4b, black) and (2.4c, green) show that the two-term Mooney-Rivlin model provides the best approximation to the material behaviour across the full strain range covered during the experiments. The neo-Hookean model is accurate up to $\epsilon \approx 0.20$ mm/mm. The lack of agreement between the Hookean model and the experimental data implies that there is only a small range of strain in which the material can be considered linearly elastic under uniaxial compression. In the calibration data, the average deviation of the models from the experimental data was ≈ 50 % for the Hookean and ≈ 25 % for the neo-Hookean models. This discrepancy reduced to ≈ 2 % for the Mooney-Rivlin model which is further evidence of its appropriate fit.

In Table 2.2 the Young's modulus of the bulk material as determined by fitting the Hookean (E_H), neo-Hookean (E_{NH}) and Mooney-Rivlin (E_{MR}) models

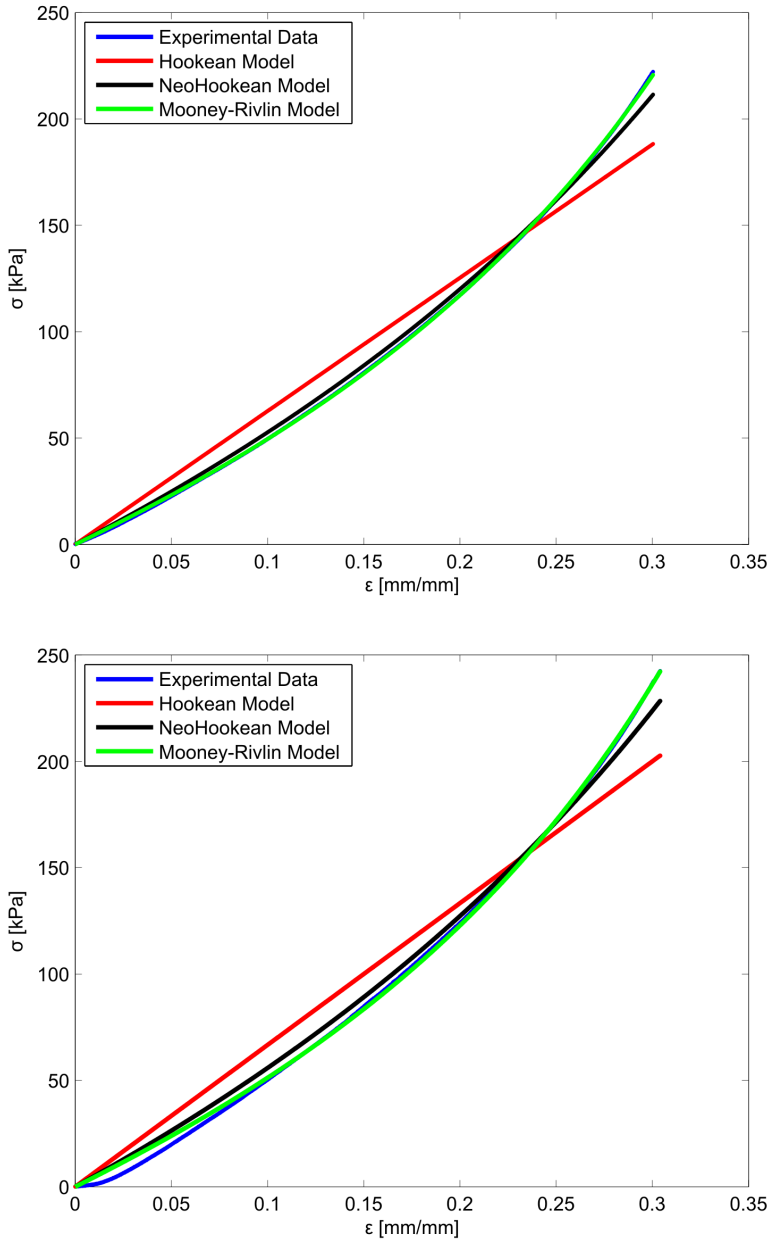

Figure 2.6: Fitting elasticity models to the experimental data (blue). The stress-strain equations proposed by Hookean (red), neo-Hookean (black) and Mooney-Rivlin (green) models replicate the experimental measurements with a varying degree of accuracy. Both the experimental data sets taken for the unlubricated (top) and lubricated calibration sample are well captured by the Mooney-Rivlin model.

	E_H (kPa)	E_{NH} (kPa)	E_{MR} (kPa)
Unlubricated	666.55	500.65	452.29
Lubricated	626.65	472.21	439.25

Table 2.2: The Young's modulus values obtained by fitting equations (2.4a), (2.4b) and (2.4c) to the experimental stress-strain data. The Young's modulus is used to normalise the stress values measured in later experiments.

to the experimental data have been recorded. Analysis of the results shows that the application of Vaseline to the sample reduced the stiffness determined by each model by approximately 5 %. There was a 10 % discrepancy between the stiffness values calculated using equations (2.4b) and (2.4c) which suggests that both models can be considered accurate in conveying the response of the bulk material to uniaxial loading. However, the bulk material stiffness values quoted here will be those calculated using the Mooney-Rivlin model because of its good agreement with the experimental data over the full range of strain used in the experiments. In this thesis, E_s is an average value calculated across three calibration samples and the error is the standard deviation from this mean value.

2.5 Summary

The experimental apparatus and techniques used during the study have been described. Whilst the principle behind the experiments is simple, a number of precautions have been taken in order to ensure accuracy in the data measurements. The calculation of the Young's modulus of the material used in manufacturing the experimental samples has provided a test-case for the procedures described here. Using these techniques it has been shown that the material behaves as a Mooney-Rivlin solid under uniaxial compression.

Chapter 3

Elastic Buckling in a 2D Cellular Structure

Uniaxial compression tests were performed on a regular two-dimensional cellular structure. The structural geometry consisted of an 8×8 array of circular cells arranged on a square lattice. A repeatable geometric transformation was observed whereby the initially circular voids formed a pattern-switched state of mutually orthogonal ellipses. Both the aspect ratio of the voids and the normalised stress varied linearly with the strain applied to the sample prior to the switch in the cellular geometry. In the pattern-switched state the aspect ratio had a square root dependance on the applied strain, and the normalised stress was approximately constant. The transition in the cellular geometry was shown to occur at a critical stress-strain point and a secondary pattern-switched state was shown to exist. In this state the ellipses were oriented orthogonally to their orientation in the primary state and in unloading experiments this state became unstable.

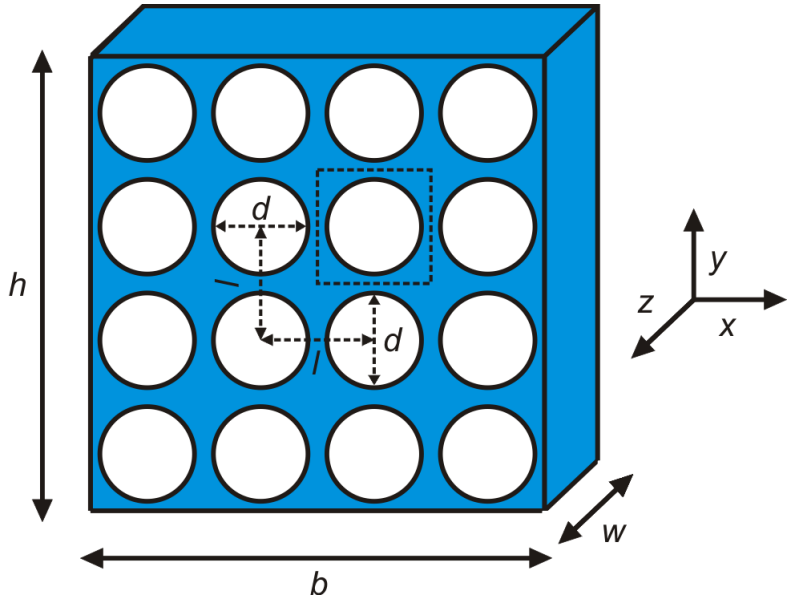

Figure 3.1: The csa-lattice. The cellular structure geometry comprised circular voids (diameter d) cut from a sheet of elastic material (blue). The voids were arranged on a square lattice with inter-hole spacing l in the $x-$ and $y-$ directions.

3.1 Two-Dimensional Cellular Structures

3.1.1 The csa-Lattice

The experiments described in this chapter were performed on a two-dimensional cellular structure with a regular, repeating planar geometry. A sketch of this geometry is shown in Figure 3.1. In the sketch an array of circular voids of diameter d in a sheet of elastic material (height h and breadth b) are shown. The centres of neighbouring voids are separated by a distance l in both the x- and y- directions and these values are constant through the out-of-plane width w of the sample.

The cellular structure sketched in Figure 3.1 can be described in numerous ways. For example, it can be considered to be a "square lattice (or array [2])

of circular holes" which occupies a an "elastomeric matrix [6]". The terms "grid of circular voids" or "circular-cell honeycomb" are also equally apt. In giving a name to the structure it was key that two aspects of its planar geometry were conveyed. These were the circular shape of the cells and the fact that the spacing was the same in each planar direction. However, another requirement was brevity, particularly given that repeated references are made to the structure throughout this thesis. For this reason, the naming convention adopted here was inspired by that used to classify crystal geometries in solid-state physics [33]. The structure depicted in Figure 3.1 shall be henceforth referred to as a *csa-lattice*, where the initial *c* stands for "circular" (to reflect the cell shape) and, *sa* stands for "square array" (to reflect the arrangement of the cells). This naming convention lends itself to other 2D cellular geometries which will be discussed in Chapter 4.

3.1.2 Planar Geometry

The planar geometry of the csa-lattice shall be defined by three measures here. The first are the number of rows n and columns m of voids in the structure. The third is the *void fraction* Φ[1] which is the proportion of the lattice volume taken up by the circular voids. This is calculated as

$$\Phi = \frac{\pi d^2}{4l^2} \tag{3.1}$$

where d and l have the definitions given in Section 3.1.1 and no additional boundary widths have been applied to the finite sample. This means that the void fraction of the csa-lattice is equal to that of the unit cell, which has been highlighted by the dashed box in Figure 3.1. The unit cell is a square of side l which, together with

[1]The void fraction should not be confused with the *relative density* $\frac{\rho^*}{\rho_s}$ which is the proportion of the lattice made up of the solid material [3].

the void it encloses, is the smallest repeating block which represents the planar geometry. Henceforth, an experimental sample which has the geometry described in this section will be referred to as an $n \times m$ csa-lattice (Φ).

3.1.3 Uncertainties

The experimental samples were made from addition-curing fluid elastomers using the moulding technique described in Appendix B. The fractional uncertainty in void fraction $\frac{\delta\Phi}{\Phi}$ was estimated by adding the experimental errors in l and d (δl and δd respectively) in quadrature. This yields

$$\frac{\delta\Phi}{\Phi} = 2\sqrt{\left(\frac{\delta l}{l}\right)^2 + \left(\frac{\delta d}{d}\right)^2} \tag{3.2}$$

In the experiments the void size was fixed such that $d = 8.79 \pm 0.09$ mm. l had values ranging between 10.00 - 20.00 mm to allow different Φ values to be considered and δl was approximately 0.2 mm. This meant that in the experimental studies $\frac{\delta\Phi}{\Phi} \approx 0.03$.

3.2 Uniaxial Compression of a csa-Lattice

The results presented in this chapter were measured in compression experiments performed on one particular experimental sample. Specifically, this was an 8×8 csa-lattice ($\Phi = 0.65$).

3.2.1 The Pattern Switch

The images shown in Figure 3.2 are of the experimental sample at differing stages of compression during a loading test performed at 0.005 mms^{-1}. In Figure 3.2 (a)

$\epsilon = 0.01$ mm/mm and the voids have been compressed in the direction of loading. During this *pre-buckling* phase of compression the voids in the sample will be referred as possessing a *homogeneous* geometry. This represents the *trivial state* of the csa-lattice, in which all of the voids have the same shape and orientation relative to the applied load.

In Figure 3.2 (b) ($\epsilon = 0.05$ mm/mm) each void has transformed into an ellipse. The symmetry of the homogeneous geometry has been broken by a switch to an array of mutually orthogonal ellipses. This cellular pattern is repeated by a translation over two cells in both the x- and y-directions, i.e. the unit cell has expanded such that it encloses four voids. The cellular pattern is no longer invariant upon reflection about two orthogonal axes with origin at the centre of the sample. However, it remains rotation invariant. In terms of the symmetry operations of the planar geometry, its invariance group reduces from the D_4 (dihedral) group to the Z_4 (cyclic)[2] group as a result of the pattern switch [53].

The top and bottom boundaries prohibited the pattern from forming fully close to these points in the sample, but elsewhere the pattern was clearly defined. This pattern switch was reversible and repeatable; recompression of the sample caused each void to become an ellipse with the same orientation as in the initial compression test. The *pattern-switched* geometry described above characterised the form of the csa-lattice during the *post-buckling* phase of compression.

The images shown in Figure 3.2 (c) and Figure 3.2 (d) are close-up views of the sample where the central four voids are shown in detail. The white diamond shapes represent the position and orientation of nine surrounding *connectors* at which the

[2]i.e. the number of elements in the group reduces from 8 to 4.

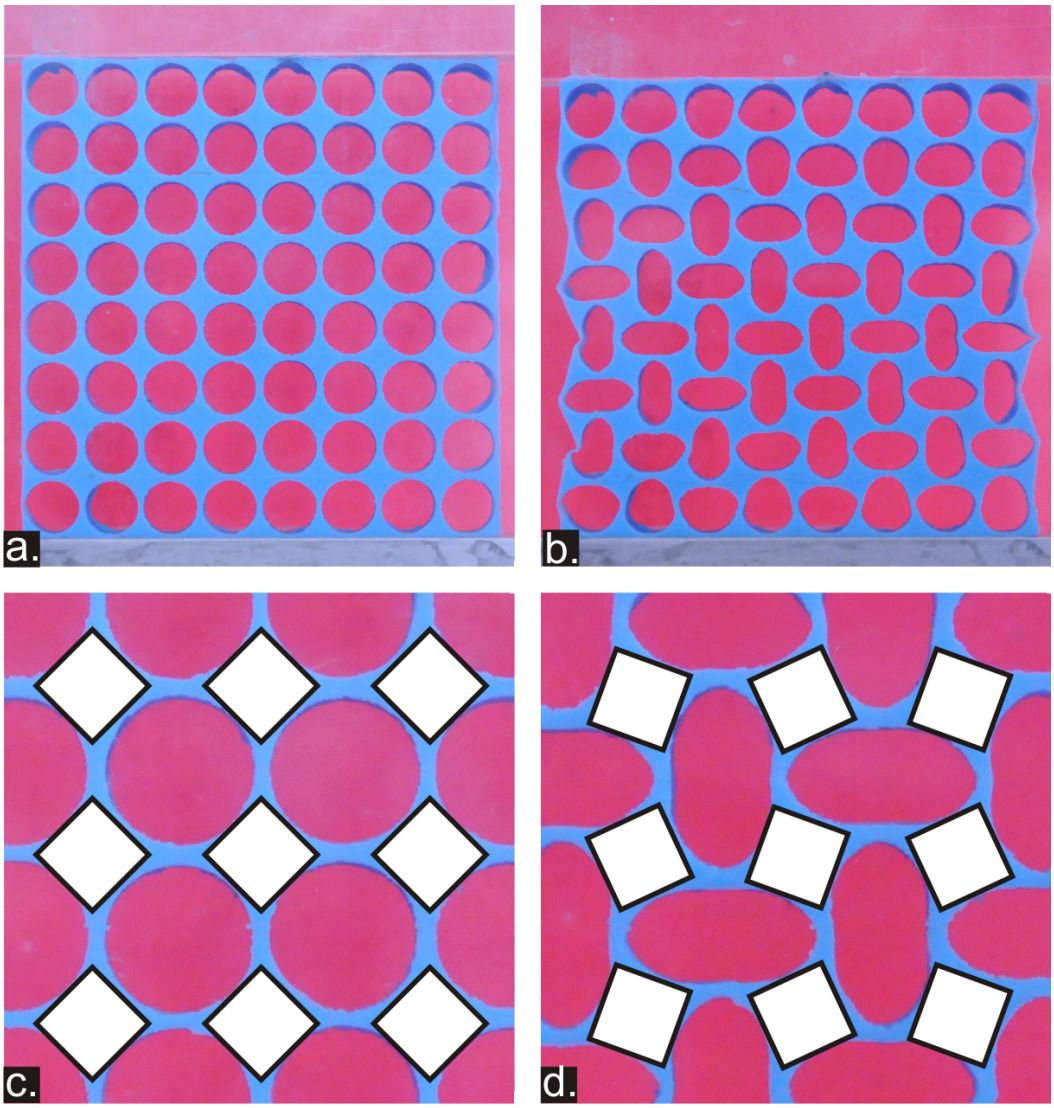

Figure 3.2: The homogenous and pattern-switched geometries. The experimental sample is shown at $\epsilon = 0.01$ mm/mm in (a) and (c) and at $\epsilon = 0.05$ mm/mm in (b) and (d). The bottom images, (c) and (d), are of the central four voids. The inter-ligament connectors (white) were observed to behave as rigid units and rotation of these was associated with the pattern onset.

vertical and horizontal ligaments meet in the csa-lattice. In the pre-buckling phase the connectors were co-aligned, and the compression of the sample reduced their separation in the y-direction. In the post-buckling phase the connectors rotated in opposite senses to their neighbours and this was associated with the buckling of the ligaments. This rigid-body rotation mechanism is an essential part of auxetic behaviour in cellular structures [48, 49], and the pattern switch described here has been shown to exhibit negative Poisson's ratio behaviour [6]. In the context of experiments on the csa-lattice, this observation is made to highlight the fact that the compression of the structure leads to high localised strains in the ligaments [26]. However, the dimensions of the connectors do not noticeably change as a result of this process.

3.2.2 Aspect Ratio

The *primary state* of the csa-lattice was the equiliibrium state of the structure which formed continuously with increased applied strain. In the experiments the primary state was split up into two parts, which were the pre- and post-buckling phases described in Section 3.2.1. It was desired to determine the precise point at which the transition between these two phases, and hence the switch in the cellular pattern, occurred. This point will henceforth be referred to as the *critical point* of the csa-lattice. To find the critical point, the aspect ratio γ (mm/mm) of the voids was monitored. This was defined as

$$\gamma = \frac{a}{b} \tag{3.3}$$

where a (mm) and b (mm) were the major and minor diameters of the voids respectively. For voids forming horizontal ellipses relative to the direction of loading, a was its vertical diameter and b its horizontal diameter. The inverse was true for

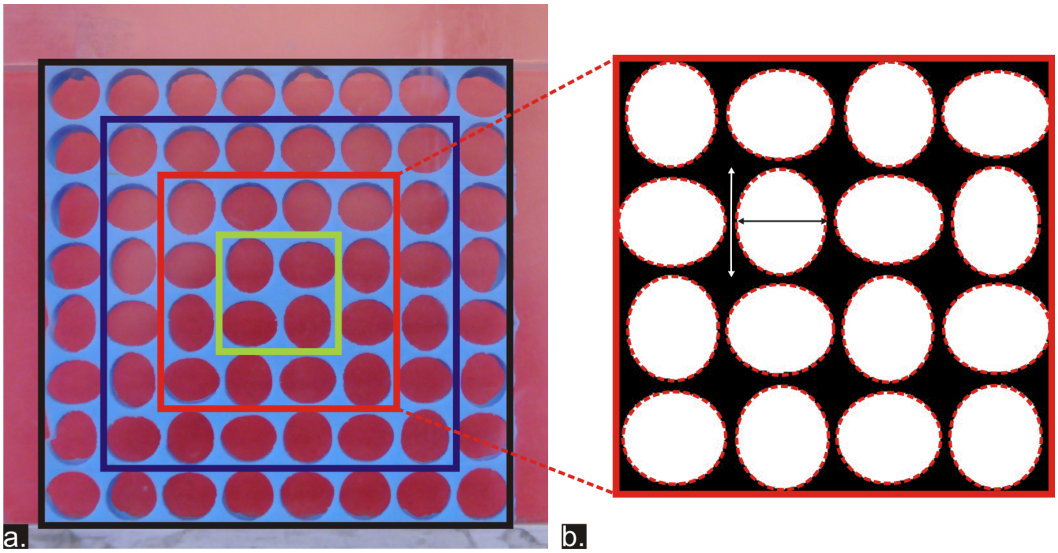

Figure 3.3: The image analysis method. The image of the sample (a) was analysed using the MATLAB : Image Processing Toolbox with a greyscale filter. The coloured lines represent the four regions of voids which were considered in calculating the γ values. The cropped images were binarised as shown in (b) and the subsequent analysis yielded the minor and major diameters of the voids.

voids which formed vertical ellipses.

The process for measuring γ is illustrated in Figure 3.3. A photo of the sample under applied strain ϵ was binarised using the MATLAB : Image Processing Toolbox by passing the image through a red/blue filter and then a greyscale filter. This filter was typically 0.65 although this was dependent on the ambient lighting and so required adjustment in some experiments. The image was cropped to contain a central square array of voids and it was then inverted such that the voids were white and the elastic material black. This process was performed on 8×8, 6×6, 4×4 and 2×2 cell arrays as indicated by the coloured lines in Figure 3.3 (a). The inverted image in Figure 3.3 (b) is of the 4×4 array.

The MATLAB *bwboundaries* function was then used to detect the continuous boundaries of the voids selected within the image. Statistical information was thereby gained of the major and minor diameters of the voids, as well as their orientation. The average aspect ratio was calculated using equation (3.3) for the horizontal (γ_h) and vertical (γ_v) ellipses. This process was repeated for images taken at strain intervals of 1.25 $\times$ 10^{-3} mm/mm in the range ϵ = 0.00 - 0.06 mm/mm to produce γ-ϵ plots for each orientation of the ellipses in the pattern-switched geometry.

In Figure 3.4 γ_h-ϵ (circles) and γ_v-ϵ (triangles) have been plotted for the csa-lattice. The sample was compressed at a speed of 0.005 mms^{-1} during this test. Discussion of the exact form of the data will be given in Section 3.2.3. The γ_h and γ_v values lie within their respective standard deviations and so it can be concluded that the pattern switch affected the voids in the same way regardless of their orientation in the switched geometry. For this reason γ, the mean of the γ_h and γ_v, shall be presented in later plots.

The forms of all γ-ϵ plots were qualitatively similar although the γ values and their standard deviation decreased as the number of cells was reduced. This was because both the 8 $\times$ 8 (black, Figure 3.4 (a)) and 6 $\times$ 6 (blue Figure 3.4 (b)) arrays contained voids whose shape was affected by the fixed boundaries at the top and bottom of the sample. This effect was reduced for the data taken on the 4 $\times$ 4 (red, Figure 3.4 (c)) and 2 $\times$ 2 (green, Figure 3.4 (d)) arrays of voids. For the purpose of analysis, the 4 $\times$ 4 γ-ϵ data set was considered representative of the change in the cellular geometry in the sample.

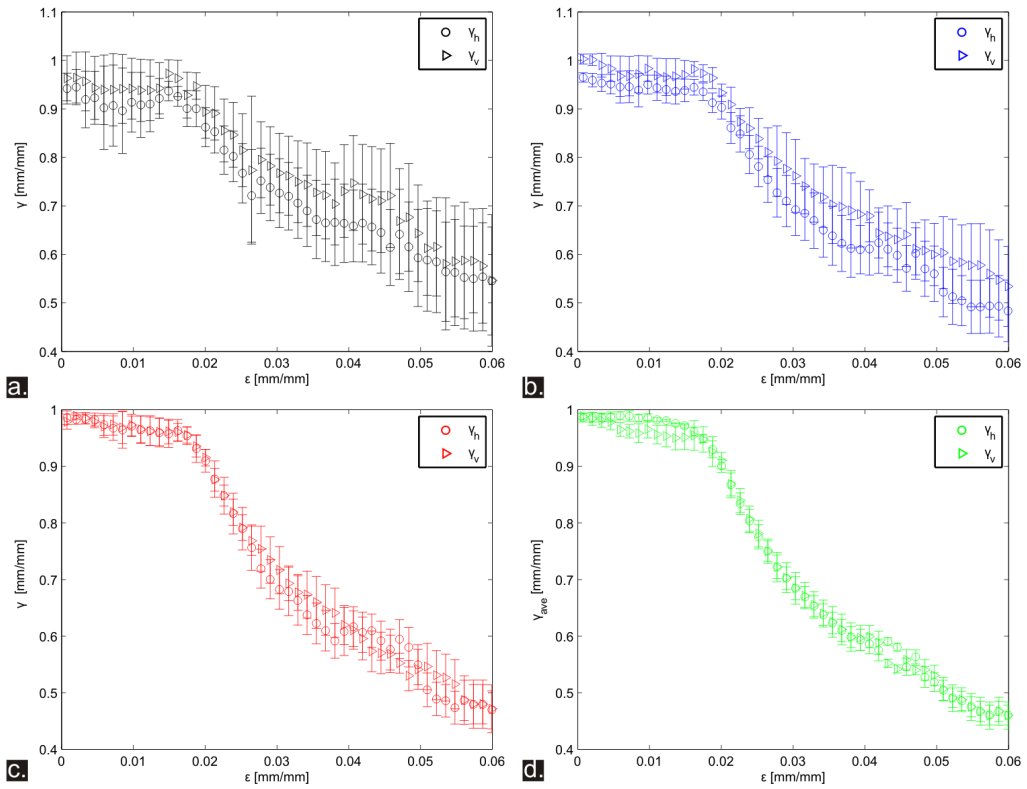

Figure 3.4: The variation of γ_h (circles) and γ_v (triangles) with ϵ. The measures were taken across 8×8 (black, a), 6×6 (blue, b), 4×4 (red, c) and 2×2 (green, d) square arrays of voids.

3.2.3 Pattern Onset

The γ-ϵ plot for the experimental sample is presented in Figure 3.5 (a) where the experimental data is red. Two distinct regimes of behaviour were observed which corresponded to the pre- and post-buckling phases of compression. During the pre-buckling phase of compression, γ decreased linearly with ϵ according to the function

$$\gamma_I = \gamma_0 - \Gamma_I \epsilon \tag{3.4}$$

where the factor Γ_I (mm/mm) linked the macroscopic deformation of the sample to its local value and γ_0 (mm/mm) was the initial aspect ratio of the voids. Fitting equation (3.4) to the experimental data using GnuPlot yielded $\Gamma_I = 1.94 \pm 0.15$ mm/mm and $\gamma_0 = 1.006 \pm 0.001$ mm/mm. This value of γ_o was suitable given the initially circular shape of the voids. The linear fit is demonstrated by the black extrapolated curve in Figure 3.5 (a).

At higher values of ϵ there was a departure from the linear behaviour to an approximate square-root γ-ϵ relationship. This characterised the change in γ in the post-buckling phase and further compression of the sample caused the enhancement of the pattern, lowering the aspect ratio of the orthogonal ellipses. The extrapolated γ_I function was subtracted from the γ values and the result of this is shown in Figure 3.5 (b). The adjusted values had the form associated with one equilibrium branch of an unperturbed pitchfork birfucation and the data was approximated by the relationship

$$\gamma - \gamma_I = -\Gamma_{II}\sqrt{\epsilon - \epsilon_{cr}} \tag{3.5}$$

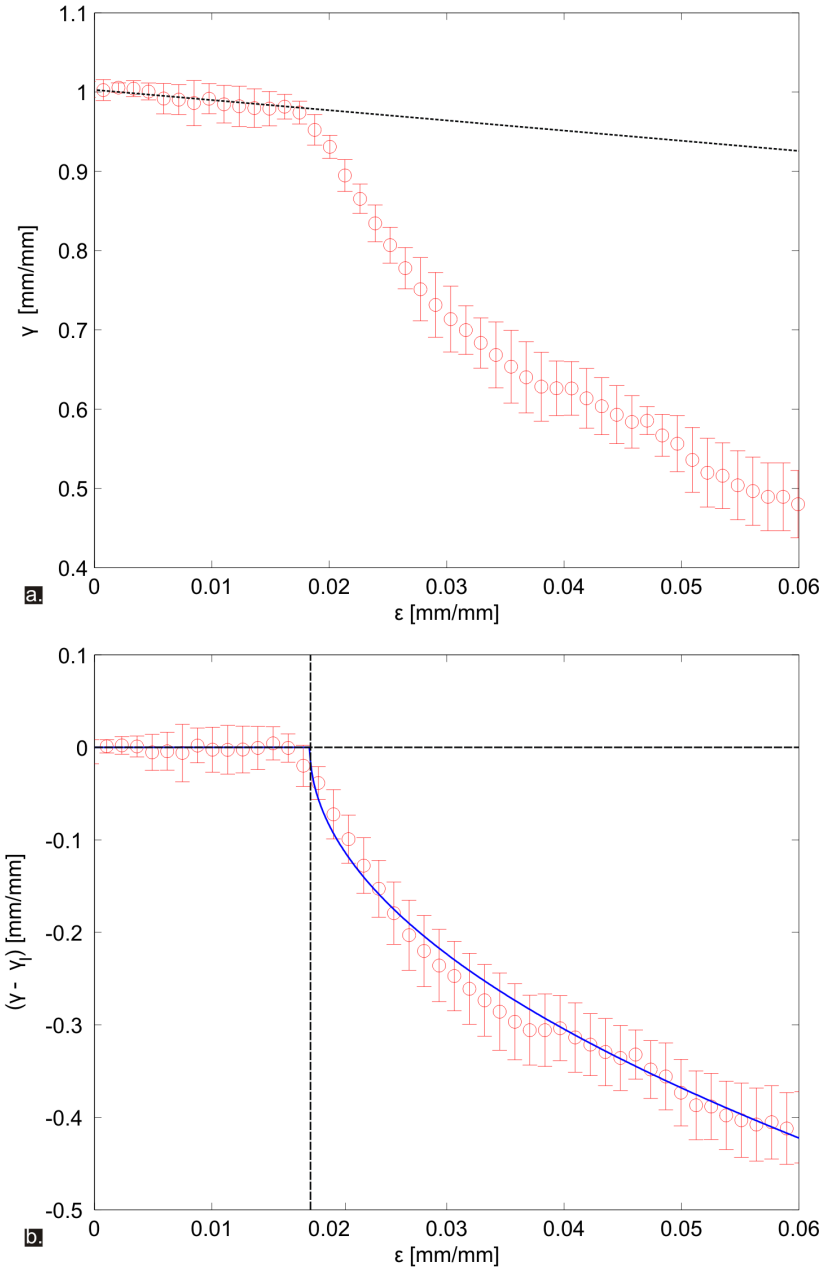

Figure 3.5: Determining the critical point. (a) The γ-ϵ plot for the 8 $\times$ 8 csa-lattice ($\Phi = 0.65$) was initially linear. In the post-buckling phase the variation of γ - γ_I (red) with ϵ was well-captured by equation (3.5) (blue) (b). The vertical dashed line marks an estimate of onset of instability in the experiment.

As with the measure Γ_I in equation (3.4) Γ_{II} gave an indication of the interaction between large- and small-scale changes in the structural geometry of the sample. In Figure 3.5 (b) a least-squares fit of equation (3.5) (blue) has been plotted alongside the experimental data (red) and the two show excellent agreement. For the data set considered here $\Gamma_{II} = 2.069 \pm 0.015$ mm/mm and $\epsilon_{cr} = 0.184 \pm 0.001$ mm/mm. The vertical dashed line marks the *critical strain* ϵ_{cr} which is the boundary between the pre- and post-buckling compression phases in the experiment.

3.2.4 Normalised Stress-Strain Data

The normalised stress-strain curve for the sample is shown in Figure 3.6. As with the data described in Section 3.2.3, the plot can be divided into two distinct phases. During the Hookean phase of compression (AB) $\frac{\sigma}{E_s}$ increased linearly with ϵ. In the *plateau* phase (CD) $\frac{\sigma}{E_s}$ was near constant despite the increased compression of the csa-lattice. These features of the data are common features of numerical and experimental studies of cellular structures, where elastic buckling of the structure has been observed to lead to two-phase normalised stress-strain behaviour [2, 3, 5, 22, 26].

The boundary between the two phases of loading is consistent with that determined by analysis of the aspect ratio of the voids. The vertical dashed line marks the ϵ_{cr} value (0.0184 ± 0.001 mm/mm) calculated using the curve-fitting procedures described in Section 3.2.3. It is clear that the Hookean phase of loading was associated with the homogeneous geometry of the voids whereas in the plateau phase the voids had the pattern-switched geometry. The action of load on the csa-lattice, therefore, is to cause the structure to buckle at the critical point, and it is this buckling which causes the formation of the elliptical pattern.

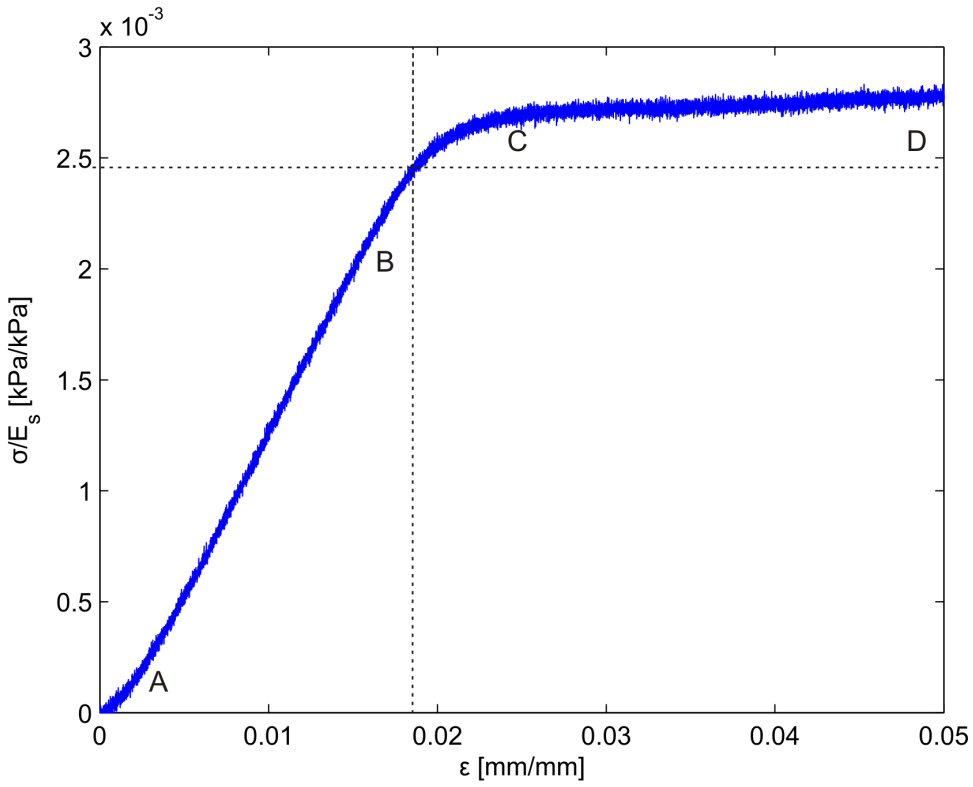

Figure 3.6: The normalised stress-strain data of the csa-lattice. The data exhibited the two-phase behaviour which characterises the response of cellular structures to compression tests. The vertical dashed line marks ϵ_{cr} and the horizontal dashed line represents the normalised critical normalised stress $\frac{\sigma_{cr}}{E_s} = 2.43 \pm 0.02 \times 10^{-3}$ kPa/kPa.

Analysis of the normalised stress-strain data allowed identification of two measures which will be used characterise the response of the csa-lattice to uniaxial loading. The *normalised critical stress* $\frac{\sigma_{cr}}{E_s}$ is a quantitative measure of the *strength* of the structure. It is the normalised stress value at the transition point i.e.

$$\frac{\sigma_{cr}}{E_s} = \frac{\sigma(\epsilon_{cr})}{E_s} \tag{3.6}$$

and this has been indicated in Figure 3.6 by the horizontal dashed line. The *normalised elastic modulus* $\frac{E}{E_s}$ of the structure was the gradient of the normalised stress-strain curve in the Hookean phase [3]. This is used to evaluate the *stiffness* of the csa-lattice under uniaxial compression. Here $\frac{\sigma_{cr}}{E_s} = 2.43 \pm 0.02 \times 10^{-3}$ kPa/kPa and $\frac{E}{E_s} = 1.45 \pm 0.01 \times 10^{-1}$ kPa/kPa.

The coordinates of the critical point[3] (ϵ_{cr}, $\frac{\sigma_{cr}}{E_s}$) are used to mark the onset of instability in the csa-lattice. In the buckling of perfect 2D cellular structures the critical and plateau stresses coincide and the boundary between the pre- and post-buckling phases is sharp and well-defined [3]. *It is neccessary to discuss here the subtle difference between thebifurcation in the csa-lattice and its failure. The onset of the bifurcation is defined as the point at which the microscopic (i.e., inner) features of the cellular structure changde and it is this process which, ultimately, leads to the failure of the structure. There is some delay between these two events as the transition between the Hookean and plateau phases is rounded as opposed to sharp.*

In considering this point it is important to remember that the γ values have only been measured across the central 4 × 4 square of voids in the structure for

[3]This is often referred to as the initiation point of the structure [5]

accuracys sake whereas the stress values are measured across the sample, boundaries included. It should be expected, therefore, that some rounding effects will occur as a result of the non-uniform pattern transformation in regions close to the boundary and where imperfections may take their toll. As discussed by Bertoldi and Boyce [26] in infinite structures the macroscopic and microscopic failure surfaces overlap and as such, it may possible in experiments on larger lattice sizes that a sharper transition between the plateau and Hookean regimes occurs. Naturally, in such a structure a larger proportion - if not all - of the constituent voids could be considered in determining the bifurcation point. As described in Section 3.2.2 the aim of the analysis described here was to find an accurate experimental analysis technique to estimate the instability onset in the finite csa-samples. This would allow comparison with numerical simulations such as those carried out by Bertoldi et al using eigenvalue analysis on a perfect planar geometry [6, 26]. These showed that pattern onset occurred prior to the commencement of plateau stress behaviour and the results described here are consistent with these observations.

3.2.5 Repeatability, Rotation and Rate Dependence

The data analysed in Sections 3.2.3 and 3.2.4 was taken during one experimental run at a compression speed of 0.005 mms^{-1}. In Figure 3.7 the variation of $\frac{\sigma}{E_s}$ (a) and γ (b) with ϵ measured during experiments at compression speeds 0.005 mms^{-1} (red), 0.010 mms^{-1} (blue) and 0.100 mms^{-1} (green) are shown. It is notable in Figure 3.7 that the normalised stress values associated with applied strain decreased as the speed was increased. This is contrary to the previous observation in 2 that stiffness of the bulk material increases with the compression speed. This softening may have come about by repeated compression of the material as the experiments were performed in order of increasing speed. However, the deviation between the norrmalised stress is less than 5% which is within acceptable

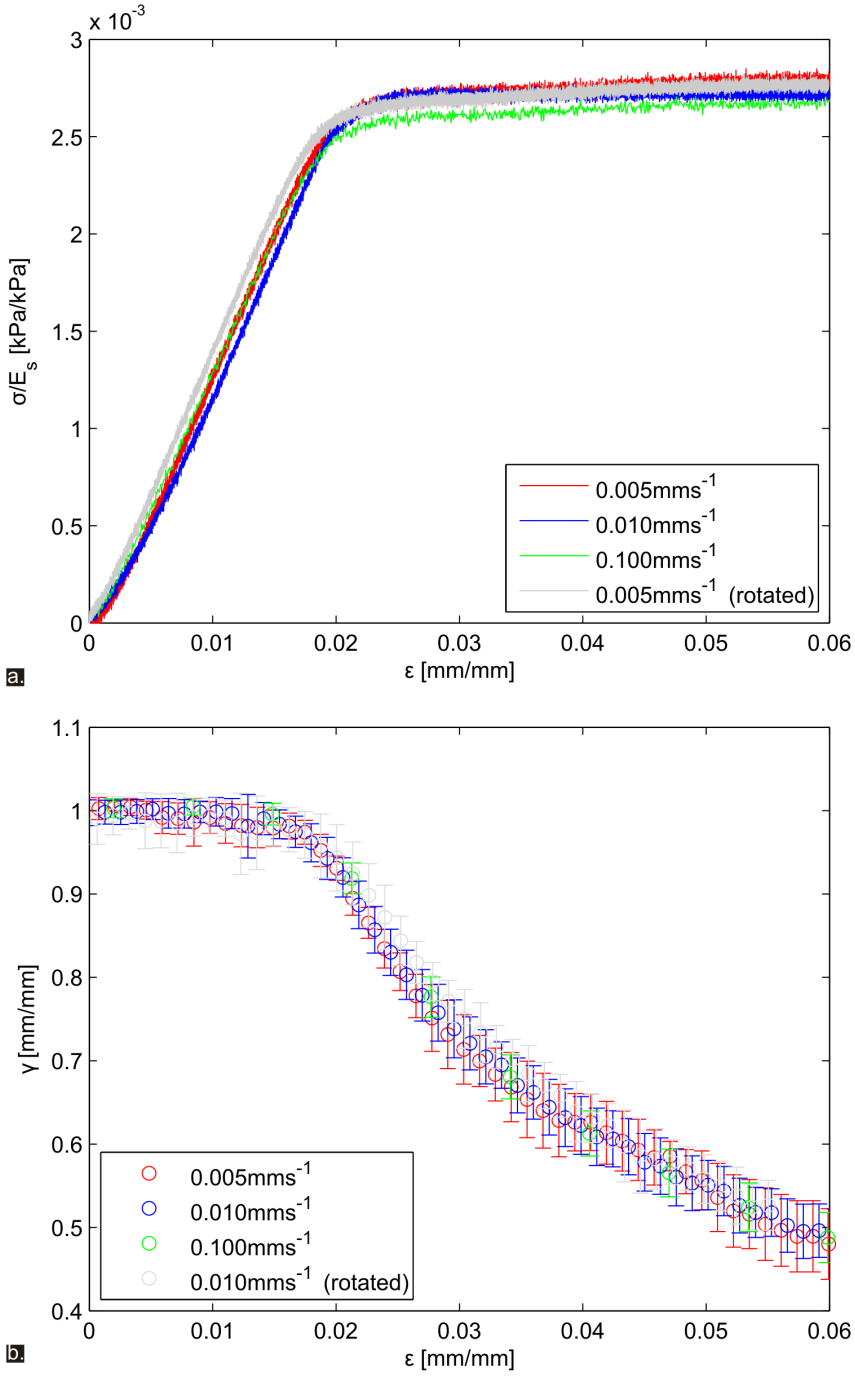

Figure 3.7: Rate dependence of the experimental data. $\frac{\sigma}{E_s}$ (a) and γ (b) have been plotted with ϵ for experiments taken at different speeds. Both parameters are rate invariant over the range 0.005 mms^{-1} - 0.100 mms^{-1}.

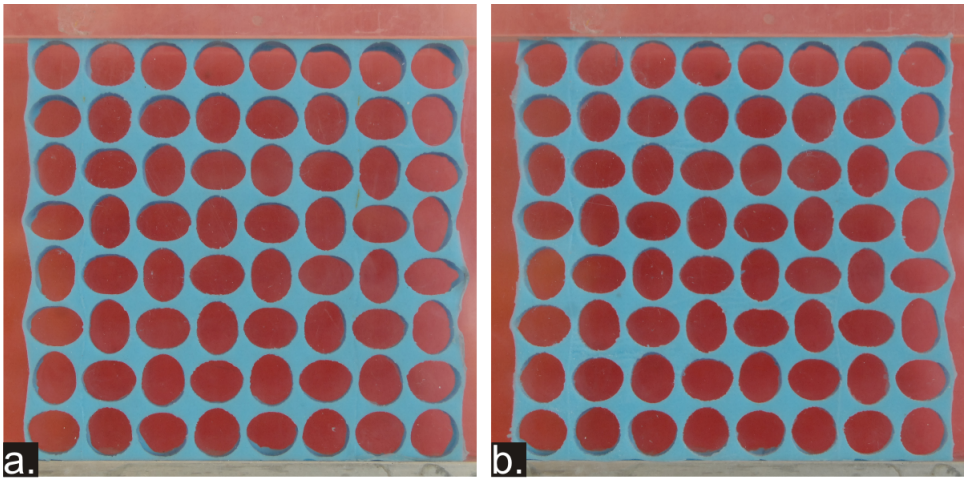

Figure 3.8: Rotation dependence of the pattern-switched geometry. The images are of the sample at $\epsilon = 0.03$ mm/mm in the initial (a) and rotated (b) configurations to demonstrate the rotation invariance of cellular geometry in the post-buckling phase.

experimental error. As such the data is considered repeatable for the purpose of calculating average ϵ_{cr}, $\frac{\sigma}{E_s}$ and $\frac{E}{E_s}$ parameters for the sample. These were $\epsilon_{cr} = 0.0175 \pm 0.0012$ mm/mm, $\frac{\sigma}{E_s} = 2.45 \pm 0.02 \times 10^{-3}$ kPa/kPa and $\frac{E}{E_s} = 1.47 \pm 0.04 \times 10^{-1}$ kPa/kPa respectively.

The fourth data set (grey) shown in Figure 3.7 was taken on the sample when rotated 90^o about its centre and compressed at a speed of 0.010 mms^{-1}. The experimental data shows excellent agreement with that taken in the initial tests which implies that the structure buckles at the same point regardless of its orientation in the housing. In Figure 3.8 the sample is shown in its buckled state at $\epsilon = 0.03$ mm/mm in the initial (Figure 3.8 (a)) and rotated (Figure 3.8 (b)) configurations. The patterns are identical; where a void formed a horizontally aligned ellipse in post-buckling phase of the primary state, it formed a vertical

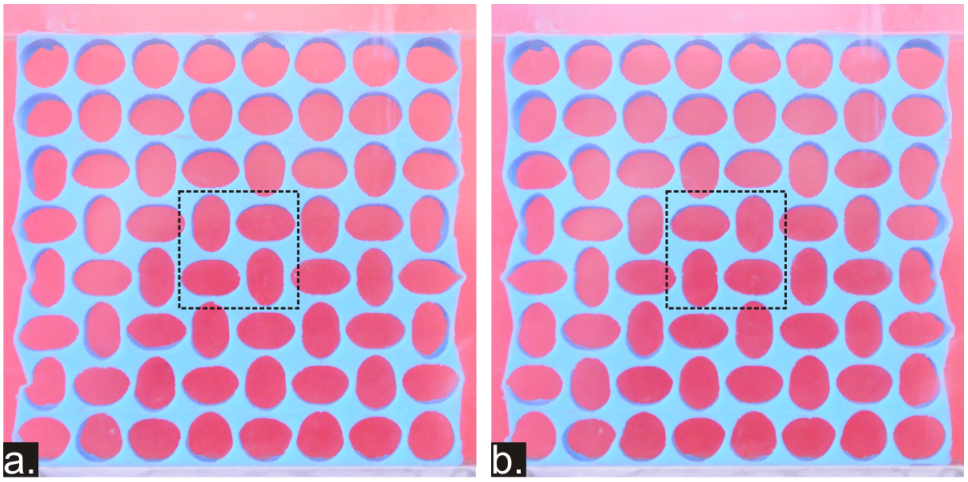

Figure 3.9: The primary (a) and the secondary (b) pattern-switched states. The sample is shown at $\epsilon = 0.05$ mm/mm in both images. Both states consist of mutually orthogonal ellipses and are related to one another by a rotation of the cells by 90^o about their centres.

ellipse when the sample was rotated by 90^o about its centre and recompressed.

3.3 Secondary State

The critical behaviour described in Section 3.2 related to the continuous primary state of the csa-lattice. There was a *secondary state* in which each void formed an ellipse during the post-buckling phase which was aligned orthogonally to its orientation in the primary state. The sample is shown in Figure 3.9 at $\epsilon = 0.05$ mm/mm during the post-buckling phase in both the primary (Figure 3.9 (a)) and the secondary states (Figure 3.9 (b)). The two images are indistinguishable but for the relative rotation of the cells by 90^o about their centres.

3.3.1 Methodology

It was not possible to achieve the secondary state via the continued increase of applied strain to the sample from zero strain. This was because the secondary state was the stable branch of a disconnected saddle node and could not be attained by following the continuous equilibrium branch of the sample. Instead, the existence and stability of this state was investigated by pre-straining the experimental sample past ϵ_{cr} such that the switched geometry associated with the primary state was formed. The secondary state was then induced by removing the front plate of the housing and using tweezers to rotate one of the interstitial connectors in the opposite sense to which it had already rotated. This caused the surrounding connectors in the csa-lattice to switch their orientation by 90^o in a avalanche event which demonstrated the high degree of coupling of the ligaments in the sample. Once the sample was in the secondary state, the front plate of the housing was replaced and an unloading experiment was performed in order to determine its stress-strain response in this state.

3.3.2 Primary vs Secondary State

In order to differentiate between the two states, the *modified aspect ratio* γ^* is introduced here. It is defined as

$$\gamma* = \lambda(1 - \gamma) \tag{3.7}$$

where

$$\lambda = \begin{cases} +1 & \text{if the structure is in the primary state} \\ -1 & \text{if the structure is in the secondary state} \end{cases}$$

In Figure 3.10 (a), the variation of γ^* has been plotted for two unloading experi-

ments. Both tests were performed at a speed of 0.005 mms^{-1}. This slow speed was necessary in order to resolve the bifurcation structure of the csa-lattice to a high degree and in order to reduce material hysteresis effects. In the first experiment (blue in Figure 3.10) the primary state was unloaded; in the second (red), unloading of the secondary state was investigated. The data sets presented in Figure 3.10 should be read from right to left as at the beginning of each test the applied strain was $\epsilon = 0.06$ mm/mm and at the end of the test $\epsilon = 0.00$ mm/mm.

Unloading of the primary state showed the same behaviour found in the loading experiments: relaxing the experimental sample caused a smooth transition from the switched to the homogenous cellular geometry, the reverse of the behaviour described in Section 3.2. In contrast to this, the secondary state became unstable during the unloading experiment and the geometry switched to that of the primary state.

The two data sets shown in Figure 3.10 have the common features of the perturbed pitchfork bifurcation diagram [4, 31] which was introduced in Chapter 1.5. The continuous branch is represented by the data taken during the primary state unloading experiment and the blue data set is the stable branch of the disconnected saddle node. The γ^* values measured during the unloading secondary state experiment dropped dramatically at $\epsilon = 0.021$ mm/mm. At this strain value only one equilbrium state of the structure existed and this was the primary state. Because of this, the ellipses in the switched geometry of the secondary state flipped their orientations by 90^o about their respective centres. Further unloading of the csa-lattice led to the transition back to the homogeneous cellular geometry as described for the primary state. The switch from the secondary to the primary switched geometries occurred ≈ 0.003 mm/mm prior to the ϵ_{cr} value determined in Section

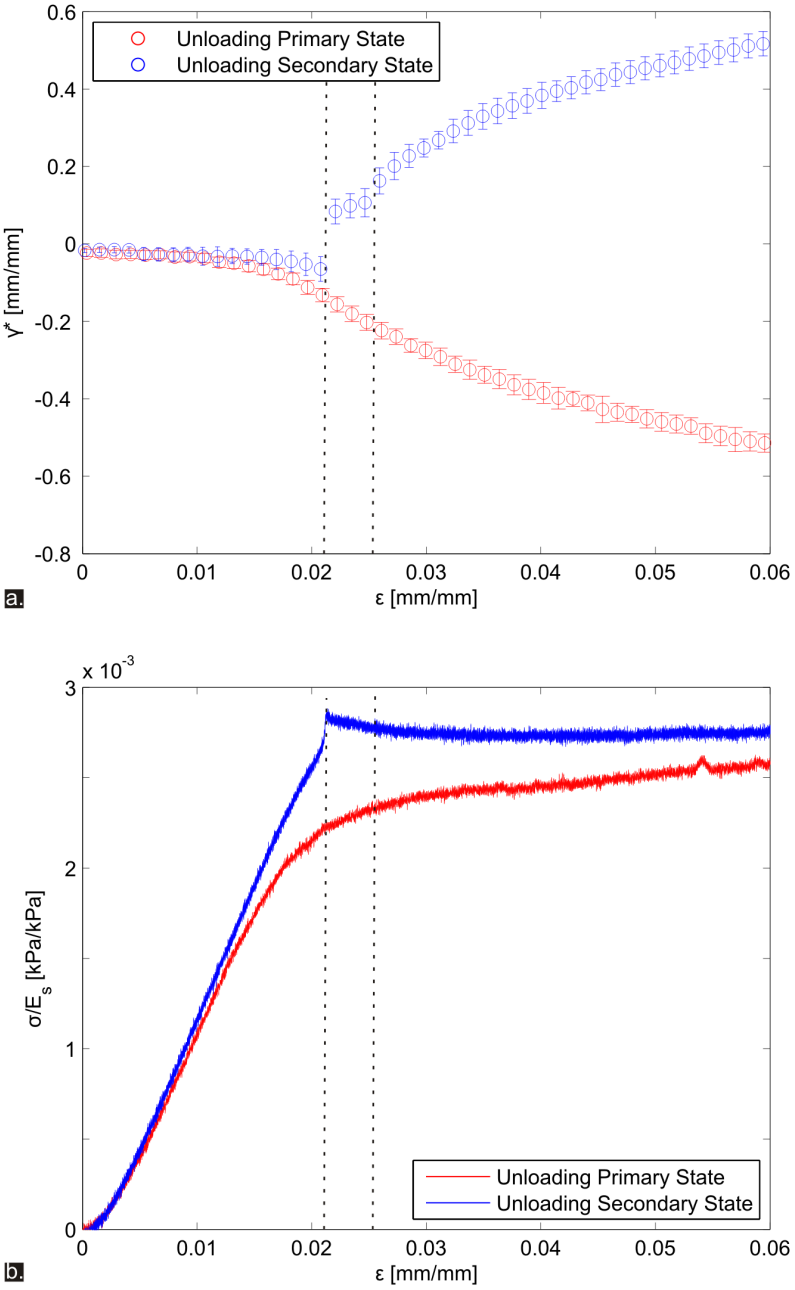

Figure 3.10: The onset of instability in the secondary state. The γ-ϵ plots (a) are similar to the perturbed pitchfork diagram with small imperfections. The states are associated with different plateau stress levels (b) and the transition between the secondary and primary state is marked by a decrease in the normalised stress.

3.2.5 which implies that the imperfection which caused the primary state to be the preferred buckling configuration observed in loading experiments was small [4,31].

The normalised stress-strain data taken during the two tests is shown in Figure 3.10 (b). The secondary state was associated with a higher normalised stress than the primary state. The difference between the two sets increased as the secondary state became unstable and this occurred over the region bound by the two dashed lines in Figure 3.10. The switch to the primary state was accompanied by a drop in $\frac{\sigma}{E_s}$ which then led rapidly into a linear strain region. The switch between the primary and secondary states was not reflected entirely by the data sets shown in Figure 3.10 - the normalised stress and aspect ratio values for the secondary data set did not overlap with those taken in the primary state unloading experiment. It appears that the switching event induced a short-term plastic effect in the structure. This caused the aspect ratio of the voids aspect ratios to be higher than in the first experiment at the same level of compression, and this is associated with a higher level of normalised stress across the surface of the sample.

3.4 Summary

The results of a series of experiments have shown the csa-lattice to be a highly coupled nonlinear system in which pattern transformation is observed at a critical degree of compression. The transition between the trivial and primary states was evident in the variation of the aspect ratio of the voids and the stress across the sample with strain respectively, and these trends were repeatable. The switch is therefore a robust phenomenon which comes about from a reversible elastic instability triggered by loading. It has also been shown that it is possible to access the perturbed secondary state which was stable for a wide unloading range. This

state was associated with a higher stress value and a direct transition back to the primary state was observed coming in close proximity to the reversion of the structure to the trivial state. In Chapter 4 the analysis is carried forward to other csa-lattice geometries to gain a deeper understanding of the pattern-switching mechanism.

Chapter 4

Variation with Void Fraction and Side Effects

The results of an experimental study of the csa-lattice geometry are presented. It is established that the normalised critical stress, critical strain and normalised elastic modulus of these structures vary with the void fraction according to simple scaling laws. These imply that the structure deforms predominantly by axial stretching of the inter-hole ligaments in the pre-buckling phase of compression. For samples with a low number of rows a delay in the onset of the pattern-switching instability was observed. This caused an increase in the normalised critical stress of the experimental samples. It is also shown that a change in the cell shape to diamonds causes a similar pattern to be induced, whilst localisation is found in square voids. Discussion of these effects was motivated by consideration of a simple spring-link model and predictions arising from this have been compared to the experimental results.

4.1 Introduction

In Chapter 3 the critical strain, normalised critical stress and normalised elastic modulus of an 8×8 csa-lattice ($\Phi = 0.65$) were measured. The focus in this chapter is on determining these quantities for a range of csa-lattice geometries. In particular, the relationship between the stability, strength and stiffness of these structures to the parameters Φ, n and m is investigated.

4.1.1 Scaling Laws

The approach adopted here follows conventional studies [3,18,54] of two-dimensional cellular structures under uniaxial compression. Accordingly, the main aim was to determine empirical fits of the form

$$\frac{\sigma_{cr}}{E_s} = \frac{\sigma_o}{E_s} \left(\Phi_{max} - \Phi\right)^{\alpha} \tag{4.1a}$$

$$\epsilon_{cr} = \epsilon_o \left(\Phi_{max} - \Phi\right)^{\beta} \tag{4.1b}$$

$$\frac{E}{E_s} = \frac{E_o}{E_s} \left(\Phi_{max} - \Phi\right)^{\gamma} \tag{4.1c}$$

In equations (4.1) Φ_{max} is the maximum void fraction of the csa-lattice. Whilst for many 2D cellular structures $\Phi_{max} = 1$, the curvature of the circular voids neccessitates that

$$\Phi_{max} = \frac{\pi}{4} \approx 0.785 \tag{4.2}$$

where Φ_{max} has been calculated using equation (3.1) and the condition that the inter-hole distance l is equal to the void diameter d.

As listed in Table 4.1, the exponents α, β and γ and the constants $\frac{\sigma_o}{E_s}$, ϵ_o and $\frac{E_o}{E_s}$ depend on the shape of the cells in regular 2D lattices [18]. The exponents are used to distinguish between stretching- and bending-dominated structures. In the former, $\alpha \approx 3$, $\beta \approx 1$ and $\gamma \approx 2$, whereas in the latter $\alpha \approx 3$, $\beta \approx 3$ and $\gamma \approx 0$. The scaling laws shown in Table 4.1 have been derived by considering the compression of the constituent struts within each lattice and are accepted as valid for $\frac{t}{l} < 0.25$ [3], where t is the uniform thickness of each strut, l its length. The scaling laws presented above are theoretical expressions which have been validated in experiments and numerical simulations [3].

The curvature of the voids in the csa-lattice makes assessment of its connectivity non-trivial and the scaling laws expressed in equations (4.1) have not yet been established for the csa-lattice. The square arrangement of cells indicates that its behaviour will be similar to that of lattices in which the voids are square in shape. Taking this comparison into consideration, it was expected that the exponents and constants for the csa-lattice empirical relationships would have similar values to those listed in the second line of Table 4.1.

The principal new aspect of this investigation is the parameter range over which the experiments have been conducted. As discussed above, the scaling laws presented in Table 4.1 are only valid for high Φ values to enable simple geometrical models of these structures to be used. As well as this, according to Gibson and Ashby [3] the definition of a porous structure as being a "cellular solid" is brought into question when $\Phi < 0.7$[1]. There are two reasons for ignoring limitations on Φ here. Firstly, the value of Φ_{max} calculated in equation (4.2) combined with Gibson & Ashby's limit defines a range of Φ values outwith the bounds of the

[1]This limit is 0.8 according to the University of Virginia [55].

Cell Shape	Z	$\frac{\sigma_{cr}}{E_s}$	ϵ_{cr}	$\frac{E_o}{E_s}$
Hexagon	3	1.50 (1 - Φ)^3	0.10	0.14 (1 - Φ)^3
Square	4	0.10 (1 - Φ)^3	0.21 (1 - Φ)^2	0.50 (1 - Φ)
Triangle	6	0.33 (1 - Φ)^3	0.27 (1 - Φ)^2	0.09 (1 - Φ)

Table 4.1: Scaling laws for 2D cellular structures. $\frac{\sigma_{cr}}{E_s}$, ϵ_{cr} and $\frac{E_o}{E_s}$ for 2D cellular structures vary according to the equations listed here The shape of the cell, and hence the connectivity Z, determines the constant and exponents in each of the relationships. The critical stress referred to here is often termed the elastic buckling stress σ_{el} in order to differentiate it from the stress associated with plastic and brittle failure.

manufacturing process as the maximum Φ value available using these methods was 0.65. Secondly, it was desired to probe the prediction by Bertoldi et al that global pattern-switching in the csa-lattice will *not* persist beyond a critical void fraction value $\Phi_B = 0.34$ [6].

4.1.2 Methodology

The void fraction study was performed on two sets of csa-lattices. The 4 $\times$ 4 csa-lattices had Φ values increasing from 0.15 to 0.65 in steps of approximately 0.025 whereas the 8 $\times$ 8 samples had void fractions in the range 0.40 to 0.65. All samples were made from Sil AD Spezial and tests were conducted at a compression speed of 0.01 mms^{-1}.

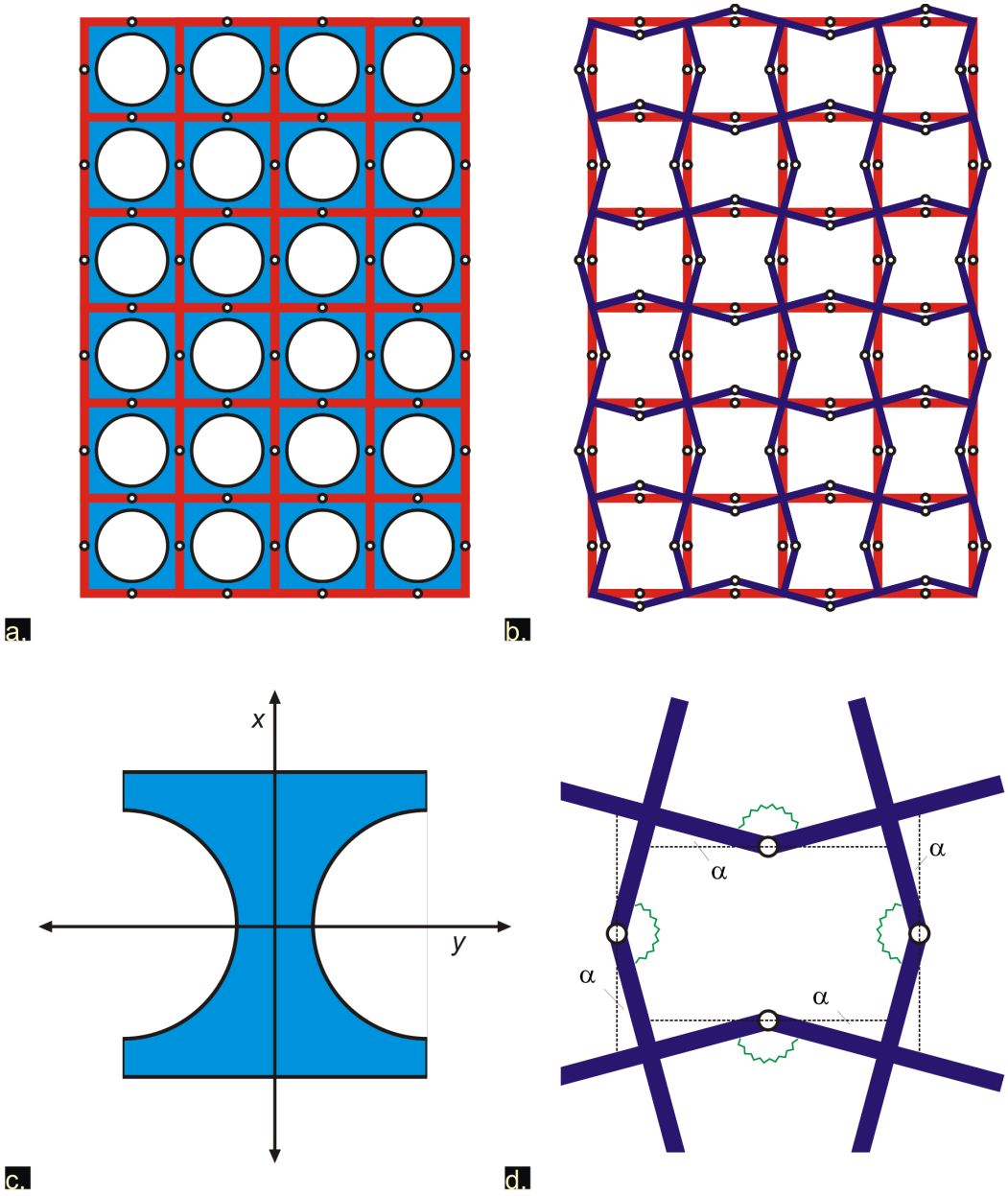

Figure 4.1: The discrete model. (a) The coupling between the hinged rigid crosses (red) in the frame means that a period-doubling pattern switch occurs when the trivial state becomes unstable (b). By considering the Euler buckling of a single tapered rod (c), it was possible to determine the rotation stiffness ρ of the rotational springs (green) which are positioned at each hinge (d).

4.2 Discrete Model

4.2.1 Model Description

The results of the experiments are compared with predictions made using the spring-link model [56]. The model is illustrated in Figure 4.1. It comprises a skeletal frame of the csa-lattice which is made up of a series of rigid crosses (Figure 4.1 (a)) inter-linked by sprung hinges. The crosses have similar properties to the interstitial connectors in the csa-lattice and they behave as rotating rigid units. The crosses have height and breadth l which is equal to the inter-hole spacing of the voids in the csa-lattice and they are arranged such that they form a square lattice of $n \times m$ square cells.

In addition to this, where two crosses meet there is a hinge and this is positioned at the thinnest section of each of the horizontal (vertical) ligaments in the csa-lattice. The result of the coupling and hinging of the rods is that when one cross is deflected from its initial position by an angle α, the other crosses must also move. The net effect is that the initially square cells transform in a period-doubling pattern switch in both directions as shown in Figure 4.1 (b). The switch in geometry is qualitatively similar to that observed in the experiments.

The model presented here represents a first step in modelling the pattern-switching properties of the csa-lattice. It has been tailored such to accommodate only the period-doubled mode of the lattice as opposed to other modes such as the longer wave, global modes described in Chapter 1. Here, it is acknowledged that other modes may prevail in the csa-lattice, particularly for structures with low void fractions and large row numbers. In these limit it is foreseeable that the structure will behave as a simple elastica (i.e., the voids become so small that their

influence on the elastic matrix is reduced to nothing). In this limit, the structure may assume a half-wave mode like that described in Chapter 1 and there is no allowance, as yet, for this in the model.

The motivation behind the construction of this model is to provide a simple alternative to the Bloch wave analysis for determining the critical stress of the csa-lattice. Whilst the aforementioned numerical approach provides a comprehensive method for exploring the various instability modes of the structure, it is time-consuming and requires a knowledge and expertise of finite element simulations to correctly implement [22, 26]. The advantage, therefore, of the discrete model presented here is the relative simplicity of the mathematics associated with it. By comparing the model to experimental data, the goal is to determine how appropriate it is to apply simple beam theory to predict the buckling loads of these structures, as well as the effect of the boundaries on this property.

4.2.2 Spring Constants

The resistance to deformation in the model is provided by rotational springs (stiffness ρ [Nmrad^{-1}]) positioned at each of the hinges. In general ρ can be calculated separately for horizontal (ρ_h) and vertical springs (ρ_v). However, this is only necessary where the holes are elliptical and/or arranged on a rectangular lattice. The spring stiffness is calculated by considering the elastic buckling of a tapered column (Figure 4.1 (c)) when it is subjected to an axial force F. A comprehensive derivation of the spring constants is presented in Appendix C and only the pertinent points are highlighted here. The stiffness ρ is calculated according to the following equation [56]

$$\rho = 12wE_s \left(\int_{\frac{-l}{2}}^{\frac{l}{2}} \frac{1}{(2y(x))^3} dx \right)^{-1} \tag{4.3}$$

where w is the out-of-plane and $2y(x)$ the in-plane width of the tapered column. $y(x)$ varies with the distance x along the central axis of the rod as

$$y(x) = \begin{cases} \frac{l}{2} - \frac{d}{2}\sqrt{1-4x^2} & \text{if } 0 < |x| < \frac{d}{2} \\ \frac{l}{2} & \text{if } \frac{d}{2} < |x| < \frac{l}{2} \end{cases}$$

In Figure 4.2 the variation of ρ is shown as a function of the void fraction (red). As the voids become smaller, the amount of material, and hence the stiffness, increases.

4.2.3 Boundary Conditions

The total strength of the model is calculated by adding together the contributions of the rotational springs in each of the rows and columns. In order to reflect the fixed boundary conditions used in the experiment, the stiffness of the vertical springs in the upper- and lower-most rows of the model are increased by a rotation stiffness factor $\frac{1}{k}$, where $k \leq 1.0$. This is qualitatively similar to the concept of effective length kL in the Euler-Bernoulli column problem, whereby k assumes different values depending on the boundary conditions ($k = 0.5$ where both ends are clamped, for example, meaning that its length L is effectively reduced). It is assumed that each of the crosses in the interior of the sample is free to translate and rotate with no influence from the boundaries, meaning that $k = 1.0$ for the majority of the rods in the discrete model.

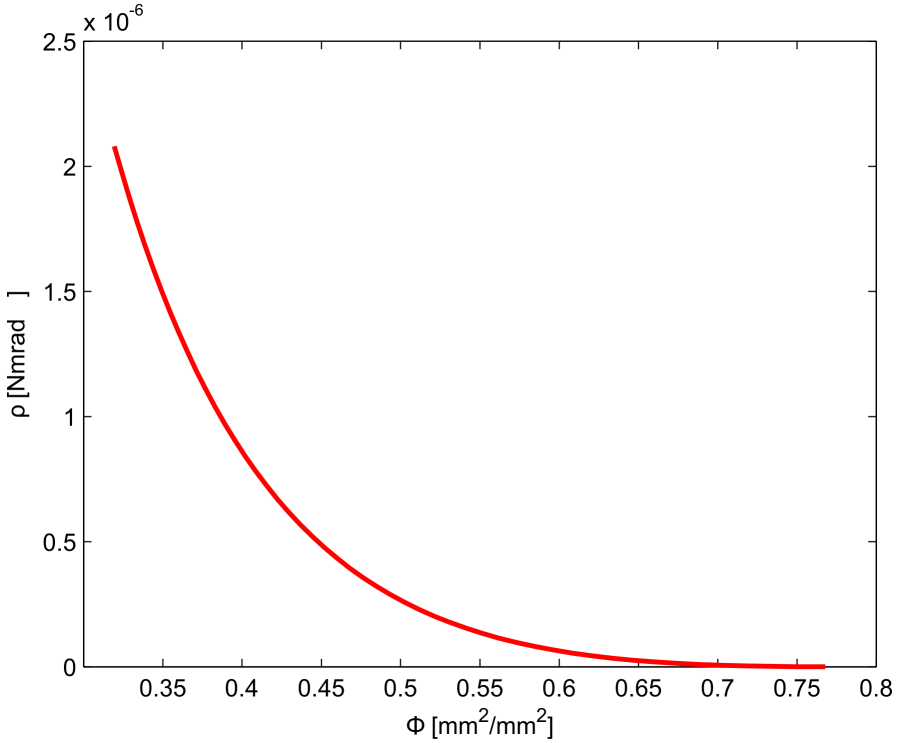

Figure 4.2: The variation of ρ with Φ. The rotational spring stiffness calculated using the model decreases with increased void fraction.

4.2.4 Critical Stress

The normalised critical stress can be calculated by considering the total energy function of the structure, $\Pi(\alpha)$. The full details of the derivation can be found in Appendix C. In outline, the total energy of the system is given by

$$\Pi(\alpha) = Flmn\cos\alpha + 2m(2n-2)\rho\alpha^2 + \frac{4m\rho\alpha^2}{k} \tag{4.4}$$

where the first term represents the work done by an external force F in compressing the structure. The remaining two terms are the energy stored in the rotational springs. Linear stability analysis of equation (4.4) allows the calculation of a critical force F_{cr} at which the trivial state ($\alpha = 0$) becomes unstable. F_{cr} is given by

$$F_{cr} = \frac{8(1-\frac{1}{n})\rho}{l} + \frac{8\rho}{nkl} \tag{4.5}$$

The critical stress $\frac{\sigma_{cr}}{E_s}$ can be calculated by dividing equation (4.5) by the area over which it acts ($A = wl$). As ρ is linear in w and E_s (equation (4.3)), these two variables can be set to unity, yielding

$$\frac{\sigma_{cr}}{E_s} = \frac{8\rho}{l^2}\left(1 + \frac{1}{kn} - \frac{1}{n}\right) \tag{4.6}$$

as the predicted normalised critical stress of the cellular structure. It is noteworthy that there are terms in equation (4.6) which depend on the number of cells which make up the lattice. Specifically, there is an inversely proportional relationship with n, which suggests that the smaller the number of rows, the greater the stress at which the pattern onset will occur. This implies that the effect should be

detectable in the experiments since the samples are small (i. e. less than 10 rows).

4.3 Experimental and Numerical Results

The strength, stability and stiffness curves for the csa-lattice are presented in the following sections and a short description of some key experimental observations is given in Section 4.3.1.

4.3.1 $\gamma - \epsilon$ and $\sigma - \epsilon$ Plots

The data shown in Figure 4.3 represents the general trends observed in the experiments. The variation of $\frac{\sigma}{E_s}$ (Figure 4.3 (a)) and γ (Figure 4.3 (b)) with ϵ has been plotted for four 4×4 csa-lattices with different void fractions. Both the aspect ratio- and normalised stress-strain measurements show the same qualitative behaviour described in Chapter 3 and this allowed the critical strain ϵ_{cr}, normalised critical stress $\frac{\sigma_{cr}}{E_s}$ and the normalised elastic modulus $\frac{E}{E_s}$ to be measured. The dashed vertical lines in each of the plots represent the average ϵ_{cr} value for that particular structure, which was calculated over five successive tests. A comparison of the data sets presented in Figure 4.3 is in accord with intuition in that samples with smaller Φ were stiffer, stronger structures which buckled at a higher degree of compression. The same trends were observed for the 8×8 experimental data sets.

4.3.2 Strength

In Figure 4.4 the variation with Φ of the critical stress for the 4×4 (blue circles) and 8×8 (red circles) csa-lattices has been plotted. The dashed curve in each of the graphs in Figure 4.4 represents the best fit of equation (4.1a) to the data. For the 4×4 samples, $\frac{\sigma_o}{E_s} = 0.71 \pm 0.15$ and $\alpha = 2.60 \pm 0.17$. The 8×8 data set

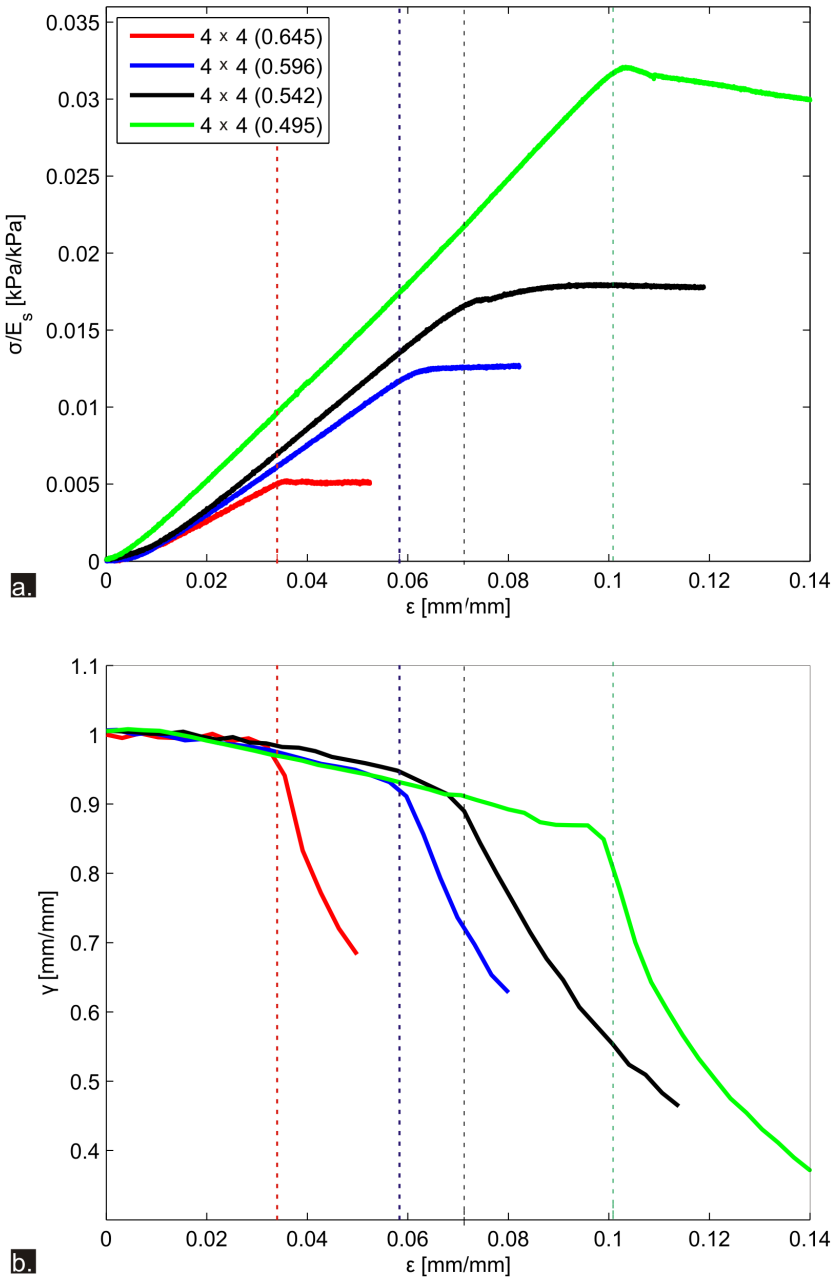

Figure 4.3: Example plots to show the trends of the experiments. The stress (a) - and aspect ratio (b) - strain plots show the same qualitative behaviour as described in Chapter 3 and the dashed lines are the critical strain.

shows behaviour approximated by $\frac{\sigma_o}{E_s} = 1.00 \pm 0.10$ and $\alpha = 2.94 \pm 0.09$. The size of the structure influences the stress at which the pattern onset occurs: the critical stress values presented in Figure 4.3 (a) are greater than those in Figure 4.3 (b). The dashed black line in Figure 4.4 marks $(\Phi_{max} - \Phi_B) = 0.445$ which is the theoretical limit for pattern-switching predicted by Bertoldi et al [6]. In the experiments, no pattern-switching was observed for Φ values less than Φ_B.

In both graphs shown in Figure 4.3, the green curve represents the variation of $\frac{\sigma_{cr}}{E_s}$ calculated using the discrete model with $k = 0.70$, which is the stiffness factor used when calculating the buckling stress of Euler-Bernoulli columns with one fixed and one free boundary. The normalised critical stress calculated using the model is less than the experimental measurements and this implies that the stiffness of the springs has been underestimated. For the data shown in Figure 4.4 the deviation of the critical stress calculated using the model is between 25% and 50% lower than the experimental values. In Figure 4.4 the deviation is approximately 20 %, which suggests that there is a slight improvement in the agreement between theory and experiment as the sample size was increased. The black lines in Figure 4.3 represent the best fit of equation (4.6) to the experimental data, where for the 4 $\times$ 4 lattices $k = 0.31$ and for the 8 $\times$ 8 lattices $k = 0.21$.

4.3.3 Stability

The dependence of the critical strain ϵ_{cr} on Φ is shown in Figure 4.5 for the two csa-lattice sizes. Again, the experimental data is represented by circles and the dashed lines show the best fit of equation (4.1b.) to the data. As with the $\frac{\sigma_{cr}}{E_s}$ values, there is a noticable decrease in ϵ_{cr} when the size of the lattice is increased. This is reflected in the contrasting ϵ_o and γ values for the two data sets: for the 4 $\times$ 4 csa-lattice, $\epsilon_o = 0.82 \pm 0.07$ and $\beta = 1.66 \pm 0.07$, whereas for the 8 $\times$ 8

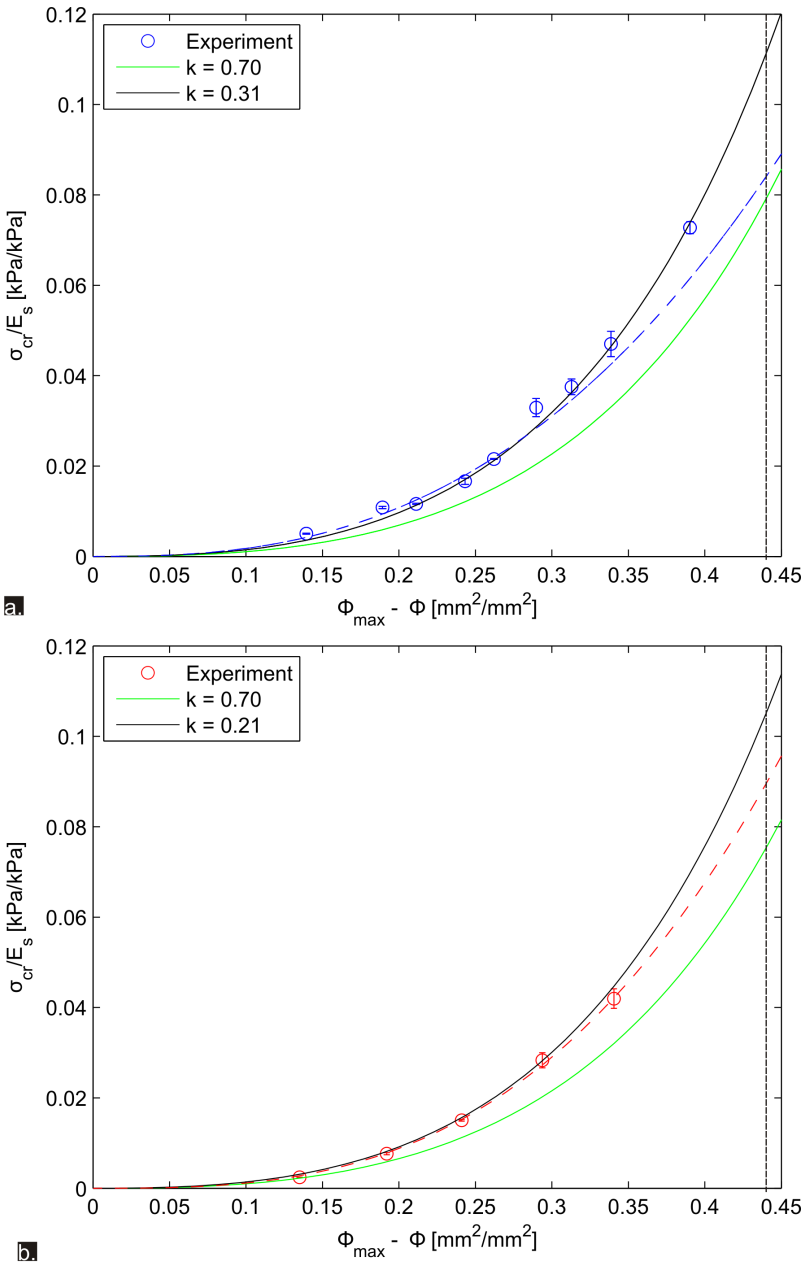

Figure 4.4: The variation of the normalised critical stress $\frac{\sigma_{cr}}{E_s}$ with Φ. This has been plotted for (a) the 4×4 and (b) the 8×8 experimental samples. The experimental data has been plotted alongside the predictions from the model using k =0.70 (green) and $k = 0.31$ (a) and $k = 0.21$ (b), which are represented by the black lines in each plot. The dashed line is the empirical fit for each data set.

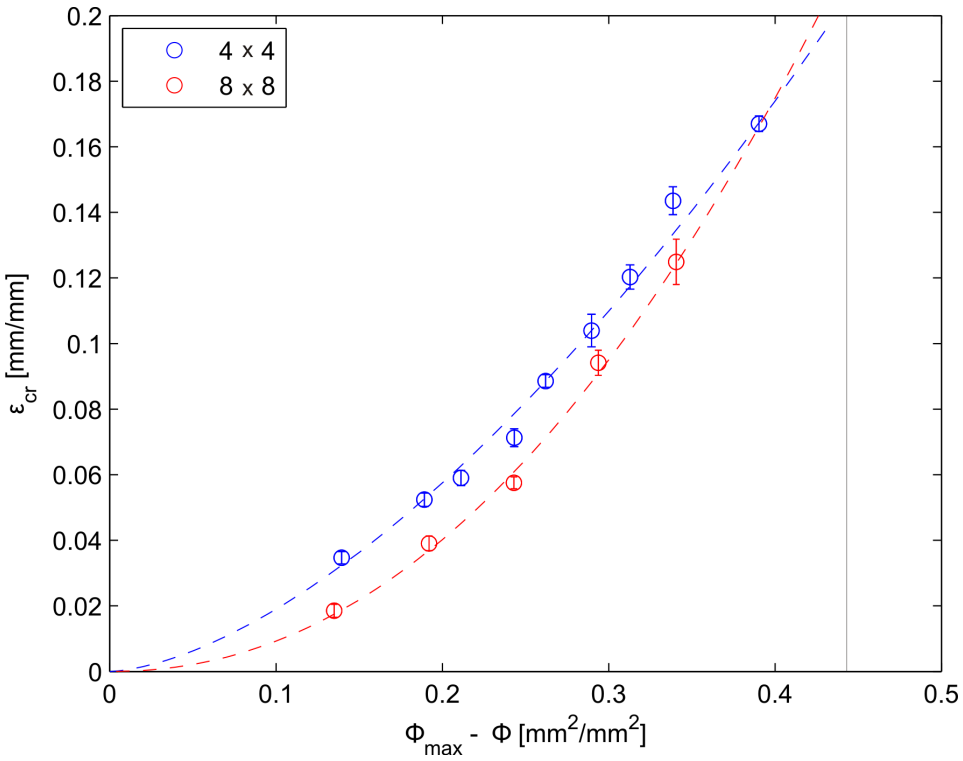

Figure 4.5: The variation of the critical strain ϵ_{cr} with Φ. This has been plotted for the 4×4 (blue) and 8×8 (red) csa-lattice. The dashed line is the empirical fit for each data set.

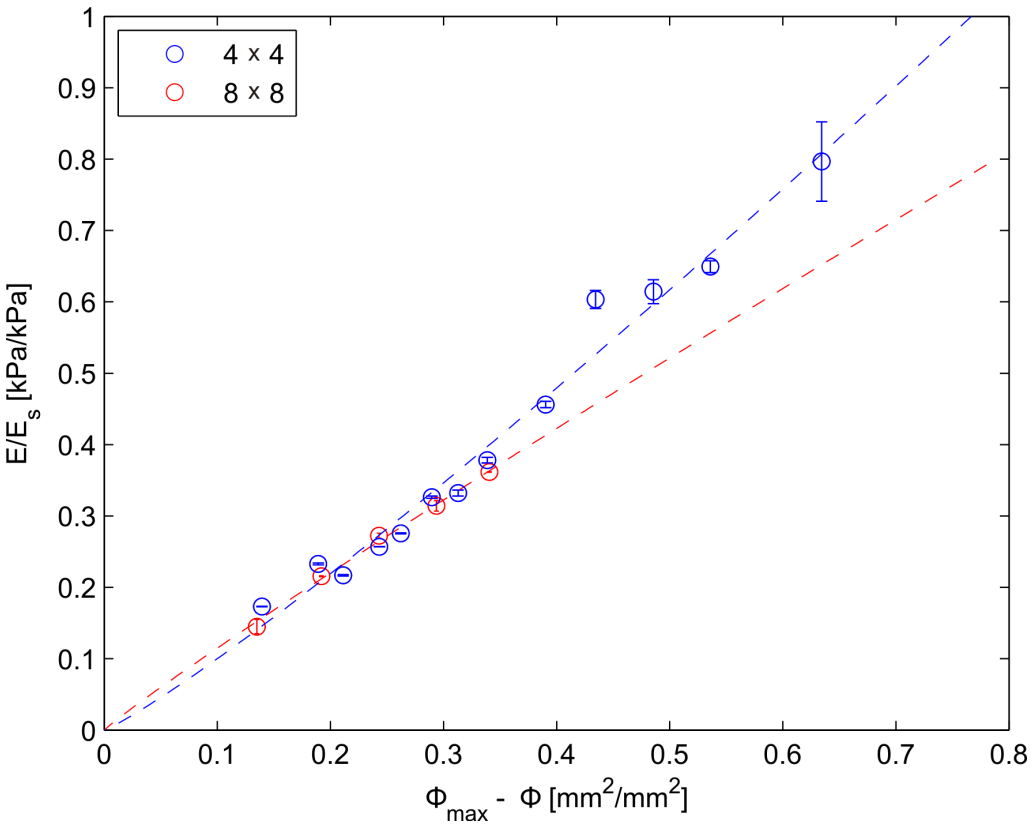

Figure 4.6: The variation of the normalised stiffness with Φ. For both the 4×4 (blue) and 8×8 (red) samples a linear form of equation (4.1c) provided a good fit to the experimental data.

csa-lattice $\epsilon_o = 1.22 \pm 0.07$ and $\beta = 2.12 \pm 0.10$. Again, no data points have been plotted past the limit $(\Phi_{max} - \Phi) = 0.445$, as pattern formation was not observed here.

4.3.4 Stiffness

The change in the normalised elastic modulus of the csa-lattice with Φ is illustrated in Figure 4.6. Here the variation of the normalised honeycomb stiffness with the void fraction has been plotted. For both the 4×4 and 8×8 lattices a quasi-linear

dependence of $\frac{E}{E_s}$ with $(\Phi_{max} - \Phi)$ was observed. Fitting equation (4.1c) to the experimental data yielded $\frac{E_o}{E_s} = 1.35 \pm 0.07$ and $\gamma = 1.13 \pm 0.06$ for the 4×4 and $\frac{E_o}{E_s} = 1.00 \pm 0.06$ and $\gamma = 0.94 \pm 0.04$ for the 8×8 csa-lattices.

As highlighted in the previous sections, no pattern switch was observed for csa-lattices with $\Phi < 0.40$ and as a result no ϵ_{cr} or $\frac{\sigma_{cr}}{E_s}$ measurements were presented for these. Although instability onset was observed to only exist for high values of Φ, it was possible to measure the honeycomb stiffness of these samples, which is why the range of Figure 4.6 is larger than that of Figures 4.4 and 4.5 respectively. For low Φ values the consequence of compression was these structures *out of plane* at high ϵ values and when this occurred the experiment was brought to an end.

4.4 Size Effects

The results shown in Section 4.3 demonstrated a dependence on the finite sample size. As was predicted by the model, the smaller n, the greater the normalised stress at which the csa-lattice buckled. The influence of sample size (i.e. the role played by n and m) on the strength, stability and stiffness of the csa-lattice was investigated in the study which follows.

4.4.1 Methodology

Three batches of experimental samples with void fractions $\Phi = 0.65$, 0.60 and 0.55 respectively were manufactured and then subjected to compression tests. Each batch comprised eight samples with $m = 8$, and increasing n from 3 to 10. After compression tests on these were complete, the samples were rotated by 90^o about their centres and the tests were repeated. In the initial phase of the experiments it was therefore possible to investigate the effect of increased height of samples

with fixed width, and vice versa in the latter phase. All experimental samples were made from Sil AD Spezial and tests were conducted at a compression speed of 0.01 mms^{-1}.

4.4.2 Results

The effect of sample size on the elastic properties of the csa-lattice can be seen in Figure 4.7. The data presented in the plots in Figure 4.7 (a - c) is used to show the effect of n; the role played by m has been plotted in the graphs in Figure 4.7 (d - f). In all panels the different Φ values are represented according to the following colour scheme: 0.65 (red), 0.60 (blue) and 0.55 (green).

As can be seen in the plots (a) and (b) in Figure 4.7, n plays a key role in determining the value of the critical point at which pattern onset occurs. The shorter the structure, the greater the degree of compression required for the onset of instability and the associated normalised stress increases. There is a clear inverse proportional relationship with n displayed in Figure 4.7, whereas the stiffness of the structure is unaffected (Figure 4.7 (c)). The bold line plotted for each of the data sets is the function

$$\frac{\sigma_{cr}}{E_s} = \frac{8\rho}{l^2} + \frac{A_o}{n} + B_o \tag{4.7}$$

where ρ is the spring stiffness calculated using equation (4.3). Equation (4.7) is a modified version of equation (4.6) which incorporates the term $\frac{8\rho}{l^2}$ as well as an inverse dependence on n. The constants A_o and B_o have been found to depend on the void fraction as displayed in Table 4.2. Whilst A_o increases with decreased Φ, B_o is small ($\frac{|B_o|}{A_o} \approx 10^{-2}$) and so its influence is negligible.

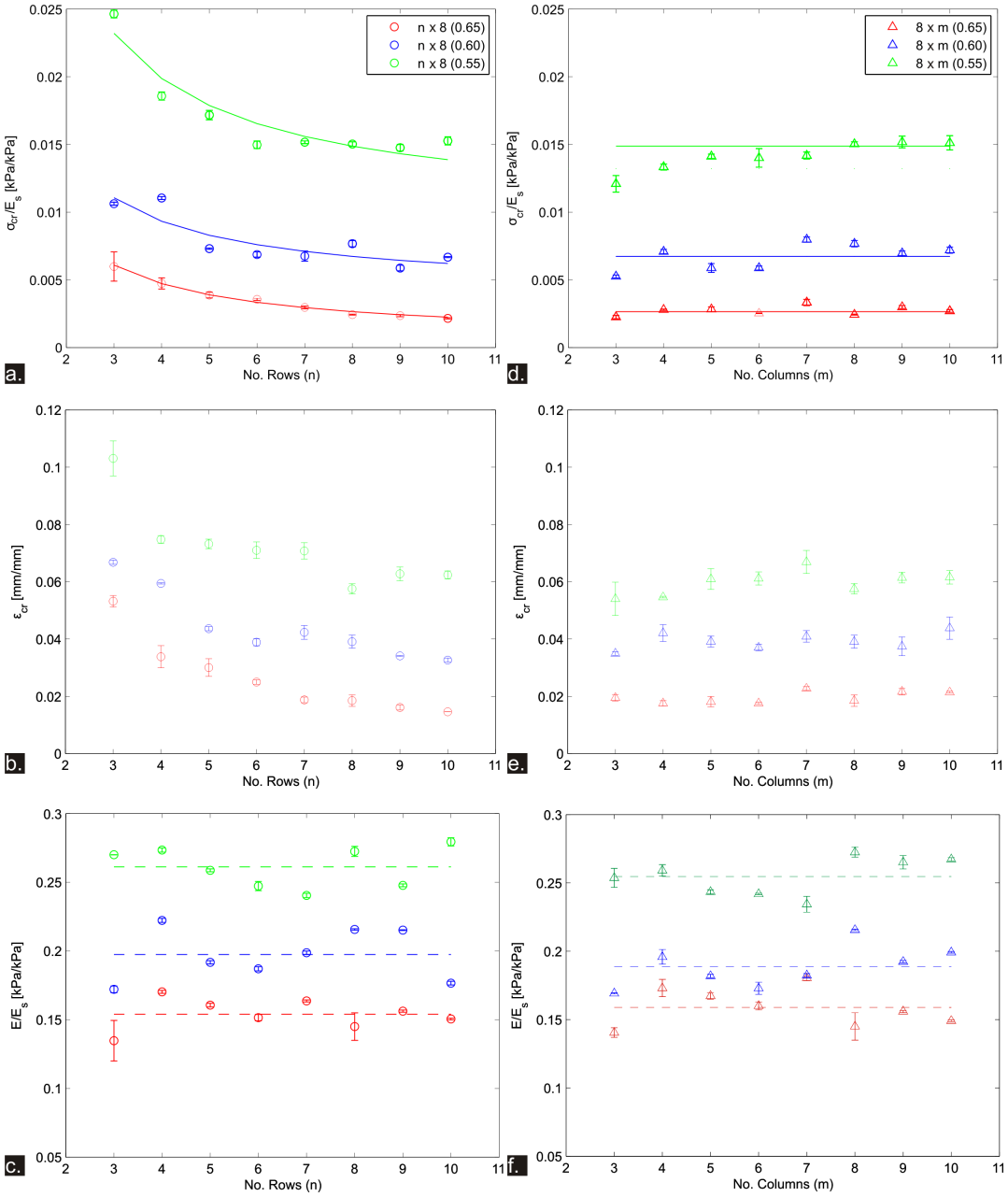

Figure 4.7: Size effects in csa-lattices. The variation of $\frac{\sigma_{cr}}{E_s}$, ϵ_{cr} and $\frac{E}{E_s}$ with n (a - c) and m (d - f) has been plotted.

Φ	A_o	B_o
0.65	0.0165 ± 0.007	-0.0015 ± 0.0002
0.60	0.0208 ± 0.046	-0.0009 ± 0.0010
0.55	0.0400 ± 0.050	-0.0001 ± 0.0010

Table 4.2: The parameters A_o and B_o for the three Φ values considered in the study of size effects. These were calculated by fitting the experimental data to equation (4.7).

Whilst the numbers of rows in the sample appear to influence two of the three measurements plotted here (the normalised elastic modulus data presented in Figure 4.7 (c) is independent of n), m does not play such a role. By fixing n to 8 and increasing m there was no change in the parameters plotted in the graphs (d - f) in Figure 4.7. As such the strength, stability and stiffness of the structure is independent of the finite width of the sample as predicted by the discrete model.

4.5 Void Shape

The effect of cell shape was also investigated using 2D cellular structures with *square* and *diamond*-shaped voids. These were made using the techniques described in Appendix B. According to the naming convention described in Chapter 3 the structures are called *ssa*- and *dsa*-lattices, where the first initials stand for the cell shape (square or diagonal respectively) and again *sa* stands for *square array*. The geometry of the ssa- and dsa-lattices is illustrated in Figure 4.8. Little experimental research exists on the mechanics of dsa-lattices although theoretical models using tesselated hinged squares have been shown in theory to exhibit ideal auxetic behaviour (i.e. Poisson's ratio ν = -1) when they are compressed [48, 49]. The pattern which develops in the models is qualitatively similar to the elliptical

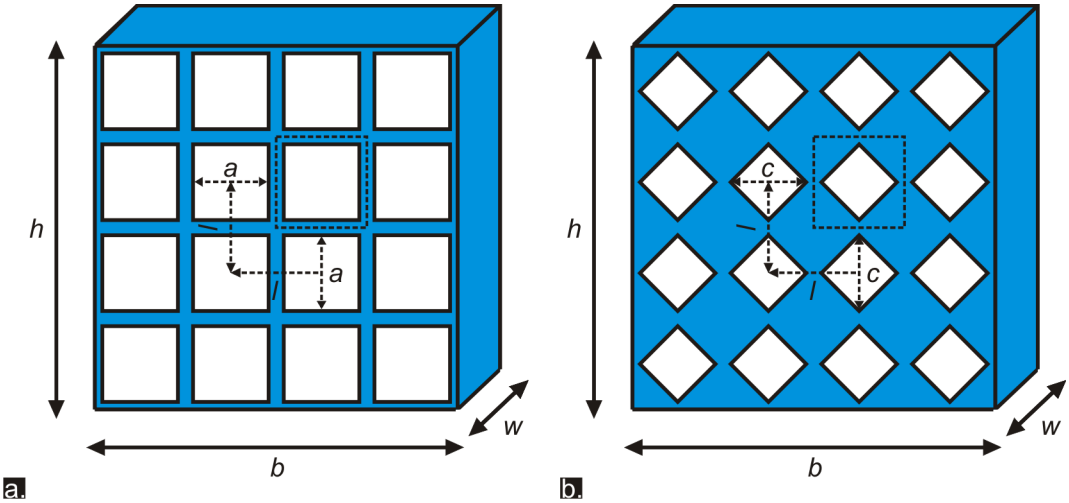

Figure 4.8: The ssa- and dsa-lattice geometries. These consisted of square arrays of square (a) and diamond (b) cells respectively.

pattern observed in the csa-lattice. Instead of ellipses, the diamond shaped voids form rhombi which are oriented orthogonally to their neighbours.

4.5.1 Geometry

The ssa- and dsa-lattice geometries comprise an $n \times m$ array of cells and the inter-hole spacing is l. The cells in the former are square-shaped with side a. The void fraction Φ of these structures is calculated as

$$\Phi = \left(\frac{a}{l}\right)^2 \tag{4.8}$$

For the dsa-lattice, in which the voids have diagonal c,

$$\Phi = \left(\frac{c}{\sqrt{2}l}\right)^2 \tag{4.9}$$

4.5.2 Methodology

An ssa- and a dsa-lattice were manufactured as described in Appendix B such that each was a 4 × 4 square array with $\Phi = 0.45$. The lattices were made from Sil AD Spezial and tested using the aluminium loader at a compression speed of 0.01 mms^{-1}.

4.5.3 Elastic Buckling

Both the ssa- and dsa-lattices underwent elastic buckling when compressed uniaxially. However, the form taken by each of the structures in their respective buckled states was qualitatively different. The ssa- and dsa-lattices are shown in the strain states $\epsilon = 0.03$ mm/mm and 0.10 mm/mm in the images in Figure 4.9. At lower ϵ values the geometry of the cells in the ssa- and dsa-lattice is homogeneous (Figure 4.9 (a) and (b) respectively). Both structures buckled at a critical strain and there is a clear difference between the response of the two lattice types as shown in Figure 4.9 (c) and (d) respectively. The ssa-lattice buckles to the side such that there is localised shearing of the voids in the top and bottom rows of the structure. However, in the dsa-lattice the effect of compression is to create a new cellular pattern. In this, the diamonds have transformed into an array of mutually orthogonal rhombi and these are equivalent to the elliptical voids which form in the csa-lattice. Again, the pattern is global and no localised effects were observed.

The comparison between the buckling states of the dsa- and ssa-lattices can be used to illustrate the competition between global and local buckling modes as discussed in Chapter 1. As can be seen in (c), the diamond voids change shape according to a period-doubling transformation, whilst the ssa-lattice forms a half-wave when it buckles. Similar phenomena was described by Rosen [57] in predicting the microbuckling of elastic fibers. According to Rosen, two buckling modes exist

for such composites [58], the first being an "extension" buckling mode, in which each fibre buckles into a pinned wave-shape which is 180 degrees out of phase with those directly adjacent to it, and the second being a "shear" mode in which the fibres form in-phase waves with one another. The comparisons between these and the buckled states observed for the ssa- and dsa-lattices are apparent on looking at the images in Figure. According to Rosen's work [57–59], the competition between different modes in complex systems and the dominance of one over the other depends on the relationship between axial and shear stiffnesses. When viewed in this respect, it seems that the short wavelength mode observed in the dsa- and csa-lattices results from a high shear stiffness relative to the axial stiffness, whereas in the ssa-lattice the opposite is true.

4.5.4 Comparing Cell Shapes

The normalised stress-strain curves plotted in Figure 4.10 (a) provide a quantitative comparison of the ssa- (blue) and dsa- (red) lattices to uniaxial compression. The green data sets were taken in a test on a csa-lattice with the same n, m and Φ values as the dsa- and ssa-lattices, which allows assessment of the influence of cell shape on the stress-strain characteristics of the square arrays of cells. The data sets for each structure comprise Hookean and plateau phases as described in Chapter 3. The dsa-lattice is the most compliant of the three which can be seen by comparing its slight slope to that of the other two structures. During the linear phase, the normalised stress-strain curves of the csa- and ssa-lattice samples are nearly coincident, although the former structure buckles at a higher degree of compression than the latter.

As the pattern switches in the csa- and dsa-lattices are qualitatively similar

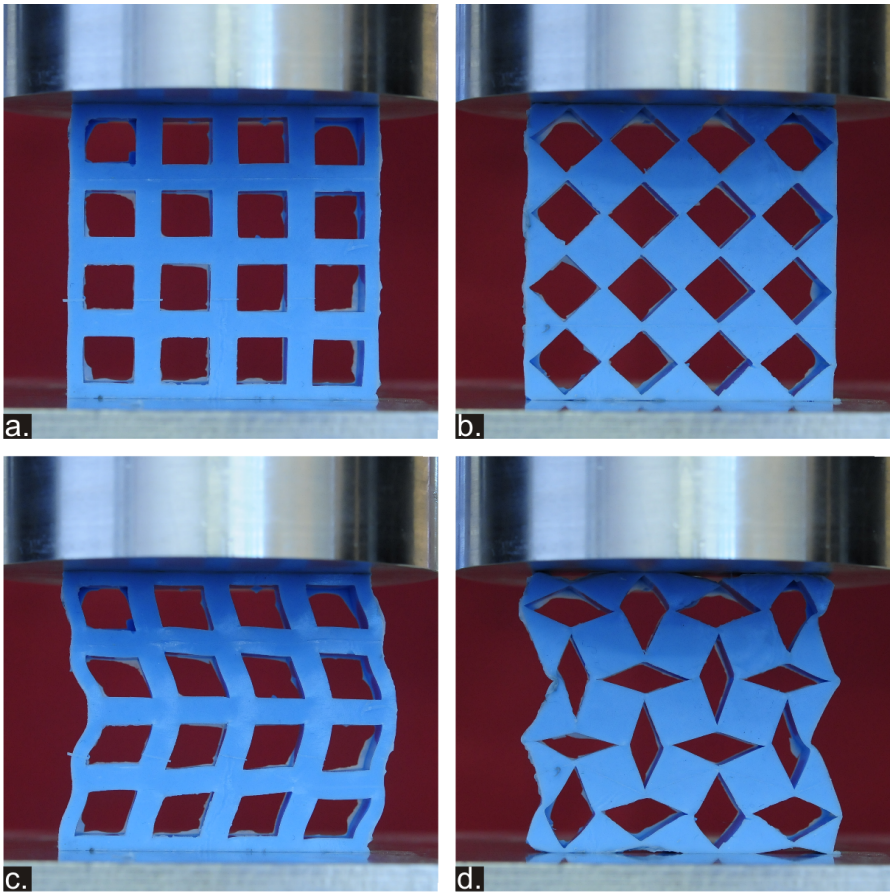

Figure 4.9: The buckled configuration of the ssa- and dsa-lattices. The samples are shown at $\epsilon = 0.00$ mm/mm (a and c) and 0.10 mm/mm (b and d) respectively.

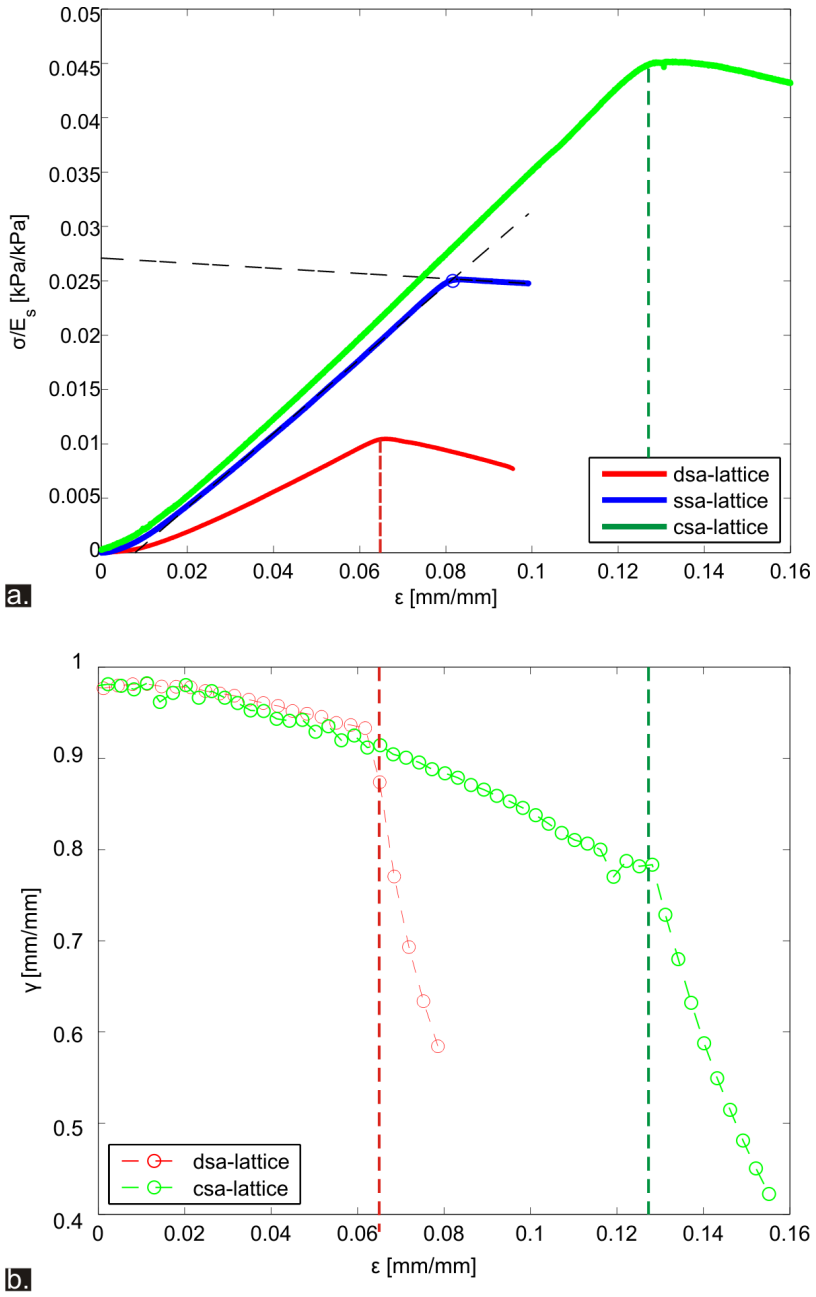

Figure 4.10: The variation of $\frac{\sigma}{E_s}$ (a) and γ (b) for the dsa-(red), ssa-(blue) and csa-(green) lattices. The critical strains for the lattices of diamond and circular cells are marked by the dashed lines. The critical point of the ssa-lattice is marked by the circle in (a).

Cell Shape	Square	Diamond	Circle
ϵ_{cr}	0.079 ± 0.002	0.066 ± 0.002	0.144 ± 0.004
$\frac{\sigma_{cr}}{E_s}$	0.025 ± 0.005	0.011 ± 0.001	0.047 ± 0.003
$\frac{E_o}{E_s}$	0.341 ± 0.022	0.203 ± 0.007	0.380 ± 0.008

Table 4.3: The critical strain, normalised critical stress and normalised stiffness of the ssa-, dsa- and csa-lattice with $n = m = 4$ and $\Phi = 0.45$.

it was possible to use the image analysis techniques described in Chapter 3 to monitor the aspect ratio γ of the diamond shaped cells. For the dsa-lattice γ was the ratio of the diagonals of each of the cells. The variation of γ with ϵ has been plotted in Figure 4.10 (b) for the csa- and dsa-lattices respectively. The plots are of the same form, comprising an initial linear decrease in the aspect ratio which changes to a square root dependence beyond a critical strain value ϵ_{cr}. The critical point of each lattice was determined by fitting equation (3.5) to the γ-ϵ data as described in Chapter 3 and these values has been marked using the dashed lines on Figure 4.10 (b). It was very difficult to determine the critical strain using image analysis techniques on the ssa-lattice as the buckled pattern was not global. However, the coordinates of the critical point were estimated by fitting linear curves to the data in the Hookean and plateau regions respectively to estimate the onset of the buckling.

The ϵ_{cr}, $\frac{\sigma_{cr}}{E_s}$ and $\frac{E}{E_s}$ measures for each of the samples have been presented in Table 4.3. Each value in the table is the mean of five compression tests and the error is the standard deviation. It is striking that for the same Φ value the csa-lattice can be considered relatively strong in comparison to the other structures; it has the highest ϵ_{cr}, $\frac{\sigma_{cr}}{E_s}$ and $\frac{E}{E_s}$ values of the three samples considered here. The dsa-lattice is far weaker and buckles at a far lower degree of compression,

	4×4	8×8
$\frac{\sigma_{cr}}{E_s}$	$0.71 \pm 0.15\ (\Phi_{max} - \Phi)^{2.60 \pm 0.17}$	$1.00 \pm 0.10\ (\Phi_{max} - \Phi)^{2.94 \pm 0.09}$
$\frac{E_o}{E_s}$	$1.35 \pm 0.07\ (\Phi_{max} - \Phi)^{1.13 \pm 0.06}$	$1.00 \pm 0.06\ (\Phi_{max} - \Phi)^{0.94 \pm 0.04}$
ϵ_{cr}	$0.82 \pm 0.07\ (\Phi_{max} - \Phi)^{1.66 \pm 0.07}$	$1.22 \pm 0.07\ (\Phi_{max} - \Phi)^{2.12 \pm 0.06}$

Table 4.4: The empirical laws for the csa-lattice. The data shows that size effects are significant when compressing small structures.

approximately half of that of the csa-lattice.

4.6 Summary

It has been shown that Φ plays a crucial role in determining the strength, stability and stiffness of the csa-lattice. The empirical fits which approximate the behaviour observed in the experiments have been reproduced for the 4×4 and 8×8 experimental samples in Table 4.4. There is a similarity in these scaling laws to those for the square cell structure which implies the csa-lattice is a stretching-dominated structure. The constants $\frac{\sigma_o}{E_s}$, $\frac{E_o}{E_s}$ and ϵ_o are higher than those presented in Table 4.1, however there is good agreement in the exponents. It should be noted that because $\Phi_{max} \neq 1$ for the csa-lattices, the empirical laws determined here cannot be considered exact equivalents to those listed in Table 4.1. This is evident when considering the asymptotic limit $\Phi = 0$; $\frac{E_o}{E_s}$ is not unity as should be expected. What the relationships do provide, however, is a means for predicting the critical points of csa-lattice samples possessing finite dimensions.

Whilst the void fraction has been the main focus of the study, the finite size of the csa-lattice - specifically, the number of rows in the sample - has been shown to influence experimental measurements. Discussion of this effect was motivated

by the predictions arising from a discrete model which has been shown to be a good approximation of the structure. It remains, however, to determine the exact effect of the boundaries on the critical stress in this model. The results presented in Section 4.4.2 imply that the coefficient of terms proportional to $\frac{1}{n}$ is dependent on Φ and not a constant as was assumed in the model. It may also be the case that the pinning at the boundary permeates through the rest of the structure. As such, a nodal stiffness for the csa-lattice must be determined to fully capture this effect.

The role of the boundaries is particularly interesting as it has a similar effect on the stability of the structure. The increased stress values associated with csa-lattice possessing low row numbers is driven by a delay in the pattern onset and not by increased stiffness of the structure, as shown in Figure 4.7. Further evidence of this effect can be found in Figures 4.5 and 4.6 respectively. The ϵ_{cr} values for the 4×4 samples are clearly higher than those of the 8×8 samples, whereas there is little to differentiate between the $\frac{E}{E_s}$ data sets. It is therefore no surprise that there is some discrepancy between the empirical fits presented for the two different sizes in Table 4.4 and noteworthy that α, β and γ tend towards 3, 1 and 2 respectively as the size of the lattice is increased.

The findings presented in Section 4.5 have shown that the period-doubling transition also occurs in the dsa-lattice. This structure is weak in comparison to the csa-lattice. This must be because of the relative thickness of the ligaments in each of the structures; in the dsa-lattice these are far thinner than in the csa-lattice. Non-uniform thickness appear central to the switching mechanism and this has been shown by the fact that no such switching effects occurred in the ssa-lattice.

Chapter 5

Pattern Switching in 3D Cellular Structures

Experiments were conducted to determine the buckling behaviour of a porous elastic cube with two sets of cylindrical voids. The voids crossed one fanother orthogonally and the load was applied at right angles to their plane of coincidence. The primary buckling state of the structure was essentially two-dimensional with a pattern switch in one direction and localisation in the other. The switch occurred in the cylinder set with the highest planar void fraction and this occurred at the same degree of compression as for the 2D csa-lattice. Where the two void sets were of the same size relative to the inter-void spacing, imperfections caused one of these to provide the preferred buckling mode of the structure. Pattern-switching was induced in the second void set by pre-straining the sample in two directions simultaneously. This secondary state was shown to become unstable in unloading tests, which indicated that there were large imperfections in the sample.

5.1 3D Cellular Structures

The central issue explored in Chapters 3 and 4 was the in-plane deformation of two-dimensional solids which had a regular, repeating planar geometry. Here, the uniaxial loading of regular *three-dimensional (3D)* cellular structures is considered. The structures are free to buckle in two directions orthogonal to the loading, either independently or simultaneously. Despite the increased structural complexity inherent in progressing from a two- to a three-dimensional cellular geometry it is well known that the effect of compression is similar in both of these system types [3]. There is an initial linear compression regime which levels off to a plateau phase as a result of the failure of the structure. Typically, failure in 3D systems causes the emergence of localised collapse and densification regions as opposed to the global behaviour described in Chapters 3 and 4 [3, 60, 61].

The most common example of a three-dimensional cellular structure is a *foam*, in which the cells have a random size distribution and connectivity, as well as various cell wall types [3]. However, recent studies have concentrated on pattern formation in ordered 3D structures. These have a geometry which is inspired by naturally-occurring photonic structures which exist on the micron scale [62, 63]. The techniques required to mimic the structure of these systems exist [64, 65] and as such there is the potential to create three-dimensional switching devices which respond to external stimuli and change their optical and audio transmission properties as a result.

5.1.1 Cubic Lattice

The particular structure under consideration in this chapter will be referred to as a *cubic lattice*. A schematic of this structure has been provided in Figure 5.1, in

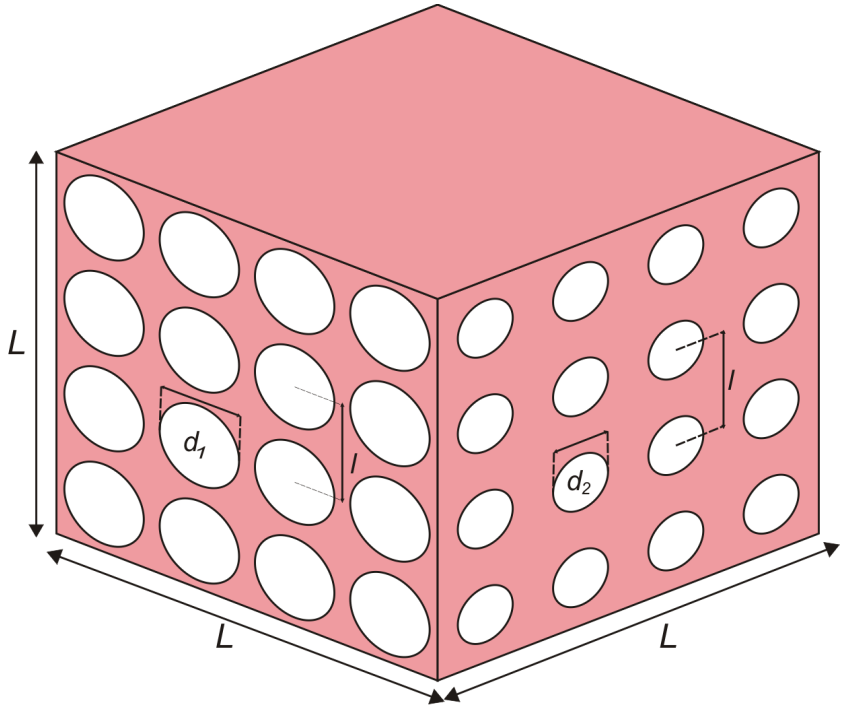

Figure 5.1: The cubic lattice. The structure is a block of elastic material (side length L) through which 2 sets of cylindrical voids permeate. The sets of voids have diameters d_1 and d_2 respectively and are arranged on square lattices with inter-void spacing l. The voids cross one another at right angles within the cube.

which three of its six faces are shown. The lattice is a cube of elastomer (side L) through which two sets of cylindrical voids cross one another at regular spatial intervals. The voids are oriented such that the central axes of the cylinders cross one another at right angles and each set passes through two opposing faces of the structure.

The porous planes of the cubic lattice possess the geometry of the csa-lattice described in Chapter 3. The sets of voids are each of diameter d_1 and d_2 respectively and are arranged in a 4×4 square array. The inter-void spacing l is the same in each plane. The planes are characterised by their respective void fractions

Φ_1 and Φ_2 and the 3D system will be henceforth labelled as a ($\Phi_1 \times \Phi_2$) cubic lattice. The convention used here is that, for void sets of contrasting size, $d_1 > d_2$ and hence $\Phi_1 > \Phi_2$. In order to draw comparison with 2D cellular structures, the void sets are referred to here by the *plane in which they enter the cubic lattice* For example, the effect of change in geometry on the void set where $d_1 > d_2$ is described as a change in the geometry of the *large void plane*.

5.1.2 Porosity

The cubic lattices are characterised not only by the Φ values of the two void sets but also by the *porosity* P [mm^3/mm^3] of the whole structure. The porosity is the three-dimensional equivalent of the void fraction and is defined as the volume of the voids relative to that of the whole cube, L^3. At the outset of the study it was assumed that, for higher P values, the decreased material presence in the cubic lattices would result in lower normalised stress values at a particular degree of compression. As with the definition of void fraction given in Chapter 3, the porosity can be calculated for a representative unit cell of the structure which is then used to characterise the whole system. The unit cell of the cubic lattice is a cube of side l (volume $V = l^3$) through which two cylindrical voids (length l) cross. Accordingly, P is given by

$$P = \frac{V_1 + V_2 - V_{12}}{V} \tag{5.1}$$

where V_1 and V_2 are the respective volumes taken up by each of the cylinders in the unit cell i.e.

$$V_i = \frac{\pi d_i^2 l}{4} = \Phi_i l^3 \tag{5.2}$$

for $i = (1, 2)$. Derivation of the common volume of the cylinders V_{12} is a nontrivial problem which has the solution [66]

$$V_{12}(d_1, k) = \frac{d_1^3}{3}\left[(1 + k^2)E(k) - (1 - k^2)K(k)\right] \tag{5.3}$$

In equation (5.3) $k = \frac{d_2}{d_1}$ and $K(k)$ and $E(k)$ are the complete elliptic integrals of the first and second kinds respectively. Both can be expressed as power series in k such that the common volume V_{12} reduces to[1]

$$V_{12} = \frac{2d_1^3}{3} \tag{5.4}$$

for $k = 1$, in which case the voids have the same diameter. The maximum porosity P_{max} of the cubic lattice is achieved when $d_1 = d_2 = l$ and according to equations (5.1) and (5.4) $P_{max} = \frac{\pi}{2} - \frac{2}{3} \approx 0.904$.

5.1.3 2D Geometry Interactions

The aim of the experiments was to determine the behaviour of cubic lattices under uniaxial loading compression by applying load to the top (non-porous) surface of the structure. It was possible to manufacture two different cubic lattices using the moulding techniques described in Appendix B: these were (0.60 x 0.41) and (0.60 x 0.60) cubic lattices for which $P = 0.70$ and 0.76 respectively.

It has been shown in Chapter 3 that pattern onset in the 2D csa-lattice geometry comes about as a result of an elastic buckling instability which occurs at a

[1]This is a strikingly simple result which was known to Archimedes [67].

critical strain ϵ_{cr}. The compression point at which the structure becomes unstable is proportional to $(\Phi_{max} - \Phi)^2$, i.e. the larger the diameter of the voids, the lower the critical strain. The two cubic lattice geometries considered here were made up of superimposed csa-lattice geometries and the void fractions were chosen such that pattern-switching would be observed in 2D samples possessing these respective arrangements of voids. However, it was unclear as to how the buckling modes of the two sets of orthogonal voids would interact and what consequences this would have for the cellular geometry of the structure.

If the two sets of voids act independently of one another, then 2D pattern-switching in one of the planar directions was expected in the experiments. Incrementing the applied strain from $\epsilon = 0.00$ mm/mm would cause the set of voids with the greater Φ value to form the pattern of mutually orthogonal ellipses. The primary buckling state of that void set would then dominate the 3D structure. This is simple to comprehend in the case of the (0.60×0.41) cubic lattice, for which pattern-switching in the $\Phi = 0.60$ planar direction was expected, but it is less clear for the (0.60×0.60) cubic lattice. In theory, buckling modes in each set of voids would be triggered at the same level of compression, unless there are structural imperfections which cause one direction to be preferred. If the above description of the interaction between the voids were to prove appropriate, this would be further evidence of the robust nature of the switching mechanisms described in Chapter 3. However, there may exist other buckling modes of the cubic lattice as the two void sets cannot necessarily be treated independently of one another.

5.2 Methodology

5.2.1 Manufacture and Testing

The experimental samples were made from Sil AD Soft ($E_s \approx 350$ kPa). In its initial fluid state this material is the least viscous of the addition-curing elastomers used in the study. This made it suitable for pouring into the millimetre-sized gaps which were present in the mould. The procedure followed in manufacturing the cubic lattices is described in full in Appendix B.

As well as manufacturing the cubic lattice samples, two reference samples were made using the same material. These were extended versions of the csa-lattice geometries described in Chapter 3 with increased out-of-plane width w. The data taken during experiments on these structures was required for comparison with that measured for the two cubic lattices. The reference samples had 4×4 square lattices of cylindrical voids which possessed the respective void fractions ($\Phi_1 = 0.60$ and $\Phi_2 = 0.41$) of the voids in the cubic lattice samples. The inter-void spacing l was the same for all four experimental samples. The cubic lattice and reference samples were tested using the aluminium loader attached to the compression machine and during the tests the compression speed was set to 0.01 mms^{-1}.

5.2.2 Boundary Removal

The initial compression tests performed on the cubic lattices showed localised behaviour in the cylindrical voids. In the images in Figure 5.2, two faces of the (0.60 $\times$ 0.41) cubic lattice are shown in the strain state $\epsilon = 0.10$ mm/mm. Within the large diameter void plane (Figure 5.2 (a)) the effect of buckling was the side-to-side shearing of the voids. The bottom row of voids in this plane were the most strongly affected i.e. the deformation was locally manifested. The result of this

was that the voids in the small void plane were sheared out-of-plane in an irregular manner. This is shown in Figure 5.2 (b), where, again the bottom row in the small diameter void plane has undergone a greater degree of deformation than the top rows. The same effect of in-plane deformation in on a dominant void set was observed in experiments on the (0.60×0.60) cubic lattice.

These preliminary experiments showed that buckling within one plane was the dominant effect on the cubic lattices. However, the form taken by these structures as a result of buckling gave no indication that the pattern-switching observed within the csa- and dsa-lattices was to be expected in the cubic lattice. It has been shown by Bertoldi et al [26] that the presence of thick side walls in the csa-lattice can affect the global nature of switching mechanisms and it was hypothesised that the faces of the cubic lattices may have played a similar role in the initial experiments.

Each of the cubic lattices were therefore modified by the removal of the porous cube faces using a sharp thin-bladed knife. These experimental samples possessed a reduced breadth and width and each lattice of voids comprised a 4×2 square array flanked by a column of four semi-circles on each side as a result. The side walls were also removed from the reference samples at this stage to replicate the alteration performed on the cubic lattice samples. As shall be documented in the following sections, the effect of the boundary removal was profound for the cubic lattices. All results presented henceforth were measured during experiments performed on the modified experimental samples.

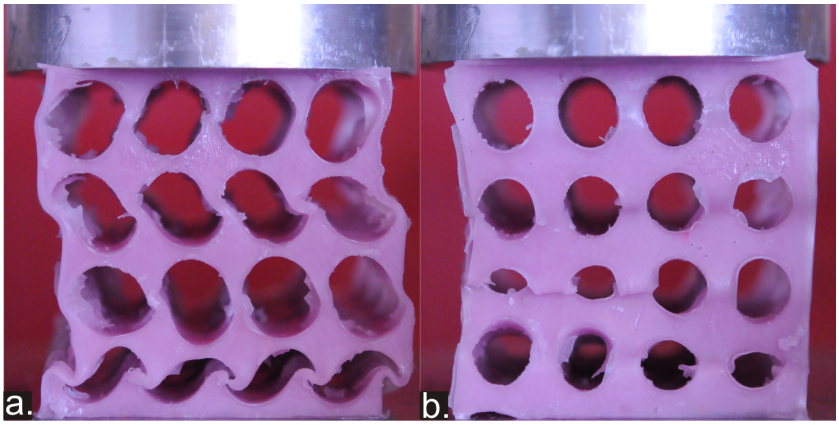

Figure 5.2: Localisation in the initial experiments. In the large void plane of the (0.60 × 0.41) cubic lattice (a) the voids underwent shearing as a result of the structure buckling. The buckling was localised and was most pronounced in the bottom layer of the voids. (b) The effect of the localised buckling in the large void plane was the irregular shearing of the small voids out of plane.

5.3 Results

5.3.1 Pattern Transformation

Reference Samples

The compression experiments confirmed that the effect of elastic buckling of the reference samples caused the initially circular voids to form mutually orthogonal ellipses. The structures are shown prior to compression in Figure 5.3 (a) and 5.3 (b) and at $\epsilon = 0.09$ mm/mm (Figure 5.3 (c)) and 0.15 mm/mm (Figure 5.3 (d)). As observed in Chapter 4, the necessary applied strain required to observe the pattern-switching effect was higher for the reference sample with the lower Φ value.

A striking feature of the images shown in Figure 5.3 is that the in-plane rotation of the interstitials was consistent along the axis of each of the voids. The coupling

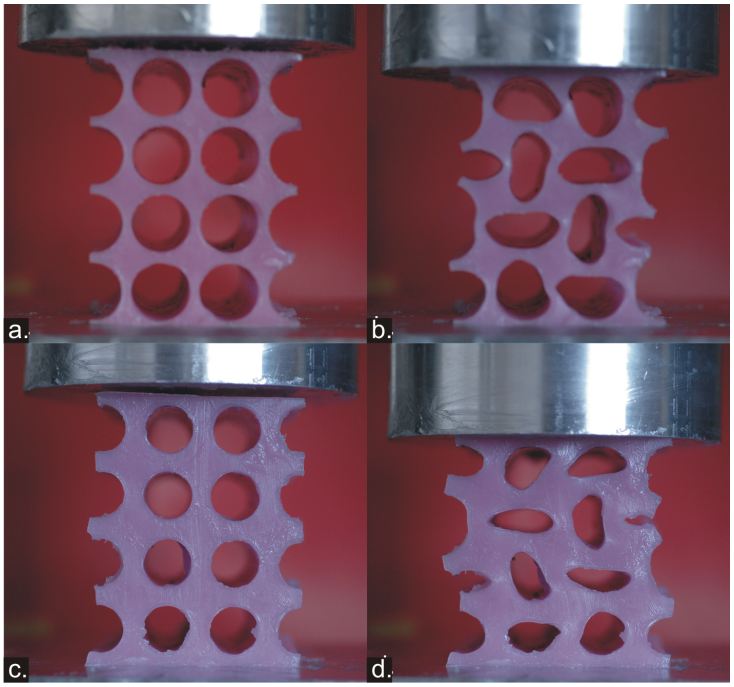

Figure 5.3: Pattern-switching in the reference samples. The $\Phi = 0.60$ and 0.41 reference samples are shown prior to compression (a and c, $\epsilon = 0.00$ mm/mm) and after the respective buckling events (b, $\epsilon = 0.09$ mm/mm and d, $\epsilon = 0.15$ mm/mm).

between the connectors remained strong despite the increased out-of-plane width and this was repeatable as described in Chapter 3. The experiments on the reference samples served to confirm that csa-lattices with the Φ values used to design the cubic lattice samples would show pattern-switching on their own.

Cubic Lattices

The form taken by each of the cubic lattices during the compression tests has been documented in Figures 5.4 and 5.5 respectively. In Figure 5.4 (a) the large void plane of the (0.60×0.41) cubic lattice is shown prior to compression and in Figure 5.4 (b) the small void plane is shown in the same strain state. In the images in

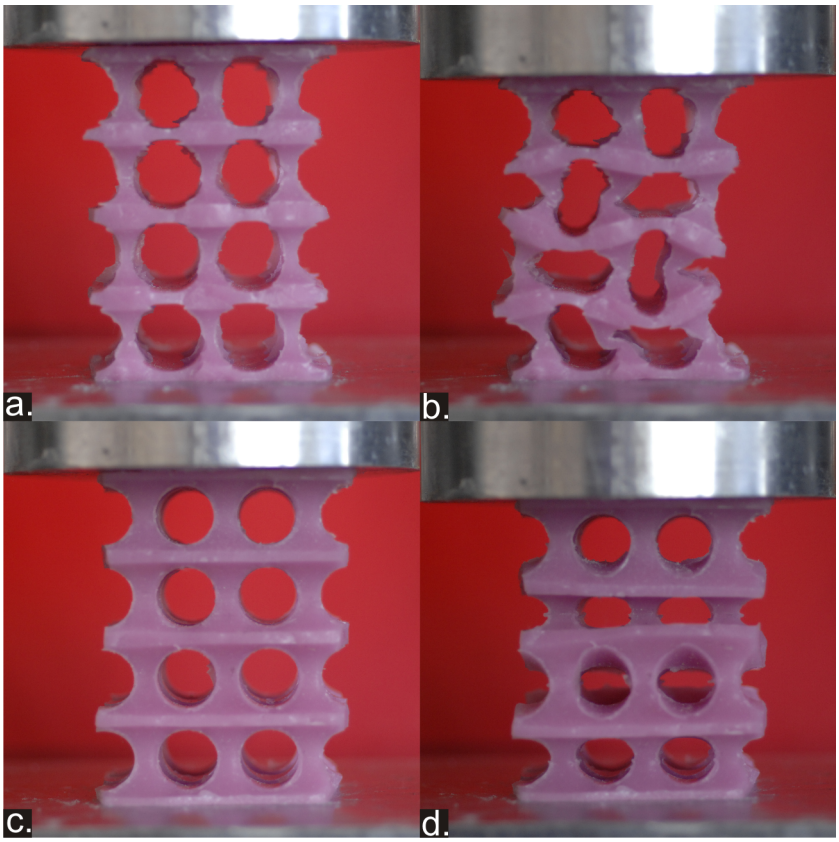

Figure 5.4: Pattern-switching in the (0.60 × 0.41) cubic lattice. The large (a) and small (c) void planes are shown prior to compression. The images in (b) and (d) are of the same planes at $\epsilon = 0.10$ mm/mm, and the effect of buckling on the respective void sets is clearly confined to one plane.

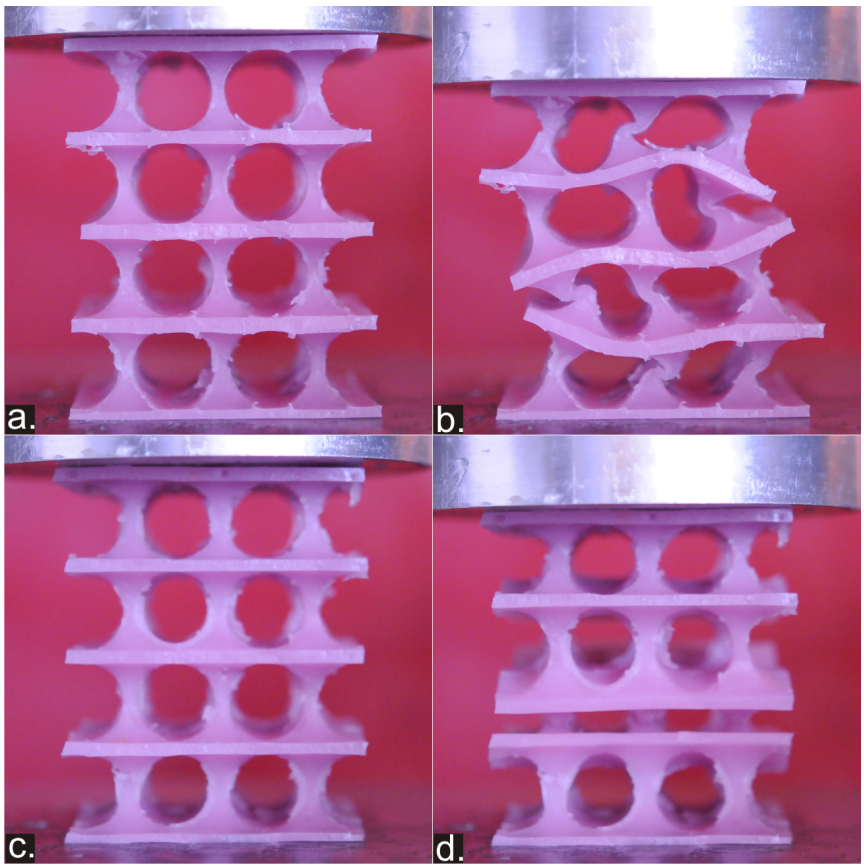

Figure 5.5: Pattern-switching in the (0.60 × 0.60) cubic lattice. In the experiments a pattern-switching plane (Plane 1) and a non-pattern-switching plane (Plane 2) were shown to exist. Planes 1 and 2 are shown prior to compression in (a) and (c) They are shown at a $\epsilon = 0.12$ mm/mm in images (b) and (d).

Figure 5.4 (c) and Figure 5.4 (d) these planes are shown at $\epsilon = 0.10$ mm/mm, which is after the buckling event occurred. The large void plane buckled into the familiar pattern of mutually orthogonal ellipses (Figure 5.4 (b)). The small diameter voids have become sheared out of plane (Figure 5.4 (d)); no evidence of pattern formation was observed in this planar direction.

Similar behaviour was observed in compression tests performed on the (0.60×0.60) cubic lattice. The images in Figure 5.5 are of each of the lattice planes prior to compression (Figure 5.5 (a) and (c) and at $\epsilon = 0.12$ mm/mm (Figure 5.5 (c) and (d)). As was observed in the (0.60×0.41) cubic lattice, the pattern formation was confined to one plane only. The consequence of this was that the other set of voids was sheared out of plane as shown in Figure 5.5 (d) and this was observed in repeated tests. For clarity, the planes of the (0.60×0.60) cubic lattice are labelled as Plane 1 (in which pattern formation was observed) and Plane 2 (non-pattern forming plane).

5.3.2 Normalised Stress-Strain Data

Reference Samples

The normalised stress-strain data measured in the uniaxial compression tests on the two reference samples is presented in Figure 5.6. As described in Section 6.3.1, both structures were observed to undergo elastic buckling and their normalised stress-strain curves were of the characteristic form associated with the buckling of cellular structures. Specifically, the response of the lattice to compression prior to its buckling comprised a linear normalised stress-strain relationship and buckling led to a plateau phase as in the 2D case. It is highlighted that strain softening effects were observed for the $\Phi = 0.41$ lattice, which is marked by the negative

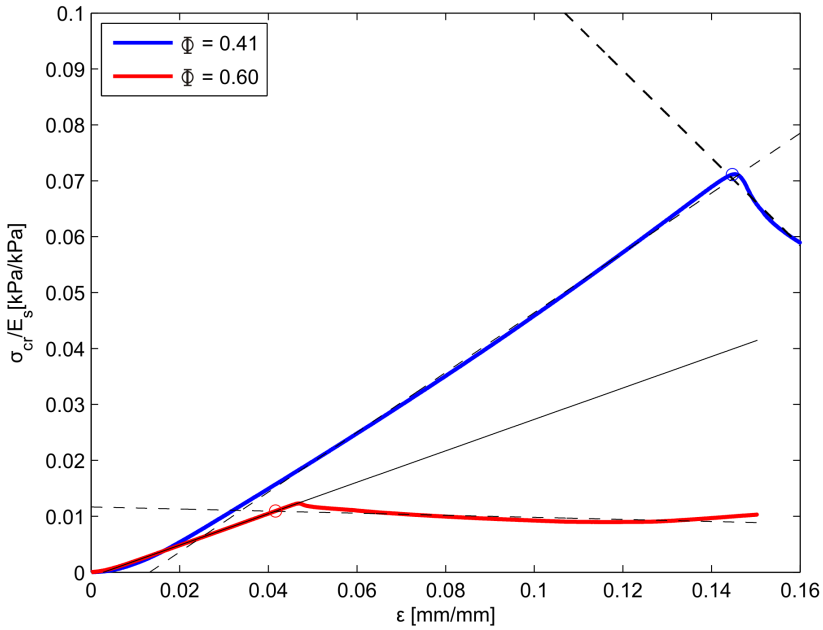

Figure 5.6: The normalised stress-strain data for the reference samples. Both lattices were observed to buckle elastically and the experimental results agree with those conducted on two-dimensional lattices.

slope of the normalised stress-strain curve post-buckling, whereas for the higher void fraction the plateau phase was flat. In this study, the coordinates of the critical point $(\epsilon_{cr}, \frac{\sigma_{cr}}{E_s})$ were determined by approximating the normalised stress-strain behaviour in each of the two phases as a linear relationship and finding the intersection of the two linear plots. These have been marked by the dashed black lines on the plots in Figure 5.6, and the critical points have been highlighted by a circle with the appropriate colour on each data set.

As observed in Chapter 3, the large void structure ($\Phi = 0.60$) was the weaker of the two, buckling at a low critical strain and normalised stress and with a lower stiffness. The coordinates of the critical points and the elastic moduli of the two

Φ	0.60	0.41
ϵ_{cr} [mm/mm]	$4.74 \pm 0.36 \times 10^{-2}$	$1.43 \pm 0.04 \times 10^{-1}$
$\frac{\sigma_{cr}}{E_s}$ [kPa/kPa]	$1.08 \pm 0.03 \times 10^{-2}$	$6.87 \pm 0.19 \times 10^{-2}$
$\frac{E}{E_s}$ [kPa/kPa]	$2.29 \pm 0.19 \times 10^{-1}$	$4.81 \pm 0.23 \times 10^{-1}$

Table 5.1: The critical strain, normalised critical stress and normalised elastic modulus of the reference samples.

reference samples have been listed in Table 5.1. Each of the measures quoted in the table are mean values determined from five repeated tests on each structure and the error on these values is the standard deviation from this value.

Cubic Lattices

The normalised stress-strain data measured in uniaxial tests on the (0.60 × 0.41) (red) and (0.60 × 0.60) (blue) cubic lattice samples has been plotted in Figure 5.7. The modified structures exhibited a similar normalised stress-strain response to the reference samples, and it was possible to identify an initial region of Hookean elasticity which led into a plateau phase of compression. The (0.60 × 0.41) cubic lattice was stiffer and stronger than the (0.60 × 0.60) cubic lattice and this can be seen by comparing the normalised critical stress and normalised elastic modulus values presented in Table 5.2. It was observed that both samples buckled at approximately the same level of compression: $\epsilon_{cr} = 4.79 \pm 0.09 \times 10^{-2}$ mm/mm and $4.78 \pm 0.11 \times 10^{-2}$ mm/mm respectively.

5.3.3 Critical Parameters

In Figure 5.8 the critical strain (Figure 5.8 (a)) normalised critical stress (Figure 5.8 (b)) and elastic modulus (Figure 5.8 (c)) have been plotted for the four experimental samples considered here. In each of the plots in Figure 5.8 the independent

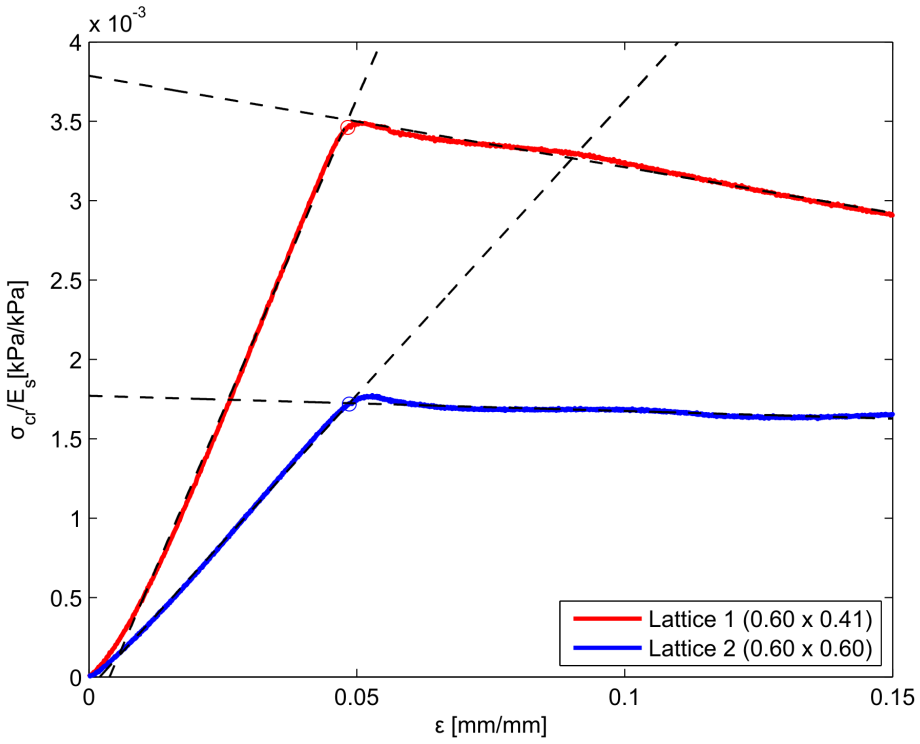

Figure 5.7: The normalised stress-strain data for the modified cubic lattice samples. The structures buckled under uniaxial compression at approximately the same strain value. The critical points for the lattices are each marked by a circle on the respective data sets.

$(\Phi_1 \times \Phi_2)$	(0.60×0.41)	(0.60×0.60)
ϵ_{cr} [mm/mm]	$4.79 \pm 0.09 \times 10^{-2}$	$4.78 \pm 0.11 \times 10^{-2}$
$\frac{\sigma_{cr}}{E_s}$ [kPa/kPa]	$3.49 \pm 0.15 \times 10^{-3}$	$1.61 \pm 0.10 \times 10^{-3}$
$\frac{E}{E_s}$ [kPa/kPa]	$7.30 \pm 0.79 \times 10^{-2}$	$3.37 \pm 0.71 \times 10^{-2}$

Table 5.2: The critical strain, normalised critical stress and normalised elastic modulus values for the cubic lattices.

variable is the porosity P of the sample, which in the case of the reference samples is simply the void fraction Φ.

The variation of ϵ_{cr} (red) confirms that the buckling of each of the cubic lattices is dominated by the 2D instability in the $\Phi = 0.60$ void set. In the reference samples, the critical strain increased as the void fraction was decreased and this is in agreement with the experimental observations described in Chapter 4. There is a deviation of less than 1% between the critical strain values of the cubic lattices and that of the $\Phi = 0.60$ reference sample which shows that the three structures buckled at the same degree of compression. This has been indicated by the dashed red line in Figure 5.8 (a) which links the ϵ_{cr} values measured for the higher porosity structures. This is particularly striking when considering the structural geometry of the cubic lattice; the presence of the additional set of voids had no effect on the onset of instability within the dominant void sets.

The strength and stiffness of the structures is affected by the presence of the two void sets and this has been illustrated in the plots in Figure 5.8. Both $\frac{\sigma_{cr}}{E_s}$ (blue) and $\frac{E}{E_s}$ (green) showed a decrease with increased porosity. The decrease in material presence served to weaken the cubic lattice as suggested in Section 5.1.2. In the experiments on the (0.60×0.41) cubic lattice, for example, elastic buckling was observed at twice the normalised stress as for the (0.60×0.60) cubic lattice.

5.4 Secondary State

The focus of the work on cubic lattices so far has been the effect of elastic buckling on the structural geometry of these structures under uniaxial compression. The buckling instability led to planar pattern-switching in one plane (Plane 1) and

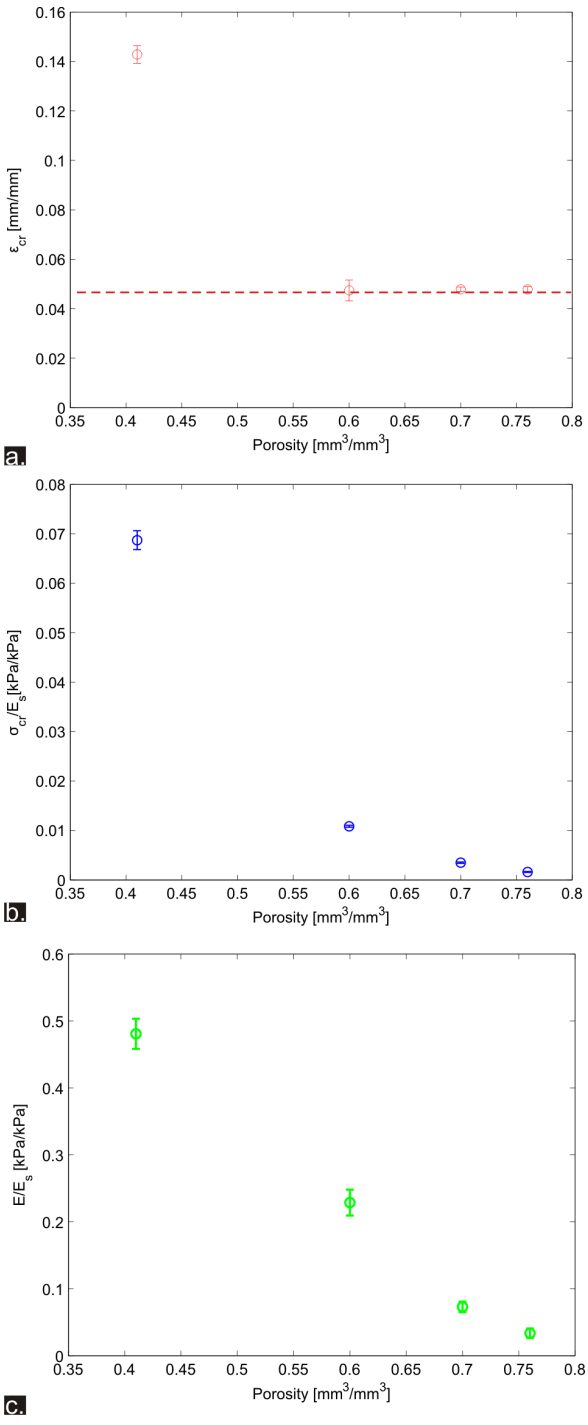

Figure 5.8: The variation with P of ϵ_{cr} (a), $\frac{\sigma_{cr}}{E_s}$ (b) and $\frac{E}{E_s}$ (c) for the (0.60 $\times$ 0.41) and (0.60 $\times$ 0.60) cubic lattices. The values are compared to the same measures for the reference samples.

out of plane buckling in the other (Plane 2). This can be considered to be the evolution of the primary state of the cubic lattice. There will exist a secondary state which forms in the same direction but where the pattern is shifted in phase by one void, as discussed for the csa-lattice in Chapter 3.

In the cubic lattices the interaction between two perturbed pitchfork bifurcations which describe the equilibrium states of the two respective void sets must be considered. Secondary bifurcations have been shown in systems with multiple bifurcation pointed to result in a rich bifurcation structure in which equilibrium branches exchange stabilities under certain conditions [68]. This leads to the creation of new equilibirium states and a complex range of stabilities and instabilities. In the cubic lattice, the dominant void set in the cubic lattice is chosen either as a result of the contrasting void diameters (as observed in the (0.60 $\times$ 0.41) cubic lattice), or by imperfections as was the case where the voids were of nominally equal size. Intuition suggests that a stable state associated with pattern-switching in Plane 2 of the (0.60 $\times$ 0.60) cubic lattice should exist and this is the focus in this section. By performing the study it should be possible to estimate the extent of the imperfections in the system which caused pattern formation in Plane 1 to dominate the buckling of the 3D structure.

5.4.1 Methodology

A biaxial compression technique was used to induce the secondary state consisted of pre-straining the cubic lattice in both axial and transverse compression directions. The steps taken to apply biaxial pre-strain to the cubic lattices are shown in the schematic in Figure 5.9. Two Perspex sheets (42.0 mm $\times$ 50.0 mm) were attached to a clamp and positioned either side of the cubic lattice (Figure 5.9 (a)). A layer of Vaseline was applied to the surface of each of the plates to aid their

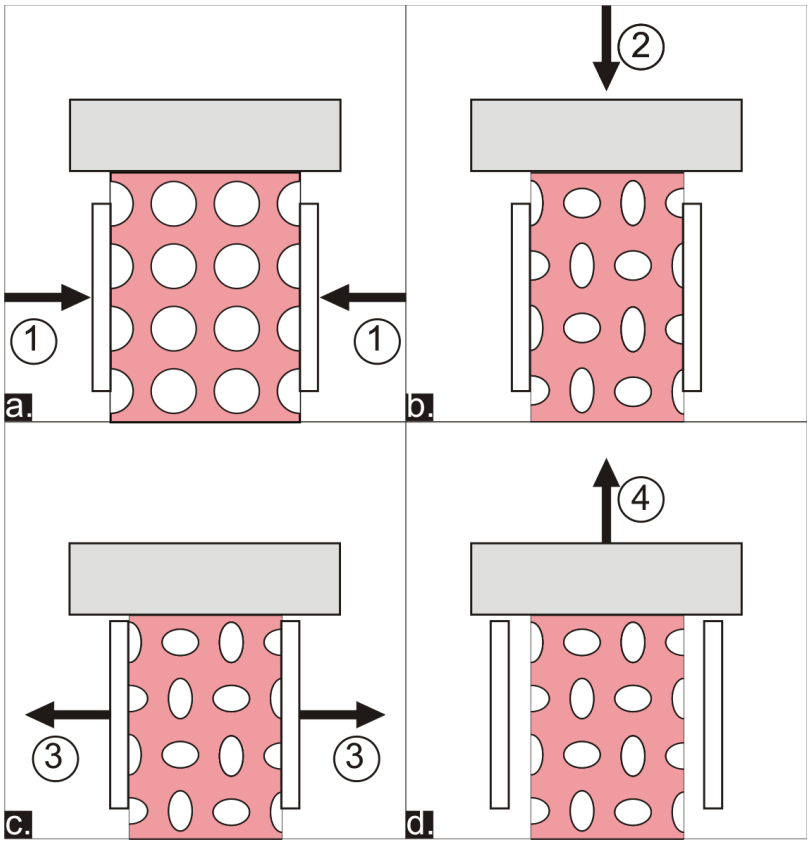

Figure 5.9: The biaxial method. (a) The Perspex plates were aligned to apply transverse strain to Plane 2 when they were tightened. The strain was increased such that the pattern of mutually orthogonal ellipses was induced in Plane 2. (b) The aluminium loader was lowered to apply axial strain to the top surface of the experimental sample. (c) The Perspex plates were loosened and removed from the experimental setup. The axial strain held the pattern in place. (d) The sample was unloaded in a controlled manner at a constant speed of 0.005 mms^{-1} to test the stability of the induced secondary state.

removal at a later stage. The sample was oriented such that tightening the clamps (Step 1) applied transverse strain ($\epsilon_{tr} = 0.065$ mm/mm) to Plane 2 of the experimental sample. This was sufficient to cause formation of the orthogonal elliptical pattern in Plane 2 of the (0.60×0.60) cubic lattice.

The aluminium loader was then lowered (Step 2) onto the top surface of the sample applying an axial strain ϵ. This reinforced the pattern which had formed in the cubic lattice (Figure 5.9 (b)). The clamps were loosened and removed from the setup by sliding them away from the experimental sample (Step 3). The cubic lattice tended to switch to the primary state if this process was not performed carefully and slowly. Having removed the plates the secondary state was held in place by action of the axial compression (Figure 5.9 (c)). A minimum axial strain ($\epsilon = 0.20$ mm/mm) was required to ensure that the cubic lattice remained in this state. The stability of the secondary state was tested by unloading the structure at a constant speed (Step 4, Figure 5.9 (d)). As with the unloading experiments described in Chapter 3, the speed of the unloading experiments was lowered to 0.005 mms^{-1} in order to reduce material hysteresis effect and provide a high resolution in the experimental data.

5.4.2 Results

In the plot in Figure 5.10 two normalised stress-strain data sets are shown. The first is a loading (red) - unloading (blue) curve for the (0.60×0.60) cubic lattice. For this data set it was observed that the features of the loading data were mimicked qualitatively by the unloading curve. During loading a transition between the trivial and pattern-switched geometries in the switched state at a critical strain $\epsilon_{cr} = 0.0481$ mm/mm and densification of the voids is marked by the increase in normalised stress values at high strains ($\epsilon > 0.20$ mm/mm). These processes are

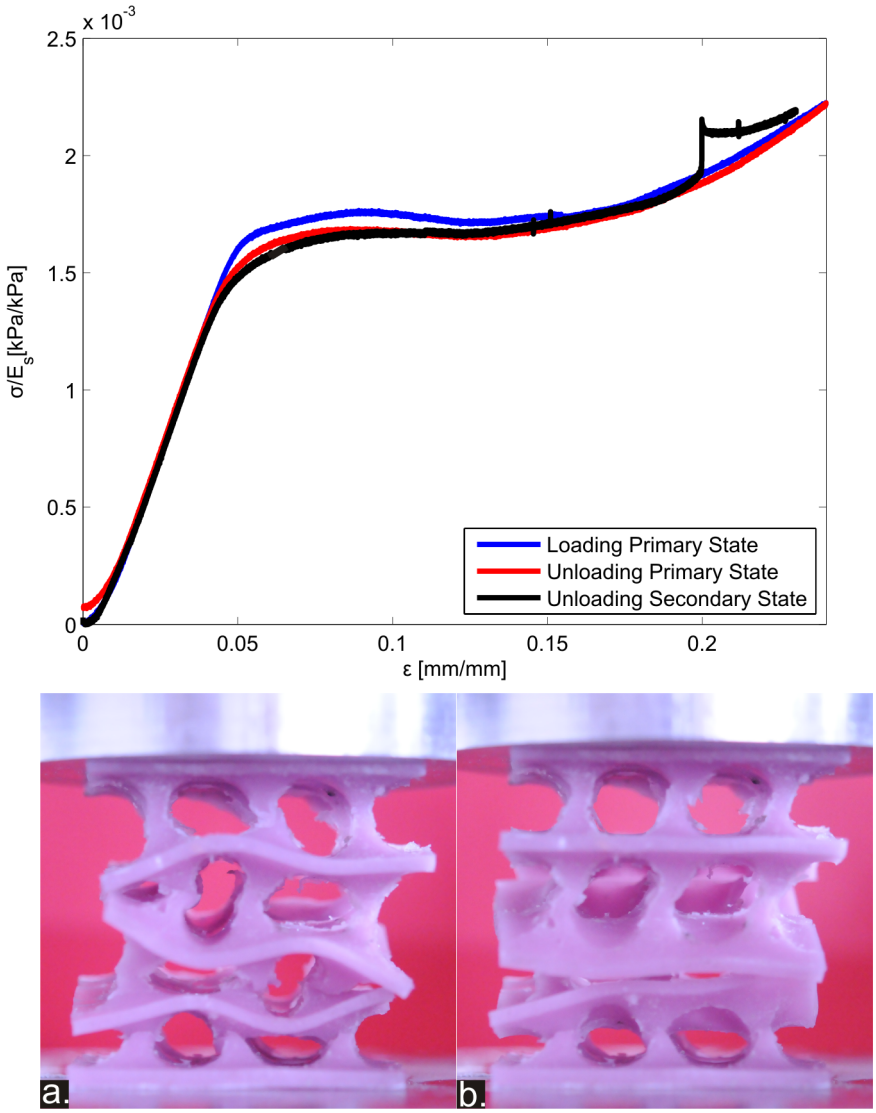

Figure 5.10: The normalised stress-strain data for loading of the primary state (red), the unloading of the primary state (blue) and the unloading of the structure in the secondary state (black). The drop in the normalised stress value during unloading of the secondary state occurred because the structure to the primary state. (a) The cubic lattice is shown in the secondary state at axial strain $\epsilon =$ 0.21 mm/mm. (b) The structure is shown at $\epsilon = 0.18$ mm/mm which is after the secondary state became unstable.

reversed by the unloading of the structure. The unloading curve lies slightly below the loading curve as a result of the hysteresis of the material during unloading.

The black curve is the unloading curve of the secondary state induced using the biaxial pre-strain technique described in Section 5.4.1. At the beginning of the test (high ϵ values) the normalised stresses required to hold the secondary state in place were higher than those associated with the unloading of the primary state. This is a similar observation to that made in Chapter 3 when comparing the normalised stress of the csa-lattice in the primary and secondary states; the latter existed at a higher normalised stress value than the former.

A large drop in the normalised stress value in the unloading of the secondary state experiment was observed at $\epsilon = 0.198$ mm/mm. After this, there was excellent agreement between the two unloading data sets. The cause of the reduction in the normalised stress value at this point was the switching of the lattice from the secondary to the primary state, which resulted from the secondary state becoming unstable at this point. The result of the transition from the secondary to the primary state of the (0.60×0.60) cubic lattice is shown in Figure 5.10. Plane 1 is visible at $\epsilon = 0.21$ mm/mm (Figure 5.10 (a)) and $\epsilon = 0.18$ mm/mm (Figure 5.10 (b)) respectively. There was a dramatic switch in the geometry of the structure between these points in the unloading experiment. The voids shown switched from a planar pattern of mutually orthogonal ellipses to voids which have been sheared out of plane. Within Plane 1 (not shown) the reverse is true.

Again, the behaviour observed here is similar to the 2D case considered earlier in Chapter 3. However, there is a contrast in the apparent size of the imperfection. In the experiments on the csa-lattice the secondary state was shown to become

unstable in close proximity with ϵ_{cr} for the structure and this implied that the imperfections in the system were small. Here, the difference between the strain point at which the secondary state became unstable and the critical strain is $\Delta\epsilon \approx 0.15$ mm/mm, which is large and implies that the primary and secondary states are separated to a large extent despite the fact that the voids in each plane were nominally the same size.

5.5 Summary

This study has provided an insight into the compression of elastic structures through which two sets of circular voids arranged on a square lattice permeate. The sets of cylindrical voids with the highest Φ values underwent pattern-switching to an array of mutually orthogonal ellipses as a result of uniaxial compression. When two such lattices were combined, the resulting three-dimensional structure buckled into a primary state with planar pattern formation. In both structures the degree of compression required to cause buckling agrees with that required to cause pattern-switching in its dominant plane. These results suggest that the instabilities in both sets of cylindrical voids competed with one another, with the large diameter voids providing the buckling mode for the cubic lattice. The effect of the second void set was simply to reduce the resistance to loading of the structure by reducing the material presence.

The void sets behaved independently of one another and this observation was maintained even when the voids in each lattice are of the same size. In this case imperfections caused the buckling of one void set to dominate the structure. It has been shown that it is possible to induce a secondary state in the (0.60×0.60) cubic lattice which consists of the formation of the elliptical pattern in Plane 2

and out-of-plane shearing effects in Plane 1. An initially high level of axial strain was required to induce the state and this became unstable within a small strain range which caused a switch in lattice geometry back to the primary state. The implications of these observations are that it is not possible for the two states to co-exist: the elliptical pattern cannot form in both planes at the same time. In addition, the cubic lattice is highly sensitive to imperfections in the manufacturing process which have shown to have a considerable effect on the structure's stability.

Chapter 6

Pattern Formation in Granular Crystals

A granular crystal comprising an ordered mixture of rigid and soft cylinders was subjected to uniaxial compression tests. The cylinders were initially arranged on a square lattice with the hard cylinders embedded in the soft array. A pattern-switching mechanism was observed whereby the rigid cylinders fell through gaps in the compressed crystal and formed vertically aligned pairs. The manner in which the cylinders were rearranged and the reversibility of the deformation process were primarily governed by the size ratio of the two cylinder sets. Good agreement was found between the experimental results and those of finite element and molecular dynamics simulations.

6.1 Granular Crystals

6.1.1 Motivation

The experiments described in this chapter were conducted on an ordered two-phase granular structure called a *granular crystal*. The inspirations for the study of this system came from a wide range of scientific fields. Whilst granular media have have been extensively studied [69] and are known to show interesting segregation behaviour [70, 71], research into ordered granular systems has been largely limited to the use of one-dimensional granular chains as acoustic filters [72] and shock absorbers [73, 74]. The 2D granular crystal is an extension of this type of structure and it possesses a structural geometry similar to that of martensitic crystals [75]. In these structures a stress-induced diffusionless solid-to-solid phase transition is observed at the atomic scale and this is the basis of shape memory behaviour.

The geometry of the granular crystal is shown in the schematic in Figure 6.1. The crystal comprises an array of large rubber cylinders (pink) embedded with one of smaller PTFE cylinders (white) such that each rigid cylinder is surrounded by four soft ones. The cylinders in the granular crystal are analogous to the particles in the martensitic crystal[1], although the interactions between the constituent particles in the two systems are markedly different. The goal of the experiments was to determine whether uniaxial compression of the granular crystal could bring about a coordinated transformation in its geometry similar to the martensitic transition [75]. If this were to occur, there would be potential for developing tunable granular devices similar to those which utilise the pattern-switching properties of the csa-lattice [40].

[1]For clarity, in this chapter the labels "particle" and "cylinder" shall be used interchangably when referring to the components of the granular crystal.

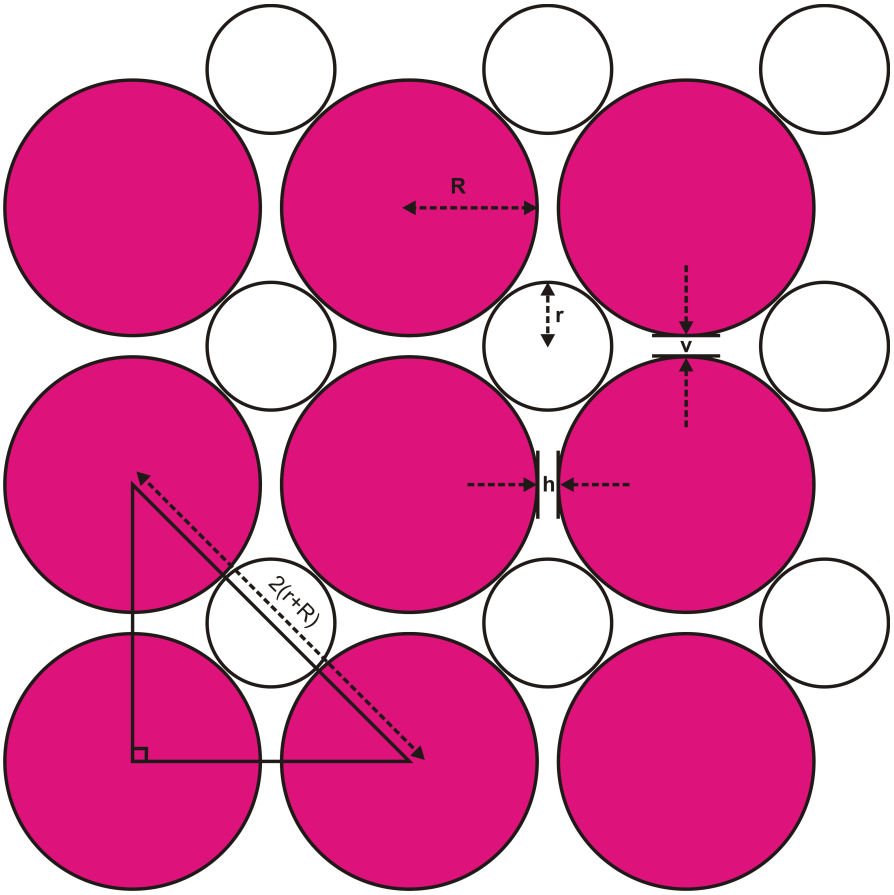

Figure 6.1: The granular crystal. The structure comprised regular arrays of rigid PTFE (white, radius r) and soft rubber (pink, radius R) cylindrical particles. The centres of the neighbouring soft particles were aligned according to a right-angled triangle of hypotenuse $2(r + R)$.

There are similarities between the granular crystal and the cellular structures considered in the previous chapters. For example, both systems possess a high degree of symmetry in their uncompressed states and are comprised primarily of elastomeric material. A clear contrast between the two systems is the mobility of their constituent components. The cellular structure is a fully connected system and compression of the experimental samples caused the voids to change shape in a reversible and repeatable manner. In contrast to this, the granular crystal was made up of discrete pieces which were free to move according to contact forces exerted by neighbouring particles and it was an open question as to whether new patterns would form in the structure under uniaxial loading conditions. If so, it was unclear whether this would come about via global switching events similar to those described in Chapters 3, 4 and 5 or if local effects would be observed.

6.1.2 Structural Geometry

The radii of the soft and hard cylinders in the granular crystal are R and r respectively and the spacing between neighbouring soft cylinders is h in the horizontal and v in the vertical planar directions. The granular crystal geometry is described by two dimensionless parameters, which are defined because the experimental observations are independent of length scale but depend on relative measures. The first of these is the particle size ratio χ which is defined as

$$\chi = \frac{r}{R} \tag{6.1}$$

and the second is the gap ratio ξ which is the ratio of the horizontal to vertical gap sizes i.e.

$$\xi = \frac{h}{v} \tag{6.2}$$

In addition to χ and ξ, the geometry of the granular crystal is fully described by the number of rows n and columns m of soft particles in the crystal. The rigid particles are arranged on an $(n-1) \times (m-1)$ square lattice.

The focus here is on the compression of granular crystals in which the cylinders were arranged in a square lattice, i.e. for geometries where $\xi = 1$. Appropriate values of h and v were chosen to create the square lattice using the fact that the centres of neighbouring particles were joined by a right-angled isoceles triangle with hypotenuse $2(R + r)$ as shown in Figure 6.1. The spacings were calculated using equation (6.3) below

$$h = v = \left(\sqrt{2}(1 + \chi) - 2\right) R \tag{6.3}$$

6.2 Methodology

6.2.1 Experimental Setup

In the experiments the soft particles (radius $R = 5.05 \pm 0.07$ mm, length $L = 10.05 \pm 0.12$mm) were made from Sil AD Soft ($E_s \approx 350$ kPa) using the cylindrical moulds described in Appendix B. The rigid particles were cut to appropriate lengths from PTFE rods ($E_p \approx 500$ MPa) using a sharp thin-bladed knife. There was an elasticity ratio $\frac{E_p}{E_s} \approx 10^3$ between the two particle types.

Two sets of PTFE cylinders with radii $r_1 = 2.70 \pm 0.05$ mm and $r_2 = 3.10 \pm 0.05$ mm were used in the experiments. Hence, the behaviour of granular crystals

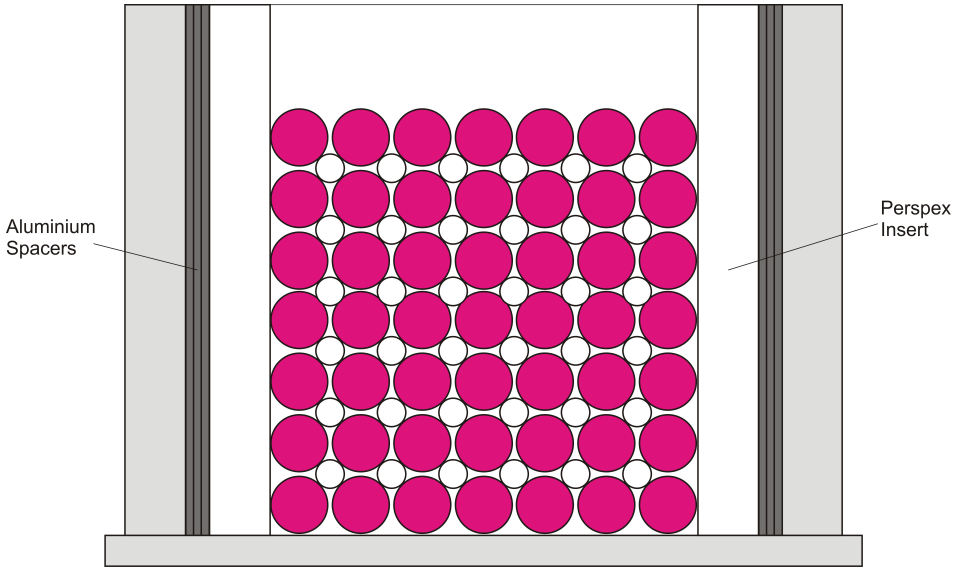

Figure 6.2: The experimental setup. The granular crystal was housed in a modified version of the Perspex housing described in Chapter 2. This incorporated Perspex sheets and aluminium spacers to reduce the internal width.

with size ratios $\chi = 0.53$ and 0.61 respectively were studied. The spacings required to achieve the square lattice were calculated using equation (6.3) and were 0.86 mm and 1.50 mm respectively.

The Perspex housing and loader were used in the experiments and compression tests were performed at a range of speeds. The data presented in this chapter was for a test with speed 1.00 mms^{-1}, although the experimental observations were rate-independent. Two rectangular Perspex sheets were put in place to reduce the inner width of the housing (Figure 6.2) in order to accommodate the granular crystal and provide a fixed boundary on either side of the sample. The width of the experimental housing could be adjusted to suit the crystal dimensions by the addition of aluminium spacers of thickness 1.50 ± 0.05 mm. The soft particles were arranged in an 8×10 lattice in the experiments on the $\chi = 0.53$ granular crystal

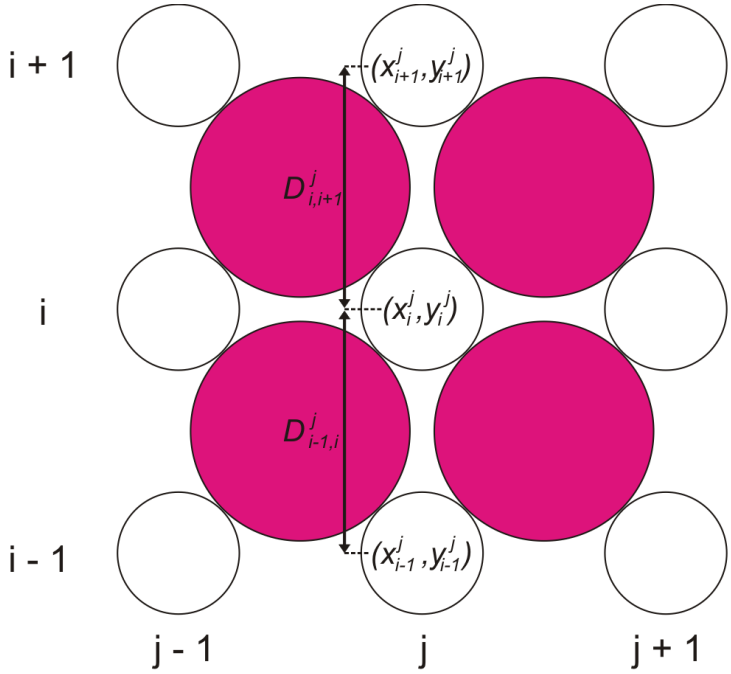

Figure 6.3: The inter-particle distance. $D^j_{i,i+1}$ was calculated for neighbouring rigid particles (i and $i+1$) within column j. The coordinates of the centres of each rigid particle were measured using image analysis techniques.

and in a 9×9 lattice for the $\chi = 0.61$ crystal to suit the housing dimensions. The crystals were built by hand prior to each experiment and the constituent particles were covered in Vaseline to reduce friction effects. The width and the height of the granular crystal was measured using Vernier callipers prior to the experiment.

6.2.2 Inter-Particle Distance

The image analysis technique described in Chapter 3 was used to calculate the distance between the rigid particles in the granular crystal. A low black-white threshold was required to differentiate between the white rigid components and the darker soft cylinders when binarising the digital images. The distance $D^j_{i,i+1}$ between neighbouring rigid particles in rows i and $i+1$ within column j was

calculated as

$$D^j_{i,i+1} = \sqrt{(x^j_{i+1} - x^j_i)^2 + (y^j_{i+1} - y^j_i)^2} \tag{6.4}$$

where x and y were the coordinates of the centres of each rigid particle. In equation (6.4) the index j is the column number and i is the row number as sketched in Figure 6.3. According to the naming convention used here the left-most column of rigid particles has superscript $j = 1$ and the bottom row has subscript $i = 1$.

6.2.3 Simulations

Numerical simulations were performed alongside the experiments on the granular crystals [76]. In the finite element simulations (FEM, [77]) the particles were modelled using the commercial software ABAQUS as nearly compressible neo-Hookean solids with the Young's moduli and radii listed in Section 6.2.1. A small Coulomb-type friction ($\mu = 0.01$) was used to replicate the friction between the particles in the experiments and plane strain conditions were applied in the calculations.

In addition to the FEM simulations, a two-dimensional soft molecular dynamics (MD, [78]) model was constructed in which the inter-particle forcing f was calculated as

$$f(\delta) = k_1\delta + k_2\delta^\alpha \tag{6.5}$$

where δ is the geometrical overlap between particles. The contact parameters k_1, k_2 and α were determined from contact simulations between the different particle types and varied for soft-soft, soft-hard and hard-hard interactions. The Coulomb-type friction was also incorporated in the MD simulations and the same parameters

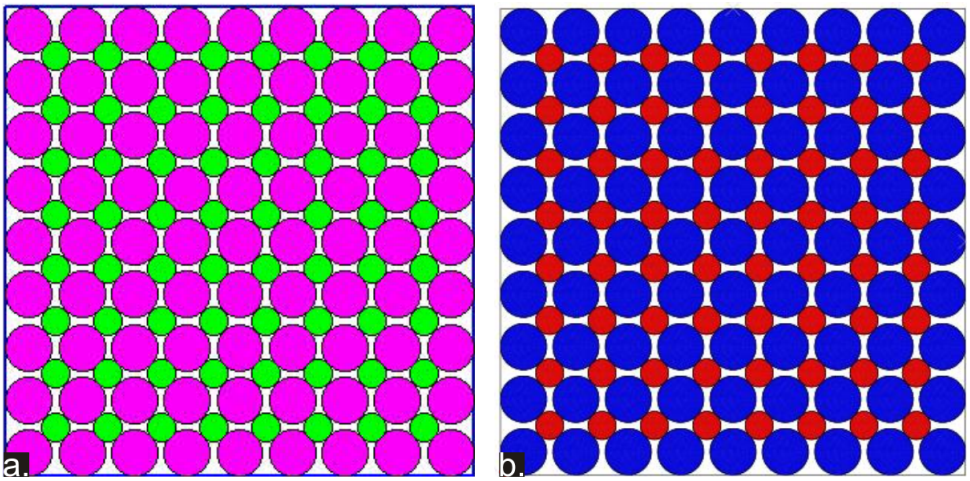

Figure 6.4: The numerical crystals. In the MD (a) and FEM (b) simulations of the granular crystal the geometry of the experimental sample and the testing conditions were replicated.

were used as in the FEM study. The simulations are described in greater detail elsewhere [76, 79]. The conditions of each experimental test - compression speed, particle spacing, boundary conditions and lattice size - were replicated in each numerical compression test. In Figure 6.4 the uncompressed $\chi = 0.61$ granular crystal is shown for the MD (Figure 6.4 (a)) and FEM (Figure 6.4 (b)) simulations respectively. In the MD simulations, the soft particles are pink and the rigid particles green, whereas in the FEM simulations they are blue and red respectively.

6.3 Pattern Switch

6.3.1 Experiments

Uniaxial compression of the granular crystal gave rise to a new pattern whereby the rigid particles formed pairs with their nearest neighbours. To illustrate the pattern switch, the $\chi = 0.53$ granular crystal is shown in strain states $\epsilon = 0.00$

mm/mm and $\epsilon = 0.25$ mm/mm in the images in Figure 6.5 (a) and (b). Compression of the crystal has caused the soft particles to form buckled chains and gaps have been created between these. The initially isolated rigid particles have been pushed into the gaps and have formed rigid particle pairs. These are aligned in the direction of loading and are arranged throughout the structure in a chess-board pattern. This switch in the crystal geometry was consistently achieved in experiments on granular crystals with both of the size ratios used in the study.

The pattern switch described above was a period-doubling transformation of the crystal's structural geometry and is similar to that observed in experiments on csa-lattices described in Chapter 3. In both systems, the unit cell which characterised their respective planar geometries became enlarged as a result of the formation of new pattern. Initially, the unit cell of the granular crystal was square and enclosed one soft and one hard particle as illustrated in Figure 6.5 (c). In the pattern-switched state the unit cell contained two of each particle type and this has been sketched in Figure 6.5 (d).

6.3.2 Simulations

The advantage of the numerical approaches described in Section 6.2.3 was that the components of the granular crystal did not have inconsistencies in construction since the particles were perfectly round and could be positioned precisely. The images in Figure 6.6 are of the experimental (a, d), FEM (b, e) and MD (c, f) crystals at $\epsilon = 0.25$ mm/mm. Both sets of simulations show excellent qualitative agreement with the experiments and replicate the pattern formation described in Section 6.3.1. This is remarkable because, as described above, the effect of imperfections in the crystal is reduced significantly by conducting the numerical study. In addition to this, there is little experimental control on friction in the experi-

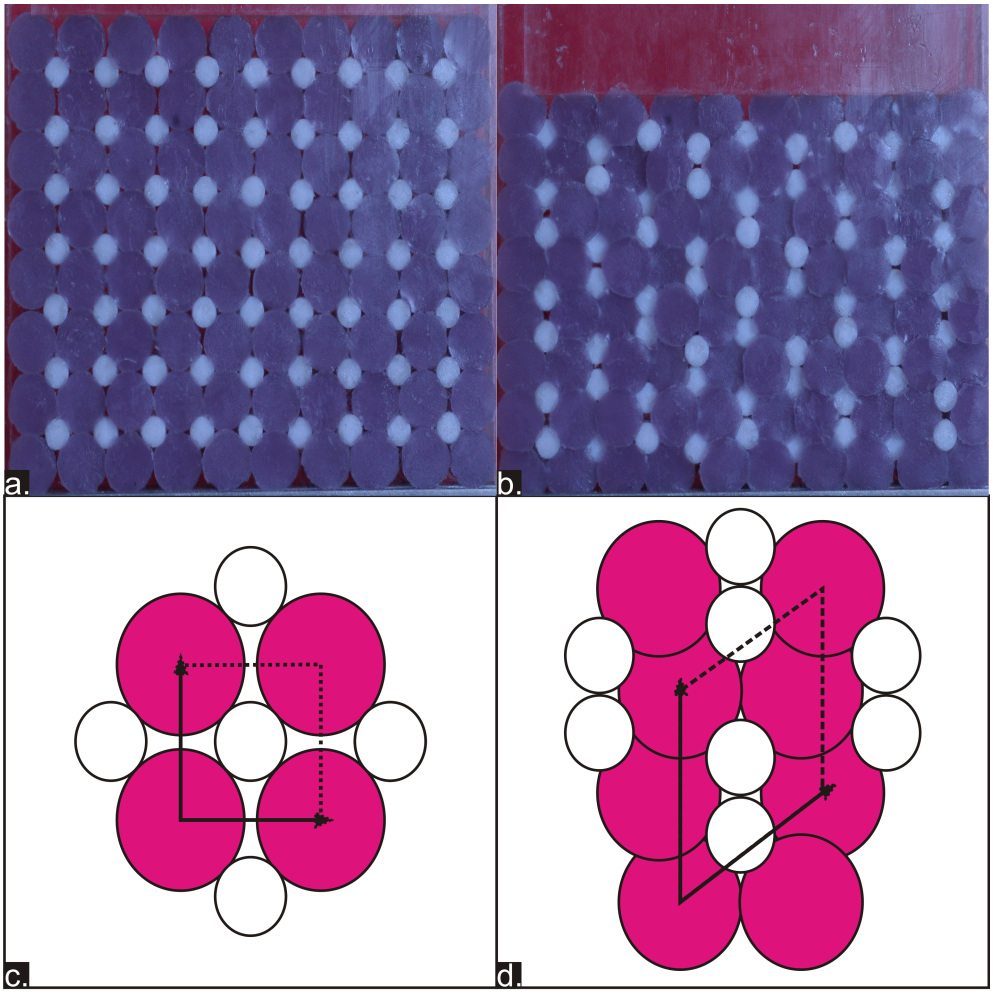

Figure 6.5: The pattern switch of the $\chi = 0.53$ granular crystal. The planar geometry evolved from the initial (a, $\epsilon = 0.00$ mm/mm) to the pattern-switched (b, $\epsilon = 0.25$ mm/mm) state as a result of compression. The switch was characterised by the expansion of the initially square unit cell (c) such that it enclosed two of each particle type in the pattern-switched state (d).

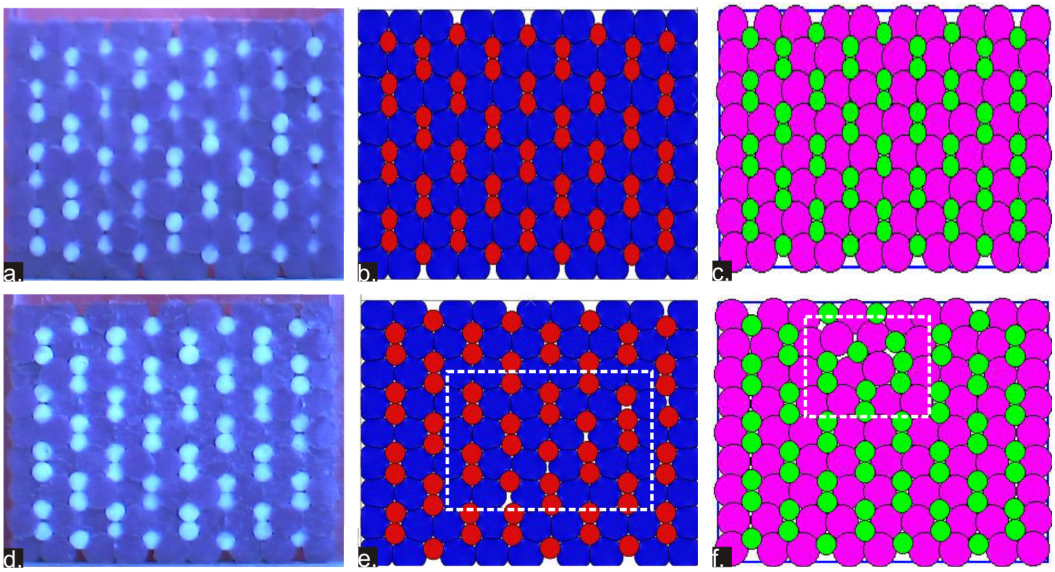

Figure 6.6: The granular crystals at $\epsilon = 0.25$ mm/mm. The $\chi = 0.53$ (a - c) and $\chi = 0.61$ (d - f) crystals underwent pattern-switching but in the simulations the crystal with the higher size ratio exhibited some localised deformation (e and f respectively).

ments and these can vary in each test. The simulations are also 2D, whereas the experiments are 3D.

In the simulations of the crystal with $\chi = 0.53$ (Figure 6.6 (b) and (c)) the fully pattern-switched state of the crystal was achieved. The simulations of the $\chi = 0.61$ crystal differ marginally from the experimental observations. As can be seen in the images in Figure 6.6 (e, FEM) and (f, MD), localised chains formed and particles became isolated as indicated by the dashed white box in each image. This came about because of the contrasting deformation mechanisms in each crystal which are described in Section 6.4. Despite this localised discrepancy, the majority of the rigid particle pairs have been found to form pairs in both simulation types and this is a striking result.

6.3.3 Two Potential States

There were two possible outcomes for the rigid particles when the paired state was formed. Each particle, other than those at the top and bottom boundaries of the system, became either the top or bottom particle in a rigid particle pair. There were therefore two branches which represent the motion of the individual particles when the crystal was compressed. In Figure 6.7 the change in distance ΔD for a *triplet* of rigid particles (i = 3, 4 and 5) in column $j = 3$ of the $\chi = 0.53$ crystal has been plotted. Specifically, $\Delta D^3_{3,4}$ (red) and $\Delta D^3_{4,5}$ (blue) have been plotted in order to illustrate the two branches described above.

Prior to the transition, the distance between particle 4 and its neighbours above and below decreases linearly. However, at $\epsilon \approx 0.12$ mm/mm the two data sets diverge. ΔD^3_{34} decreases whereas ΔD^3_{45} shows a steady increase. This is reflected in the position of the particles in the paired state. Particles 4 and 5 formed a vertical pair together, whereas particle 3 was the top particle in the pair below. The data sets in Figure 6.7 show that the rigid particles follow contrasting paths as a result of macroscopic compression. All of the particles are shifted in the direction of loading but to different degrees. In this experiment, ΔD^3_{34} decreased by 6.5 mm at the end of the test; ΔD^3_{45} increased by approximately 1 mm in the same strain state.

A secondary state must exist in which the triplet is split up such that particles 3 and 4 form a pair, with particle 5 taking the position of bottom particle in the pair above. In the inset illustrations in Figure 6.7 the two possible states have been sketched to highlight this. The effects of the many sources of imperfections input during the construction of the crystal will determine the final state of the crystal and cause there to be a preferred stable branch which describes the evolution of

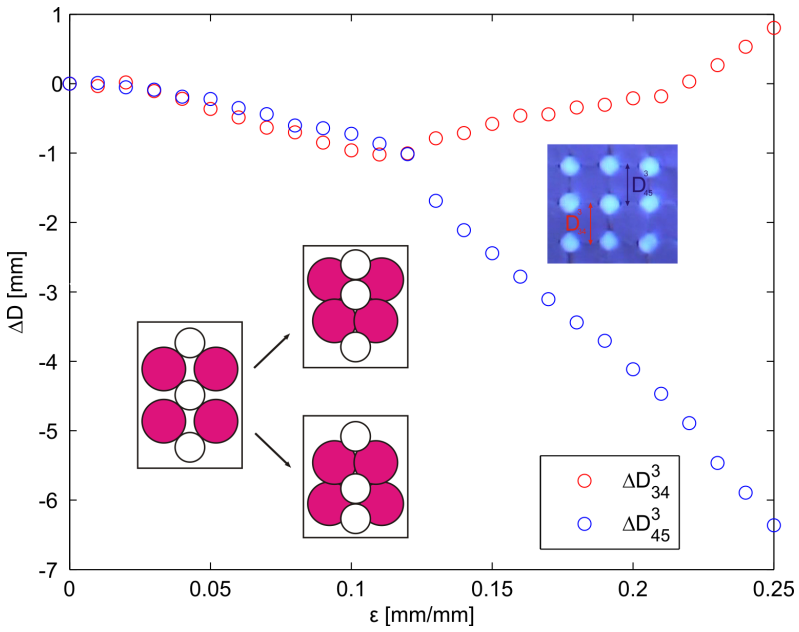

Figure 6.7: Monitoring inter-particle distances. $\Delta D^3_{3,4}$ (red) and $\Delta D^3_{4,5}$ (blue) have been plotted to show the splitting of the three particles. The inset illustrations are of the two possible configurations of the rigid particle triplet in the paired state.

the system's geometry.

6.4 Switching Mechanisms

The switched state was a robust feature of the experiments. However, the precise nature of the transition between the initial and final states was found to depend on the size ratio χ. Two distinct switching mechanisms were observed: the first was a gradual, direct change in the geometry whilst the second involved the creation and destruction of *shear bands* of horizontally aligned rigid particle pairs. The contrasting switching mechanisms were observed in the experiments and both sets of simulations.

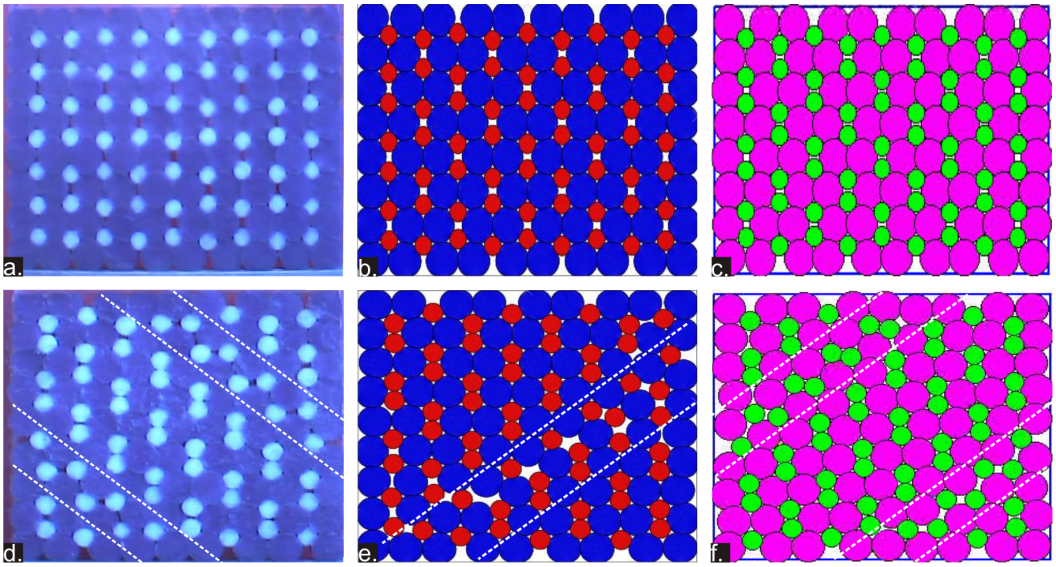

Figure 6.8: The granular crystals at $\epsilon = 0.15$ mm/mm. The representative images of the crystal with $\chi = 0.53$ (a - c) and $\chi = 0.61$ (d - f) show the structure in the experiments (left), FEM (middle) and MD (right) simulations.

6.4.1 Direct Transition

The formation of the rigid particle pairs where $\chi = 0.53$ occurred uniformly across the crystal. The initial effect of compression was to push the soft particles together into upright columns which were held apart by rigid particles. As the test continued the soft columns buckled in plane, forming hexagonally-packed clusters which enclosed two rigid particles. The vertical spacing between the rigid particles within each cluster decreased as the crystal was compressed further until the fully paired state was achieved at $\epsilon \approx 0.23$ mm/mm in the experiments. The gaps which in the crystal and led to the pattern-switched are visible in the experiments and simulations as shown in Figure 6.8 (a - c) respectively.

6.4.2 Indirect Transition

In contrast to the simple pair formation described above, the creation of the paired state where $\chi = 0.61$ crystal occurred via an intermediate "mixed state". This consisted of vertically aligned pairs and localised shear bands which stretched diagonally across the sample. Particles within the shear bands formed loosely packed horizontally aligned pairs with particles within neighbouring columns. The bands were destroyed as the crystal was compressed further. This resulted in the formation of vertically aligned pairs arranged according to the pattern already established within the bulk of the crystal.

The shear bands observed in the experiment are highlighted in Figure 6.8 (d) by the white dashed lines. Two shear bands formed during this experiment and each of these stretched diagonally downwards from left to right. Destruction of the bands occurred simultaneously, with the right most particle in each pair dropping down one row to become the top particle in a vertical pair. Shear bands were consistently observed to form in this structure, although their location, size and orientation varied in each experimental run.

As demonstrated in images (e) and (f) in Figure 6.8, shear bands were also a feature of the simulations and again these have been highlighted by the dashed white lines. In the FEM simulation (Figure 6.8 (e)) only one band formed, whereas two formed in the MD crystal (Figure 6.8 (f)). These bands were destroyed in coordinated switching events as in the experiments. The similarities between images of the experimental and MD crystals in the $\epsilon = 0.15$ mm/mm strain state is remarkable: in both systems the bands are short and form in the corners of the sample. As discussed in Section 6.3.2 the result of the destruction of the shear bands in the numerical crystals led to local phenomena as opposed to global pattern-switching.

However, the mechanisms within the systems are the same and the final state within each comprises mainly vertical pairs.

6.4.3 Unloading

Cyclic experiments were performed on the samples in order to test the reversibility of the pattern switch. Example images of the unloaded crystals are shown in Figure 6.9. There is a clear contrast between the two systems; in the $\chi = 0.53$ crystal the original geometry has been recovered which indicates that the transitition is almost reversible, as shown in Figure 6.9 (a - c) where in each of the images the crystals are shown in the relaxed state with $\epsilon = 0.00$ mm/mm. In contrast to this, where $\chi = 0.61$ (Figure 6.9 (d - f)), a shear band has re-formed in the crystal during the unloading process and the majority of soft columns have retained a hexagonally packed form as opposed to becoming upright. The formation of shear bands in the system is therefore an irreversible feature of the transition which prevents recovery to its original form. Once more, the simulations capture the experimental observations: the crystal with $\chi = 0.53$ undergoes a reversible depairing process as shown in Figure 6.9 (a - c), whereas the crystal with $\chi = 0.61$ does not return to the initial geometry and this is true for both simulation types.

6.5 Quantitative Measures

6.5.1 Particle Tracking

As discussed in the previous sections, a 15% increase in χ had a marked effect on the pattern formation process. In the systems with the lower χ value, the transition was direct and nearly reversible; an increase in χ caused the formation of shear bands which reappeared in the relaxed system. These qualitative differences were

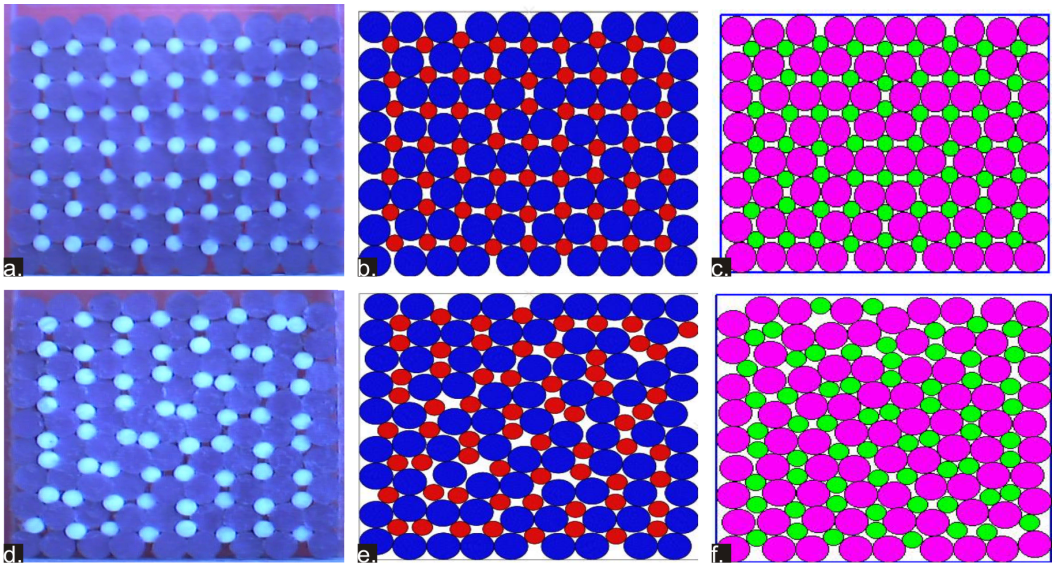

Figure 6.9: The granular crystals in their relaxed states. Reversibility was a feature of the experiments and simulations of the crystal $\chi = 0.53$ (a - c). However, this was not the case for the system where $\chi = 0.61$ (d - f) as shear bands were observed to re-form.

demonstrated in the experiments by considering local variation in the inter-particle distances $D^j_{i,i+1}$. Specifically, the distance ratio $\delta^j_{i-1,i,i+1}$ was calculated for specific rigid particle triplets. This is defined as

$$\delta^j_{i-1,i,i+1} = \begin{cases} \frac{D^j_{i,i+1}}{D^j_{i-1,i}} & \text{if } D^j_{i,i+1} \leq D^j_{i,i-1} \\ \frac{D^j_{i,i-1}}{D^j_{i+1,i}} & \text{if } D^j_{i,i+1} \geq D^j_{i,i-1} \end{cases}$$

in order to provide a measure of the relative growth of the distance of a particle in row i from the particles above and below it. Where $\delta^j_{i-1,i,i+1}$ was constant with ϵ, the central particle in the triplet was equidistant from its nearest neighbours in the column. Where $\delta^j_{i-1,i,i+1}$ decreased with ϵ, the central particle was closer to one particle than the other within the triplet and in the initial square configuration, $\delta^j_{i-1,i,i+1} \approx 1$. It was possible to predict the value of δ when each of the granular crystals is in the pattern-switched state. Assuming non-compression of the soft cylinders and that they formed a regular hexagon of side $2R$ in the pattern-switched state, δ_{final} was predicted to be

$$\delta_{final} = \frac{\chi}{2\cos\left(\frac{\pi}{6}\right) - \chi} \tag{6.6}$$

and for the size ratios considered here $\delta_{final} \approx 0.44$ ($\chi = 0.53$) and 0.54 ($\chi = 0.61$).

In Figure 6.10 the variation of δ with ϵ has been plotted for each of the size ratios considered in the study. The data set can be split up into a loading and unloading phase and these are indicated by the arrows on the plots. In both of the graphs in Figure 6.10, two remote triplets have been chosen in order to demonstrate the global/local nature of the switching processes observed in the experiments. The inset images show the location of the particles in each triplet at

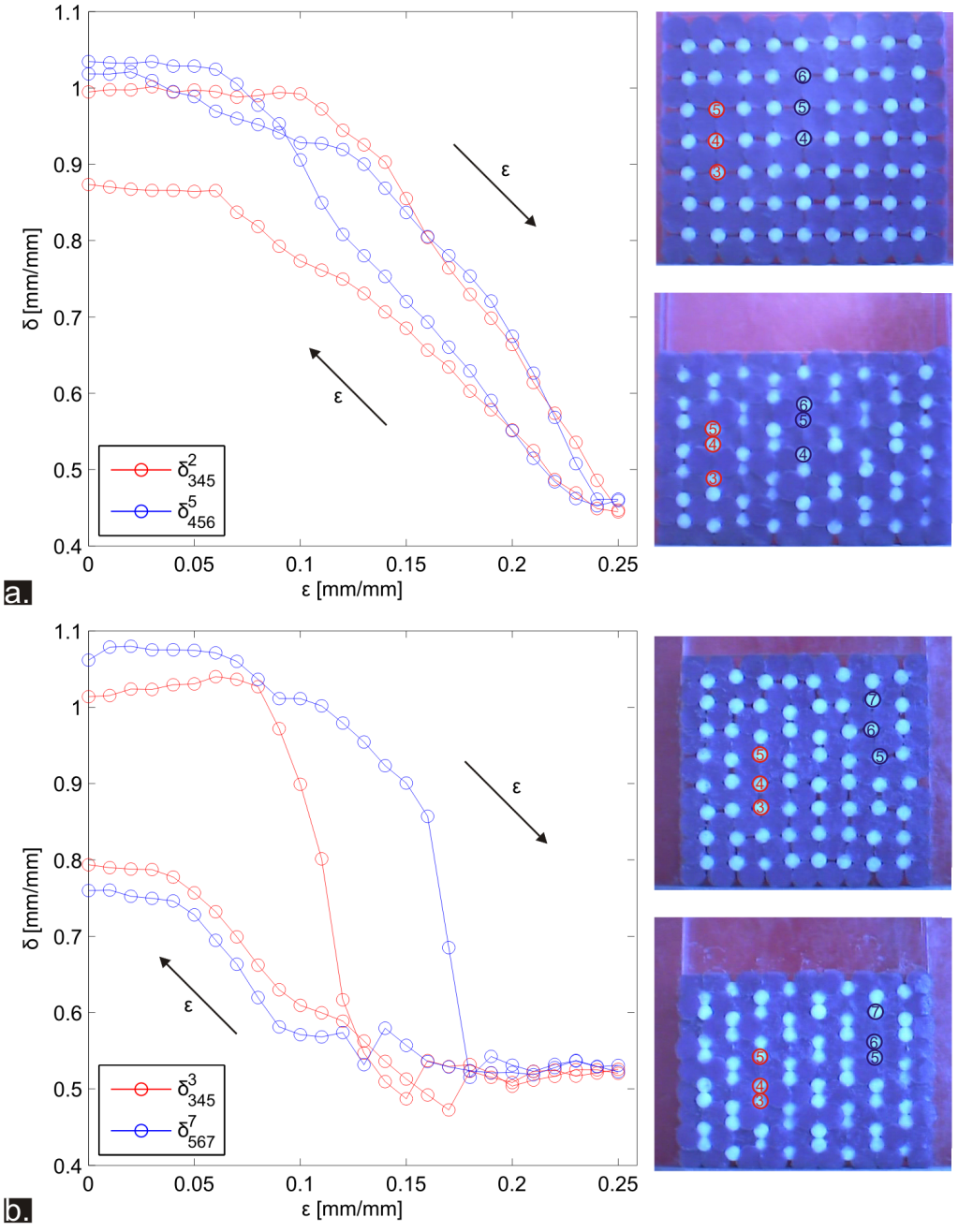

Figure 6.10: The variation of δ. In (a) it is shown that the variation of two local δ values is uniform across the $\chi = 0.53$ crystal. The formation of shear bands in the $\chi = 0.61$ crystal causes local pair formation which is reflected in the contrasting variation of the two δ values shown in (b).

$\epsilon = 0.00$ mm/mm (top) and 0.25 mm/mm (bottom) and the number in the centre of each highlighted particle is its row number i in the initial configuration.

In the upper-most graph (Figure 6.10 (a)), $\delta^2_{3,4,5}$ (red) and $\delta^5_{4,5,6}$ (blue) have been plotted for the crystal with $\chi = 0.53$. Both of the data sets show the same behaviour throughout the experiment. The central particles in each triplet are initially equidistant from their nearest neighbours above and below. At $\epsilon \approx 0.12$ mm/mm both δ values begin to decrease steadily. At $\epsilon \approx 0.23$ mm/mm the crystal is in the fully paired state and $\delta^2_{3,4,5} \approx \delta^5_{4,5,6} \approx 0.45$ at this point. During relaxation of the crystal, both δ values increase as the cylinders in each pair begin to separate. However, whilst $\delta^5_{4,5,6}$ returns to approximately its original value, $\delta^2_{3,4,5} \approx 0.88$ in the fully relaxed state. Permanent local deformation has therefore occurred such that the central particle in the triplet in column 2 is closer to the particle above than below it in the relaxed state.

In Figure 6.10 (b) $\delta^3_{4,5,6}$ (red) and $\delta^7_{5,6,7}$ (blue) have been plotted for the $\chi = 0.61$ crystal and there is a clear contrast between these data sets. A sharp reduction in $\delta^3_{4,5,6}$ is observed at $\epsilon \approx 0.11$ mm/mm. This resulted from particles 4 and 5 forming a local vertical pair in column 3. In constrast, $\delta^7_{5,6,7}$ decreases steadily until $\epsilon \approx 0.18$ mm/mm where it drops asymptotically. After this point ($\epsilon = 0.18$ mm/mm) the crystal is in the fully paired state ($\delta^3_{4,5,6} \approx \delta^7_{5,6,7} \approx 0.50$) and the two data sets agree during the remainder of the loading and the beginning of the unloading phases. The effect of unloading is to cause slight inter-particle separation but neither δ measure reaches its initial value and the initial configuration is not attained upon full relaxation of the sample.

The contrast between the two data sets shown in Figure 6.10 (b) is caused by

the competing processes in the crystal. Specifically, particles 5 and 6 in column 7 occupied a shear band and were held in position until its eventual destruction. This meant that $\delta^7_{5,6,7}$ was greater than $\delta^3_{4,5,6}$ until $\epsilon = 0.18$ mm/mm in the loading cycle. The other triplet (particles 4, 5 and 6 in column 3) became split up in a direct process similar to that observed in the crystal with $\chi = 0.53$. The increase in size ratio therefore led to a pattern-switching mechanism which retained enough order such that the final state was achieved despite the complexity observed in the experiments.

6.5.2 Stress-Strain Data

The stress-strain data measured during experiments on the granular crystals (black) has been plotted alongside the results of the MD (red) and FEM (green) simulations in Figure 6.11. The arrows above and below the data sets indicate the data taken in the loading (increasing ϵ) and unloading (decreasing ϵ) phases of each plot. There is good qualitative agreement between the experimental and numerical approaches, particularly in the loading compression phase. During this phase the FEM simulations are in better accord with the experiments than the MD approach: the former data set shows an average discrepancy of 20 % for each crystal size ratio, where as for the latter this is approximately 30 %.

During the unloading phase, the experimental data sets were approximately 50% lower than during the loading phase, a hysteresis effect which came about as a result of contact between housing and the soft particles which expanded out of plane when compressed. This hysteresis was not captured in the MD or FEM simulations as the calculations were made assuming plane strain in a 2D planar system so that the three-dimensional aspects of the experiments were not included. As such there is no quantitative agreement during this phase of the cycle. Plastic

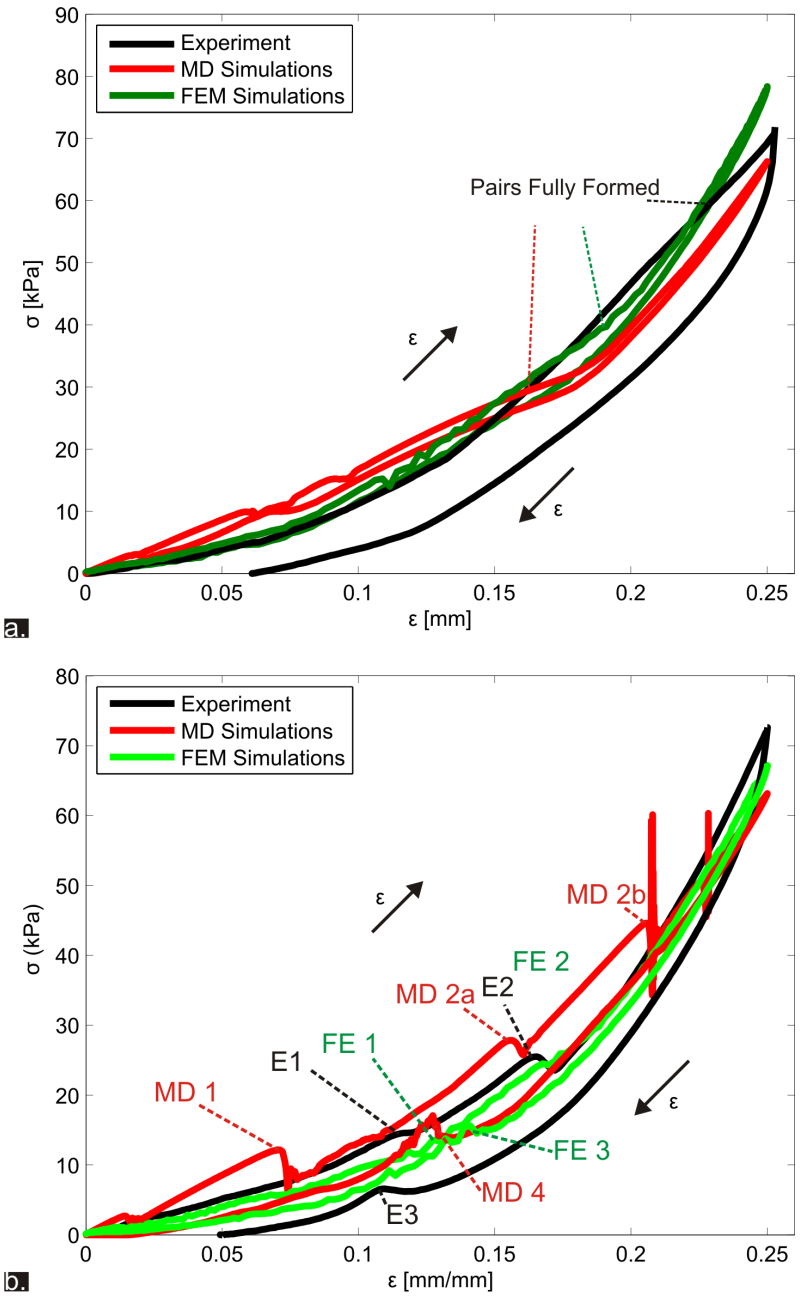

Figure 6.11: Stress-strain data for the granular crystals. This has been plotted for experiments (black) the MD (red) and FEM (green) simulations respectively for the $\chi = 0.53$ (a) and 0.61 (b) granular crystals. The local peaks identified in (b) correspond to the formation and destruction of shear bands in both the loading and unloading phases of each data set.

deformation was also observed in the experiments but not in the simulations and can be seen in the plots in Figure 6.11. The height of both structures was reduced by approximately 5 % by the end of the experiment.

The data shown in Figure 6.11 (a) was taken where $\chi = 0.53$ and reflected the gradual formation of the vertical pairs within the crystal plane. There are no notable peaks in the data sets and the buckling of the columns does not occur instantaneously as in the csa-lattices. The attainment of the fully paired state of the crystal occurred at $\epsilon \approx 0.17$ mm/mm and 0.19 mm/mm in the MD and FEM simulations respectively, the result of which was an increased stiffness of the crystal owing to increased rigid-rigid particle contacts. In the experiments, the fully switched state was achieved at $\epsilon \approx 0.23$ mm/mm and no change in the stress-strain behaviour was detected at this point.

Each of the $\chi = 0.61$ crystal data sets (Figure 6.11 (b)) were characterised by localised peaks in both the loading and unloading phases. These have been highlighted in the plot and were associated with the formation (E1) and destruction (E2) of the shear bands in the loading phase and the reformation of bands on unloading (E3). Both in the experiments and the simulations these switching events involved the coordinated rearrangement of the particles over short time scales and manifested themselves as stress drops across the surface of the crystal. It was noted that in the MD simulations two shear bands formed and were destroyed in separate events (MD2a. and MD2b.) respectively, whereas in the experiment documented here, two such bands were destroyed simultaneously. As can be observed in the data sets in Figure 6.11 (b), the ϵ values at which the bands formed and were destroyed varied for the different approaches and this was true for repeated experiments. Despite the quantitative discrepancy between the

approaches, there are qualitative details which are encouraging. In particular, the large scale rearrangement in the $\chi = 0.61$ crystal can be identified by the local peaks in the loading and unloading phases of the system in both the simulations and the experiments.

6.6 Summary

It has been shown that the 2D granular crystal, which comprises a mixture of soft and rigid cylindrical particles arranged on a square lattice, undergoes a period-doubling pattern switch when uniaxially compressed. The transition from the initial configuration to the paired state depends on the particle size ratio χ, although the final state is robustly achieved. For $\chi = 0.53$ the transition was observed to be direct and near-reversible whereas an increase in χ to 0.61 caused it to occur via an intermediate state. This comprised shear bands of horizontally aligned particle pairs, whose presence caused the initial state not to be recovered on unloading. One remarkable aspect of the experiments is the observation that the final state has been robustly achieved in crystals with both of the χ values studied here despite their contrasting size ratios leading to two contrasting deformation processes.

Some features of the stress-strain curves collected and the deformation processes observed in the experiments have been well captured by MD and FEM simulations. Although the pattern switch was not achieved globally in the numerical experiments where $\chi = 0.61$, the predominant observations of the physical experiments have been captured by the simulations, i. e. the majority of the rigid particles formed pairs. The quantitative discrepancy between the stress-strain data sets suggests that the forcing between the particles has not been completely represented in the calculations and it may be that friction between the particles and the

housing, which is one aspect of the experiments which is difficult to characterise in the simulations plays an important role in the deformation process. This has led to discrepancies in the quantitative output of the numerics in comparison with the experiments. However, it appears that this does not affect the pattern-switching phenomenon which is repeatable and shows sensitivity to the arrangement of the constituent parts of the crystal.

Chapter 7

Summary and Outlook

The results of a study of compression of two-phase elastic structures has been presented. In total, five systems - the csa-, ssa-, dsa- and cubic lattices and the granular crystal - have been considered. Whilst these possessed a range of geometries, the underlying theme of the study has been the exploration of pattern-switching behaviour using simple experiments.

7.1 Discussion of the Experiments

The csa-lattice was the main focus of the study and its behaviour under uniaxial loading conditions allows a close comparison with the end-load Euler-Bernoulli column. The primary equilibrium state of this structure comprises two types of behaviour under compression. In the first the voids are compressed homogeneously and in the second a global pattern of orthogonal ellipses forms, which is the pattern-switching behaviour observed by Mullin et al [2, 26]. The critical point at which the transition between these two phases occurred was determined by monitoring the aspect ratio γ of the voids. This measure decreased linearly in the initial loading phase and then according to a square root dependence in the

second loading phase. This behaviour represents the continuous stable branch of a perturbed pitchfork bifurcation. The second branch of the perturbed bifurcation has also been shown to exist and in this state the pattern differed by a rotation of the ellipses by 90^o. This state was terminated at its lower end by a saddle node bifurcation and only exists beyond a certain level of compression.

The critical parameters ϵ_{cr} and $\frac{\sigma_{cr}}{E_s}$, as well as the normalised elastic modulus $\frac{E}{E_s}$ have been measured for the csa-lattice. These have been used to aid comparison with established results for 2D cellular structures [3]. In Chapter 4 the measures were shown to vary according to scaling laws in $(\Phi_{max} - \Phi)^n$ and these were similar to those associated with stretching-dominated structures. The void fraction Φ is therefore the principle factor in determining the strength, stability and stiffness of the csa-lattice although the experimental samples exhibited size effects which affected the scaling laws. In particular, ϵ_{cr} and $\frac{\sigma_{cr}}{E_s}$ decreased as the number of rows n the lattice was increased. The effect of the boundaries as the sample height increased was to delay the onset of the pattern-switching instability and hence $\frac{\sigma_{cr}}{E_s}$ increased as well. Using the discrete model it has been shown that these effects can be reproduced using beam theory in a discrete model formalism. However, development in the nodal stiffnesses and boundary conditions is required before accurate quantitative with the experiments can be made.

The experiments discussed in Chapter 4 have shown that the pattern-switching effects are not confined to the csa-lattice. The dsa-lattice showed the same pattern-switching behaviour, whereas the ssa-lattice did not. A conclusion which may be drawn is that the non-uniform width of the inter-void ligaments is central to onset of the pattern switch. The ssa-lattice buckled laterally when compressed, causing the voids to be sheared to the side; in both the csa- and dsa-lattices behaviour

similar to a pitchfork bifurcation was observed. By incorporating non-uniform ligament widths into the structure in a regular manner, the buckling phenomenon results in a new global planar pattern. As discussed in Chapter 1, this behaviour is not typically observed in oblique and hexagonal lattices, in which the struts are thin and not curved. The dsa-lattice has the geometry of the hinged models which are used to explain the auxetic effect and here we have shown that it is possible to achieve this switching effect in a cellular structure and, moreover, that it results from an elastic instability. In our system there are no hinges, simply straight-edged cells and this is sufficient for the rotation mechanism to work.

In Chapter 5 the research was extended to three-dimensional cellular structures. The cubic lattices can be considered as comprising two super-imposed csa-lattice geometries and the results showed that the two-dimensional planar instability dominates the first buckling mode of these structures. When the holes were made to be the same size, imperfections caused one of the planes to buckle before the other. When incorporated in the 3D geometry of the cubic lattice the instability onset is unaffected by the second orthogonal set of voids. Decreased porosity of these systems does, however, reduce the stress values associated with compression. Therefore, the additional void set is a means for reducing the load required to cause the buckling instability onset in a 2D system without affecting the pattern itself.

The granular crystal experiments demonstrated the existence of pattern switching effects in structures with other, perhaps more complex, planar geometries. The system is sensitive to the size ratio of the constituent particles, however the period-doubled patern switch is robust and is also found in the MD and FEM simulations. The formation of the pattern-switched state in the granular crystal is a striking

result given the discrete nature of the particles - the gaps which arise in the system form a strikingly periodic pattern which is simimlar to that of the csa- and dsa-lattice and this is despite the lack of connectivity between the particles. In addition, in the system with the large χ value the pattern became established in the experiments despite there being an additional intermediate state of shear bands. Once more, the square lattice is a feature of the system - this geometry eases the motion of the rigid particles as they form the pairs with their nearest neighbours.

7.2 Future Work

There is great potential for using the experimental approach described in this thesis to explore the behaviour of cellular structures. In the first instance, a deeper understanding of the geometry of pattern switching systems is required. What is the link, for example, between the csa- and dsa- lattices? Moreover, why do square cells not show the same switching behaviour? These are open questions which require a comprehensive answer.

A particularly exciting study would be an analysis of the transition between two contrasting cellular geometries and the effect this has on the buckling instability therein. There are two obvious candidates for this. The first is the transition from the square to the oblique array of circular cells (i.e. from the csa- to the c*o*a-lattice). It is known that the former buckles at a lower degree of compression than the latter for the same void size and this is because of the increased connectivity in the system. The contrasting connectivities are linked to the pattern formation and lead to localised effects in the coa-lattice. What happens in-between is unclear. It would be possible to manufacture lattices in which there is a step-wise

change in the cellular arrangement from the csa- to the coa-lattice geometry and it is envisaged that localised regions of patterns would tend to develop. The second area in this theme is the transition from the ssa- to the dsa- lattice geometry. We have seen that a rotation of 45^o of square cells about their centres is sufficient to create a pattern-switching lattice. Once more, the dsa-lattice buckles at a lower degree of compression for the same void fration. An ineresting study would be to determine the tolerance of this: is there a pattern-switching range of rotation angles, and if so, why?

There is also an ambiguity in the role played by imperfections in the 2D cellular structures considered here. As has been discussed in Chapters 1, 3 and 5, there are imperfections in the cellular structures and these determine the form of the pattern-switched state. The imperfections fall into two categories, those which are unavoidable (bubbles which form in the material as it sets, for example) and those which are controllable, such as cell size variation. One can envisage performing experiments in which, for example, the voids in the csa-lattice are shifted locally or where there is a size or aspect ratio distribution. The effect of this may be global switching effects which occur more smoothly than described in the experiments here, or indeed localised effects where the pattern onset is observed in some, but not all, of the voids. Alternatively, imperfections may cause new pattern-switched states to emerge as a result of compression.

The above suggestions could certainly be implemented experimentally using the techniques used here. What would add a satisfying completeness to this would be the implementation of a numerical approach to the studies and this is being developed [80]. A numerical approach would also allow the investigation of the birfurcation structure of the csa-lattice. Throughout this study, we have described

the pattern switch as similar to the perturbed pitchfork bifurcation because of its similarities in terms of the stable states which exist. This is, of course, an oversimplified picture: the bifurcation structure of the csa-lattice is certainly richer than this and this has been shown by Bertoldi et al [26]. There exists a wide range of buckling modes for the structure, however it is unclear whether these are stable or attainable in experiments. This is where the experiments reach their limitation and further investigation must be performed numerically. As we have highlighted there are similarities between the dsa- and csa-lattice geometries and so there may exist new patterns in diamond-shaped cells as well, and these require exploration.

Appendix A

Negative Poisson's Ratio

A.1 Introduction

In the following pages of the appendix the paper "Negative Poisson's Ratio induced by Elastic Instability" has been reproduced. The paper documents the work completed in the first year of the PhD programme and the work is relevant to understanding the current state of research into regular 2D cellular solids. The experimental work which is contained in the paper was conducted by the author of this thesis. The cellular structure was manufactured using a different mould to that described in Appendix B. Part of the development made during the time since the paper's publication has been to refine the cellular structure manufacturing techniques to enable the study of a wide parameter range. However, the majority of the principles and techniques used in the thesis originated as part of this initial study which is a testament to the appeal of simple, careful scientific experiments.

ADVANCED MATERIALS

Negative Poisson's Ratio Behavior Induced by an Elastic Instability

By *Katia Bertoldi,* Pedro M. Reis, Stephen Willshaw,* and *Tom Mullin*

When materials are compressed along a particular axis they are most commonly observed to expand in directions orthogonal to the applied load. The property that characterizes this behavior is the Poisson's ratio, which is defined as the ratio between the negative transverse and longitudinal strains. The majority of materials are characterized by a positive Poisson's ratio, which is approximately 0.5 for rubber and 0.3 for glass and steel. Materials with a negative Poisson's ratio will contract (expand) in the transverse direction when compressed (stretched) and, although they can exist in principle, demonstration of practical examples is relatively recent. Discovery and development of materials with negative Poisson's ratio, also called auxetics, was first reported in the seminal work of Lakes in 1987.[1]

There is significant interest in the development of auxetic materials because of tremendous potential in applications in areas such as the design of novel fasteners,[2] prostheses,[3] piezocomposites with optimal performance[4] and foams with superior damping and acoustic properties.[5] The results of many investigations[6,7] suggest that the auxetic behavior involves an interplay between the microstructure of the material and its deformation. Examples of this are provided by the discovery that metals with a cubic lattice,[8] natural layered ceramics,[9] ferroelectric polycrystalline ceramics,[10] and zeolites[11] may all exhibit negative Poisson's ratio behavior. Moreover, several geometries and mechanisms have been proposed to achieve negative values for the Poisson's ratio, including foams with reentrant structures,[1] hierarchical laminates,[12] polymeric and metallic foams,[13] microporous polymers,[14] molecular networks,[15] and many-body systems with isotropic pair interactions.[16] Negative Poisson's ratio effects have also been demonstrated at the micrometer scale using complex materials which were fabricated using soft lithography[17] and at the nanoscale with sheets assemblies of carbon nanotubes.[18]

[*] Dr. K. Bertoldi
Multiscale Mechanics, University of Twente
PO Box 217, 7500 AE Enschede (The Netherlands)
E-mail: K.Bertoldi@ctw.utwente.nl
Dr. P. M. Reis
Department of Mathematics, #2-335
Massachusetts Institute of Technology
77 Massachusetts Avenue, Cambridge, MA 02139-4307 (USA)
S. Willshaw, Prof. T. Mullin
Department of Physics & Astronomy, University of Manchester
Manchester, M13 9PL (UK)

DOI: 10.1002/adma.200901956

A significant challenge in the fabrication of materials with auxetic properties is that it usually involves embedding structures with intricate geometries within a host matrix. As such, the manufacturing process has been a bottleneck in the practical development towards applications. A structure which forms the basis of many auxetic materials is that of a cellular solid and research into the deformation these materials is a relatively mature field[19] with primary emphasis on the role of buckling phenomena on load carrying capacity and energy absorption under compressive loading. Very recently, the results of a combined experimental and numerical investigation demonstrated that mechanical instabilities in 2D periodic porous structures can trigger dramatic transformations of the original geometry.[20,21] Specifically, uniaxial loading of a square array of circular holes in an elastomeric matrix is found to lead to a pattern of alternating mutually orthogonal ellipses. This results from an elastic instability above a critical value of the applied strain. The geometric reorganization observed at the instability is both reversible and repeatable and it occurs over a narrow range of the applied load. Thus, this behavior provides opportunities for transformative materials with properties that can be reversibly switched. Similar instability induced pattern transformations have been observed also at the sub-micrometer scale.[22,23] These observations pave the way for the development of a new class of materials which take advantage of such behavior.

Here we exploit elastic instabilities to create novel effects within materials with periodic microstructure. We show that the pattern transformation leads to unidirectional negative Poisson's ratio behavior for the 2D structure, i.e., it only occurs under compression. The uncomplicated manufacturing process of the samples together with the robustness of the observed phenomena suggests that this may form the basis of a practical method for constructing planar auxetic materials over a wide range of length-scales. Excellent quantitative agreement is found between numerical and experimental results to illustrate the effect for a specific sample. The numerical approach is subsequently used to explore the effect of void fraction and we uncover a scaling law for the phenomenon. Finally, we draw some conclusions and give future perspectives for this simple yet novel auxetic material.

Our system comprised a square lattice of circular holes in an elastomeric matrix which was subjected to uniaxial compression using an Instron machine as described in the Experimental Section. A representative sequence of images of the sample during loading is presented in Figure 1, where the image shown in Figure 1a corresponds to the undeformed sample, prior to loading. During the initial response of the periodic structure, the circular holes were observed to undergo a gradual and homogeneous compression and this corresponds to a linearly

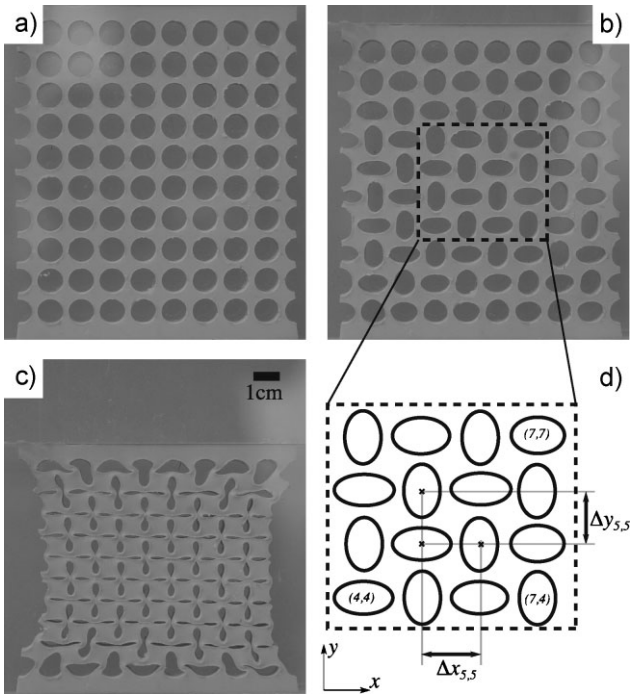

Figure 1. a) Sample in the initial unstrained configuration; b) Sample under compression of $\varepsilon = -0.06$. The dashed rectangle represents 16-hole region over which we perform the ensemble averaging. c) Sample under compression of $\varepsilon = -0.25$. d) Schematic diagram of the central region with 16 holes. The position of the centroids of the holes is measured from image analysis which allows for the determination of the vertical and horizontal center-to-center distance between two consecutive holes.

elastic regime at low strains.[20] As will be discussed in detail below, above a critical value of compressive nominal strain of $\varepsilon_c = -0.047$ a transformation to a pattern of alternating, mutually orthogonal ellipses was observed and an example of the resulting pattern switch is shown in Figure 1b where the image was taken at $\varepsilon = -0.06$ nominal strain. Once formed, the new pattern became further accentuated with increasing macroscopic compressive strain as may be seen in the image shown in Figure 1c taken at $\varepsilon = -0.25$ nominal strain. A feature, which is clear in Figure 1c, is that the lateral boundaries of the sample bend inwards, a clear signature of negative Poisson ratio behavior.

The experiments were performed on a silicone rubber cellular solid, which was manufactured using the molding process described in the Experimental section. The deformation of the sample was monitored using a high-resolution digital camera (6 MPixels Nikon D100 SLR), which was synchronized with the Instron. Quantitative estimates of the deformation of the holes in the sample were made using purpose made image processing software. In outline, at a particular value of nominal strain, the $(x_{i,j},y_{i,j})$ coordinates of the centroid of each void were determined where $1 < i < 10$ and $1 < j < 10$ are the row and column indices, respectively. Hence a particular index pair (i,j) is unique to each specific hole. This part of the procedure was accomplished using an edge detection algorithm (Matlab: Image Processing Toolbox), which takes advantage of the high contrast between the bulk regions in the sample and the voids. It became clear that the deformation near the four edges of the specimen was strongly influenced by the boundary conditions and hence, we focused on the behavior of the central part of the sample where the response was clearly more uniform. Thus we tracked the centroids of the sixteen central voids (delimited by the dashed rectangle in Figure 1b for holes with indices $4 \le i \le 7$ and $4 \le j \le 7$). The horizontal and vertical controid-to-centroid distances were calculated from the coordinates $(x_{i,j},y_{i,j})$, i.e., $\Delta x_{i,j} = x_{i+1,j} - x_{i,j}$ and $\Delta y_{i,j} = y_{i,j+1} - y_{i,j}$, respectively. Prior to compression, the value for both of these quantities was the center-to-center distance between the undeformed circular holes, i.e., $\Delta x(0) = \Delta y(0) = 11.95$ mm. A schematic diagram of the central region under consideration illustrating the definitions of $\Delta x_{i,j}$ and $\Delta y_{i,j}$ is shown in Figure 1d.

Numerical investigations were performed on both finite-sized and periodic domains using the nonlinear finite element code ABAQUS. Details of the method are provided elsewhere[21] and here we highlight some of the parts of the numerical procedure which are specific to the current investigation. Each mesh was constructed using six-node, quadratic, hybrid, plane strain elements (ABAQUS element type CPE6H) and the accuracy was checked by mesh refinement. The material was modeled using a two-term I1-based Rivlin model, which was modified to include compressibility with a high bulk modulus[21] where the material properties were determined by fitting the model to experimental calibration data (see Experimental section). The instabilities were initially investigated using a linear perturbation procedure and the results confirmed that the observed pattern transformation arose from an elastic instability, since it corresponds to the lowest eigenmode of the structure. An imperfection was introduced into the mesh in the form of this eigenmode, which enabled load–displacement analysis for the finite-sized structures. This procedure captured the instability induced pattern transformation and boundary effects were included so that direct comparison could be made with experiment. Calculations were also performed on infinite periodic structures and were used primarily for parametric investigations of the phenomena since carrying out a similar experimental study would have been impractical.

In Figure 2a we present the functional dependence of both $\langle \Delta x_{i,j} \rangle / \Delta x(0)$ and $\langle \Delta y_{i,j} \rangle / \Delta y(0)$ on nominal strain, where the angular brackets $\langle . \rangle$ denote ensemble average over the sixteen holes (hence, nine values of $\Delta x_{i,j}$ and $\Delta y_{i,j}$) under consideration ($4 \le i < 7$ and $4 \le j < 7$). The experimental data points are shown in comparison with the numerically determined solid lines and it can be seen that there is close agreement between the sets of results. The normalized vertical centroid-to-centroid distance shows a monotonic decrease from one (undeformed case) to approximately 0.85 at a strain of $\varepsilon = -0.1$. On the other hand, the horizontal centroid-to-centroid distance exhibits a non-monotonic dependence on nominal strain. It first increases during the initial linear elastic response of the periodic structures and, once the pattern switch occurs ($\varepsilon = -0.047$), it decreases.

The center-to-center distances of the holes were used to calculate local values of the engineering strain Poisson's ratio using

$$\nu_{i,j} = -\frac{\Delta x_{i,j}/\Delta x(0)}{\Delta y_{i,j}/\Delta y(0)}. \quad (1)$$

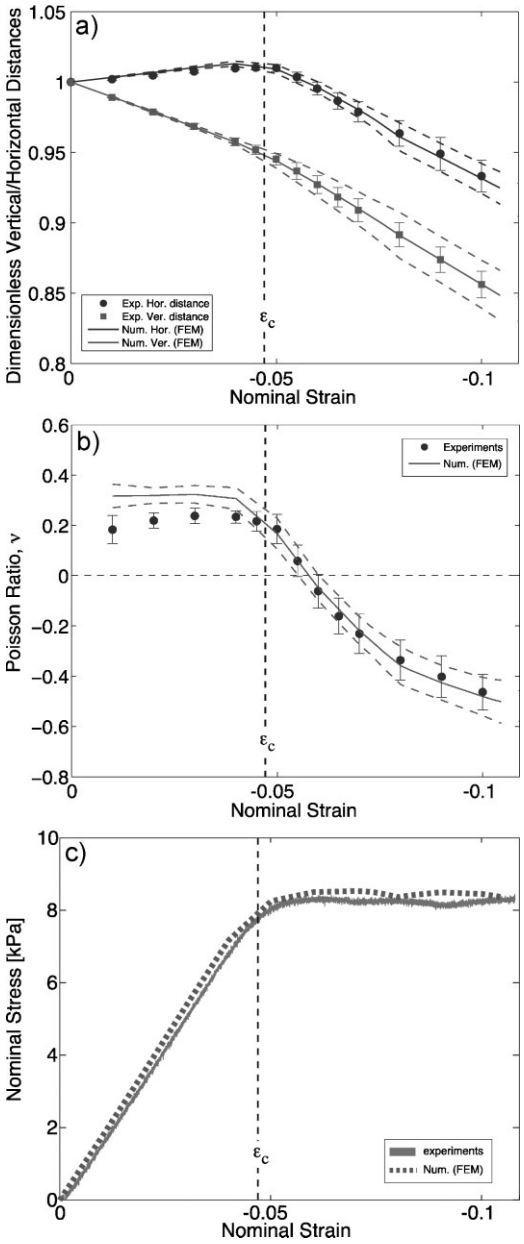

Figure 2. Quantitative comparison between experimental and numerical results. a) Averaged dimensionless horizontal and vertical distances of central 16 holes plotted as a function of the applied axial nominal strain b) Poisson's ratio as a function of the applied axial nominal strain and c) Stress-strain response of the experimental sample (solid line) and results from the finite element calculations (dashed line). In (a) and (b), points correspond to experimental data and lines to the results of the finite element calculations. The solid and dashed lines correspond to the ensemble average and standard deviation, respectively, of the 16 central holes considered (see text for details).

The ensemble average $\nu = \langle \nu_{i,j} \rangle$ for the sixteen central voids under consideration was computed. The experimental and numerical estimates of ν are plotted as a function of nominal strain in Figure 2b where the error bars on the experimental points were obtained from the standard deviation of the nine values of $\nu_{i,j}$ used in the averaging. When $\varepsilon < -0.047$, the response of the sample is linear as in the stress strain plot in Figure 2c. Over this range of strain, the numerically determined estimate of the Poisson's ratio is approximately constant at $\nu = 0.284 \pm 0.014$. The experimental data on the other hand lies consistently below the numerical results at a value of $\nu = 0.221 \pm 0.021$ and shows a slight increase. Over this range of strain, the deformation of the holes is very small and, hence, so are $\Delta x_{i,j}$ and $\Delta y_{i,j}$. Therefore, accurate measurements are difficult to make, since small unavoidable alignment errors between the sample and the camera will dominate.

It can be seen in Figure 2c that a plateau emerges in the stress-strain curve for strains in excess of $\varepsilon_c = -0.047$, i.e., the total stress becomes independent of strain. This type of response is generic for cellular solids under compression[19] and the initial periodic structure is recovered upon removal of the strain so that the change is reversible and repeatable. The strain $\varepsilon_c = -0.047$ corresponds to the critical strain at which the pattern transformation occurs and we have indicated this by a vertical line, which runs through all parts of Figure 2. The Poisson's ratio starts to decrease above this point and eventually becomes negative for strains in excess of $\varepsilon = -0.053 \pm 0.003$. Interestingly, the agreement between the experimental and numerical results for estimates of the Poisson's ratio, shown in Figure 2b, improves considerably once the pattern transformation occurs and there is an obvious distortion of the holes, as shown in Figure 1b. This excellent agreement between the two sets of results can be seen for further increase in strain and the minimum value of the Poisson's ratio found in the experiments was $\nu = -0.538$ for $\varepsilon = -0.10$. Beyond this value, the top and bottom edge of some voids touched and determination of the position of the centroids was problematic, although further contraction in the transverse direction is evident as shown in Figure 1c.

The results reported thus far are for a particular value of the void fraction, $\Phi = 0.5$, where Φ is defined as the ratio of the total area of voids divided by the surface area of the sample. The finite element simulations are able to accurately reproduce the experimental results and we now perform numerical investigations of the dependence of the auxetic properties on Φ. The pattern switch, which underpins the auxetic behavior occurs throughout the sample and is only marginally influenced by the boundaries. Moreover, practical applications are likely to involve samples of a large spatial extent. Consideration of both of these points, directed our focus to considering infinite periodic structures using representative volume elements (RVEs) and numerically convenient periodic boundary conditions.[21] Two different types of instability may occur[21] in infinite periodic solids under compression: microscopic instabilities with a finite wavelength and macroscopic instabilities characterized by a wavelength much larger than the scale of the microstructure. Although microscopic instabilities alter the original periodicity of the solid, here they are investigated on the primitive cell using Bloch wave analysis,[21] which provides both the point on loading path where instability occurs and the periodicity of the new structure. Macroscopic instability is also detected by monitoring the loss of ellipticity of the homogenized tangent modulus.[21]

Both microscopic and macroscopic instabilities were investigated and the effect of the void volume fraction on the response

Final page numbers not assigned

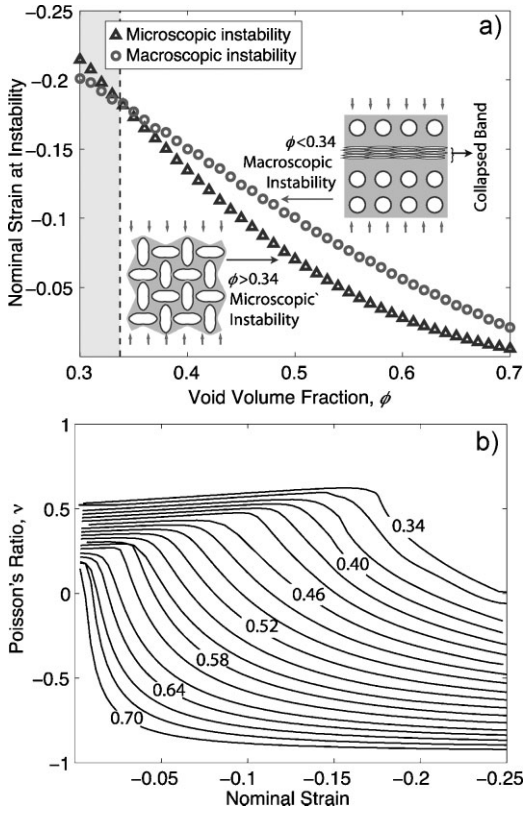

Figure 3. Results of the numerical investigation on the effect of the void volume fraction for an infinite periodic square array of circular holes in an elastomeric matrix. a) Nominal strain at the onset instability as a function of the void volume fraction. Inset schematics illustrate the instability type for $\Phi < 0.34$ (upper right: localization) and $\Phi > 0.34$ (lower left: pattern switch). b) Evolution of the Poisson's ratio as a function of applied axial nominal strain over the range of volume fraction investigated.

was studied. The results reported in Figure 3a show that for $\Phi < 0.34$, a macroscopic instability is the first to occur along the loading path. This leads to localized deformation in the form of a collapsed band of holes normal to the direction of the applied load as shown schematically in the top inset in Figure 3a. By way of contrast, a microscopic instability was found to occur first for $\Phi > 0.34$. Here the mode of deformation is characterized by a critical eigenmode consisting of mutually orthogonal ellipses as shown in the inset in the lower left hand corner of Figure 3a and consistent with the experiments. As for the finite-sized sample, load-displacement analysis was performed for the infinite periodic structures to capture the evolution of the Poisson's ratio during deformation. The Poisson's ratio was calculated directly from the numerical results on the RVEs using the homogenized strains in axial and lateral directions. As a check, it was also estimated from the images of the calculated patterns using the distance between the centers of the voids as in the experiments and negligible difference between the results obtained using the methods was found.

Results for the evolution of the Poisson's ratio as a function of the applied nominal strain are presented in Figure 3b for various values of void volume fraction and a strong dependency on this parameter is evident. For $\Phi < 0.34$ (where localization occurs prior to the pattern transformation) the Poisson's ratio is always positive during loading. On the other hand, samples with $\Phi > 0.34$ are characterized by behavior analogous to the experimental samples discussed above viz. positive Poisson's ratio up to a critical value of strain, ε_c, at which the instability induced pattern transformation occurs and beyond which the Poisson ratio decreases until it eventually becomes negative. It is interesting to note that the lowest value of the asymptotic Poisson's ratio we were able to reach numerically was $\nu_\infty = -0.904$, which occurs for the highest value of void fraction investigated $\Phi = 0.70$.

It is striking that simply by increasing the void fraction, samples can be constructed to attain increasingly negative values of ν in a pronounced way. In particular, the three quantities of interest – the value of strain at which the pattern transformation occurs, ε_c, the asymptotic value of the Poisson ratio and the rate at which this asymptotic value is reached are – all strongly depend on void fraction. We now explore the dependence of these quantities on void fraction in detail. In Figure 4a we show the

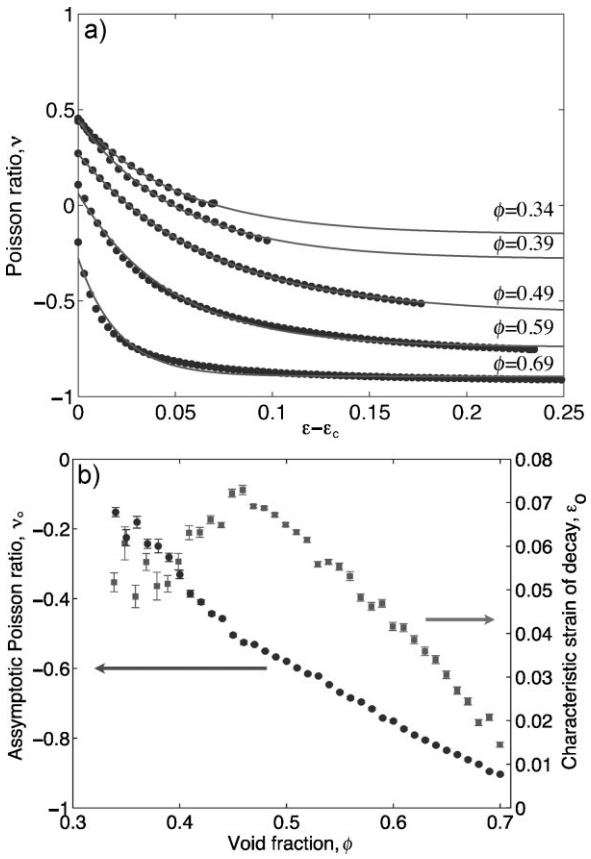

Figure 4. RVE simulations. a) Dependence of the Poisson's ratio on $\varepsilon - \varepsilon_c$ (nominal strain above the instability), where ε_c was obtained from the Bloch analysis (plotted in Fig. 3a). The circles correspond to the RVE simulations and the red lines are exponentials. Each set of curves for different void fraction (0.34, 0.39, 0.49, 0.59, 0.69). b) Parameters obtained from the exponential fit as a function of void fraction: circles (left vertical axis) for the asymptotic value of Poisson's ratio, ν_∞, and squares (right vertical axis) for strain rate decay, ε_o. The lines are exponentials obtained from fitting the experimental data to Equation 2.

Poisson's ratio dependence on $\varepsilon - \varepsilon_c$ for a range of void fractions. We see that the results from the RVE simulations (circles) can be accurately fitted (solid lines) by exponentials of the form

$$\nu = \nu_\infty + (\nu_c - \nu_\infty) \exp\left[-\frac{\varepsilon - \varepsilon_c}{\varepsilon_o}\right] \quad (2)$$

where, ν_∞, is the asymptotic Poisson's ratio, ν_c is the Poisson's ratio at the onset of the instability which occurs at a nominal strain, ε_c, and the characteristic strain of decay, ε_o, measures the speed the asymptotic value is reached.

The exponential fits are particularly good when $\Phi < 0.56$. Small deviations are observed for $\Phi > 0.56$ but the exponential dependence of Equation 2 is nonetheless a satisfactory way to describe the data from the RVE simulations. In Figure 4b, we plot the dependence of the fitting parameters ν_∞ and ε_o on void fraction and the error bars were obtained from the statistical errors in the fitting procedure. The asymptotic value of the Poisson's ratio, ν_∞, is negative for all void fractions when $\Phi > 0.34$, i.e., where there was an instability induced pattern transformation. Moreover, ν_∞ exhibits a monotonic decrease with two approximately linear regimes separated by a kink at $\Phi \sim 0.46$. On the other hand, the characteristic strain of decay, ε_o, first increases to a maximum at $\Phi \sim 0.46$, beyond which it decays. This is significant of a larger rate of decay ($1/\varepsilon_o$) of ν for high void fractions. These results suggest that in order to maximize auxetic properties, samples should be manufactured with the largest possible void fraction.

We have shown that a cellular solid which comprises a solid matrix with a square array of voids displays two-dimensional negative Poisson's ratio behavior. Unlike many other examples of auxetic materials the effect is only found under compression and above a critical value of an applied strain. The behavior arises as a result of a pattern transformation, which has recently found application at the micrometer scale in phononic/photonic crystals.[24–26] The insight gained by performing a numerical parametric exploration serves as an important design guideline in fabricating practical materials towards applications. The overriding features of the system we have explored are the simplicity of the construction and the robustness of the behavior. Each of these aspects points to a more practical method for producing negative Poisson's ratio material, which can operate over a wide range of scales.

Experimental

Material: Experiments were performed on samples made from the addition curing silicone rubber ''Sil AD Spezial'' (SADS), manufactured by ''Feguramed GmbH''. The manufacture involved mixing equal measures of two fluids, placing the individual component fluids under vacuum to remove dissolved gases and allowing the mixture to set for an hour to ensure proper curing.

Uniaxial compression and tension stress–strain tests were conducted to characterize the behavior of the bulk material by measuring stress/strain relationships for specifically designed solid blocks using a standard Instron apparatus with a 1 kN load cell. We found that the elastomeric stress-strain behavior is well captured using an incompressible two-term I1-based Rivlin model [21], so that the nominal stress is given by

$$s = \left(\lambda - \frac{1}{\lambda^2}\right)\left[\mu + 4c\left(\lambda^2 + \frac{2}{\lambda} - 3\right)\right] \quad (3)$$

where μ is the initial shear modulus and λ denotes the applied stretch, $\lambda = \varepsilon + 1$. The required material parameters were found by fitting Equation 3 to the experimental data obtained from the calibration tests. A Young's modulus of 470.8 ± 1.6 kPa was determined so that $\mu = 156.9 \pm 0.5$ kPa and using $c = 20.1 \pm 0.4$ kPa the material behavior was found to be well captured up to a nominal strain of 0.6 both in tension and in compression.

Rectangular Sample Manufacture: A batch of SADS mixture was poured into an aluminum mould measuring 130 mm × 130 mm × 7.9 mm. Machined brass pins of diameter 10 mm were screwed into the base of the mould to create a square array of 100 holes with a center to center spacing of 12.0 mm. The mold was coated with a thin layer of vaseline to help prevent sticking of the rubber to the metal. The mould was sealed and the mixture was allowed to set at atmospheric pressure and room temperature. The sample was removed from the mould after one hour and two of the side walls were cut from the sample, leaving eight columns of ten holes, flanked by a column of ten semi circles on either side. It was found that a small amount of shrinkage had taken place. The rectangular sample used in the experiments measured 128.7 mm × 107.0 mm × 7.9 mm, with a hole diameter of 9.95 ± 0.02 mm. Sample dimensions were measured using digital calipers.

Compression Experiments: Compression tests were performed using an ''Instron 5569'' machine with a 1 kN load cell. The sample was held vertically between two 8.1 mm thick PMMA sheets which were held 9.4 mm apart in the machined slots on a metal base. The sample faces were dusted with flour to reduce any frictional effects resulting from buckling during the loading process. A PMMA sheet of thickness 8.1 mm was mounted on the lower face of the load cell and used to apply the load to the top of the sample. It was ensured that the three PMMA sheets were parallel to one another, and that the bottom of the loader was parallel to the top of the sample. This allowed the even loading of the sample and prevented the loader touching the outer faces of the housing.

The compression tests were performed by lowering the loader to rest on to the top surface of the sample. The loader was then lowered further, at a rate of approximately 0.01667 mm s^{-1}, to a final displacement of 30 mm. The results were independent of the rate of change of displacement for slower speeds and hence a good approximation to the rate independent conditions of the numerical investigation was obtained in the experiments. The load associated with the displacement was recorded once per every 100 ms and used to produce a stress-strain curve for the compression process.

Acknowledgements

S.W. and T.M. are grateful to S. Morse and J. Fonseca of the School of Materials at The University of Manchester for use of their Instron and helpful discussions. K.B. and T.M. are grateful to S. Luding for the helpful discussions and traveling support.

Received: June 10, 2009
Published online:

[1] R. S. Lakes, *Science* **1987**, *235*, 1038.
[2] J. B. Choi, R. S. Lakes, *Cell. Polym.* **1991**, *10*, 205.
[3] F. Scarpa, *IEEE Sig. Proc. Mag.* **2008**, *25*, 128.
[4] O. Sigmund, S. Torquato, I. A. Aksay, *J. Mater. Res.* **1998**, *13*, 1038.
[5] F. Scarpa, L. Ciffo, J. Yates, *Smart Mater. Struct.* **2004**, *13*, 49.
[6] K. E. Evans, A. Alderson, *Adv. Mater.* **2000**, *12*, 617.

[7] R. S. Lakes, *J. Mater. Sci.* **1991**, *26*, 2287.
[8] R. H. Baughman, J. M. Shacklette, A. A. Zakhidov, S. Stafstrom, *Nature* **1998**, *392*, 362.
[9] F. Song, J. Zhou, X. Xu, Y. Xu, Y. Bai, *Phys. Rev. Lett.* **2008**, *100*, 245502.
[10] X. Tan, W. Jo, T. Granzow, J. Frederick, E. Aulbach, J. Rödel, *Appl. Phys. Lett.* **2009**, *94*, 042909.
[11] J. N. Grima, R. Jackson, A. Alderson, K. E. Evans, *Adv. Mater.* **2000**, *12*, 1912.
[12] G. Milton, *J. Mech. Phys. Solids* **1992**, *40*, 1105.
[13] E. A. Friis, R. S. Lakes, J. B. Park, *J. Mater. Sci.* **1988**, *23*, 4406.
[14] B. D. Caddock, K. E. Evans, *J. Phys. D* **1989**, *22*, 1877.
[15] K. E. Evans, M. K. Nkansah, I. J. Hutchison, S. C. Rogers, *Nature* **1991**, *353*, 124.
[16] M. C. Rechtsman, F. H. Stillinger, S. Torquato, *Phys. Rev. Lett.* **2008**, *101*, 085501.
[17] B. Xu, F. Arias, S. T. Brittain, X. M. Zhao, B. Grzybowski, S. Torquato, G. M. Whitesides, *Adv. Mater.* **1999**, *11*, 1186.
[18] L. J. Hall, V. B. Coluci, D. S. Galvao, M. E. Kozlov, V. S. Zhang, O. Dantas, R. H. Baughman, *Science* **2008**, *320*, 504.
[19] L. J. Gibson, M. F. Ashby, *Cellular Solids: Structure and Properties*, Cambridge University Press, Cambridge **1999**.
[20] T. Mullin, S. Deschanel, K. Bertoldi, M. C. Boyce, *Phys. Rev. Lett.* **2007**, *99*, 084301.
[21] K. Bertoldi, M. C. Boyce, S. Deschanel, S. M. Prange, T. Mullin, *J. Mech. Phys. Solids* **2008**, *56*, 2642.
[22] Y. Zhang, E. A. Matsumoto, A. Peter, P. C. Lin, R. D. Kamien, S. Yang, *Nano Lett.* **2008**, *8*, 1192.
[23] J. H. Jang, C. Y. Koh, K. Bertoldi, M. C. Boyce, E. L. Thomas, *Nano Lett.* **2009**, *9*, 2113.
[24] S. Singamaneni, K. Bertoldi, S. Chang, J. Jang, E. L. Thomas, M. C. Boyce, V. V. Tsukruk, *ACS Appl. Mater. Interfaces* **2009**, *1*, 42.
[25] S. Singamaneni, K. Bertoldi, S. Chang, J. Jang, E. L. Thomas, M. C. Boyce, V. V. Tsukruk, *Adv. Funct. Mater.* **2009**, *19*, 1426.
[26] X. L. Zhu, Y. Zhang, D. Chandra, S. C. Cheng, J. M. Kikkawa, S. Yang, *Appl. Phys. Lett.* **2008**, *93*, 161911.

Appendix B

Sample Manufacture

B.1 Two-Dimensional Cellular Structures

The two-dimensional cellular structures considered in the thesis were manufactured by pouring the addition-curing fluid elastomers described in Chapter 2 into hand-constructed moulds. To make these, a grid of the desired structure was drawn using CorelDraw and inclusions were stuck to the printed grid using double-sided tape. An aluminium frame was stuck to the boundary of the grid to complete the mould. This process is described in detail for the csa-lattices in Section B.1.1. The relevant details for the ssa- and dsa-lattices are given in Section B.1.2.

B.1.1 Circular Cells

The circular cell matrices were manufactured by pouring the fluid elastomer mixture into hand-constructed moulds comprising cylindrical inclusions fixed to a printed grid. The inclusions had been cut from a sheet of the photoelastomer *PSM-4* [2, 25] using a water-jet and possessed diameter $d = 8.79 \pm 0.09$ mm and height $h = 6.66 \pm 0.07$ mm.

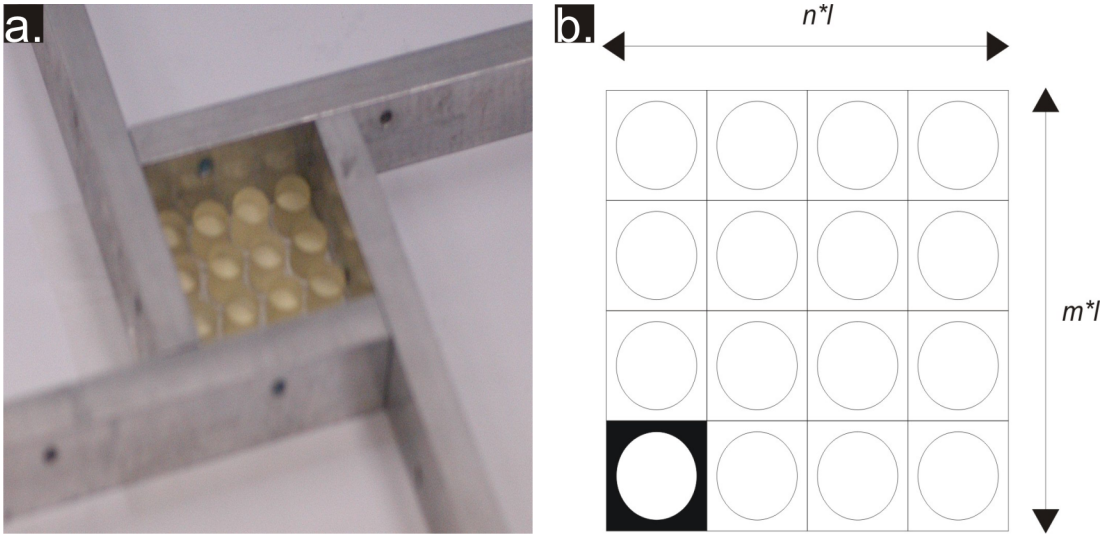

Figure B.1: The 2D mould. As shown in (a), aluminium walls formed the boundary. The inner dimensions of the mould were altered by changing the positions of the walls. Here, a 4×4 ($\Phi = 0.60$) lattice is being prepared for manufacture. The unit cell was created by concentrically positioning a circle of diameter d on to a square of side l. The unit cell is copied to form a grid of n columns of m unit cells (b). The overall dimensions of the grid are nl and ml respectively.

To create the mould, a unit cell of the desired circular cell matrix was drawn using the drawing software CorelDraw. The d value matched that of the cylindrical inclusions and l was calculated according to the desired void fraction. This unit cell was then copied and arranged into an $n \times m$ grid. An example of a printed grid is shown in Figure B.1.1 (b).

The inclusions were fixed to the printed circles in the grid using double-sided tape. Both the tape and the inclusions were transparent which aided this step of

the process. The mould was completed by fixing four aluminium walls (12.96 ± 0.02 mm × 130.04 ± 0.04 mm) to the perimeter of the grid as shown in Figure B.1.1 (a), in which the mould used to manufacture a 4 × 4 csa-lattice (0.60) has been assembled. By changing the position of the walls it was possible to create a boundary of flexible dimensions for the mould and therefore change the breadth and height of the square honeycomb made using it. The fluid was left to set in the mould for one hour, after which time the set structure was removed by detaching the walls, followed by the inclusions and the base of the mould. This last step was eased by applying a layer of Vaseline to the walls and inclusions at the outset of the moulding process.

The moulding procedure was devised because the focus of the experiments was the effect of geometry and size on the response of circular cell matrices to compression. The inclusion-based mould offered the flexibility required in order to do so, without having to rely on advanced moulding techniques. During the manufacturing process it was important to construct the mould and place the inclusions as accurately as possible; the hand-made aspect of the moulds reduced the accuracy of the positioning of the voids within the circular cell matrices in comparison with machined moulds. Whilst this is a prescient point, imperfections are ubiquitous in cellular structures made using automated and accurate techniques and sophisticated processes do not necessarily represent solution to this problem. The moulding technique used here was a simple, accessible method which enabled a variety of experimental samples to be made and was sufficient for the purposes of this study.

B.1.2 Square and Diamond Cells

The square and diamond cell lattices were made using the same technique as for the circular cell matrices. Instead of the cylindrical inclusions, cuboid inclusions were used to make the voids and this had to be considered when drawing the printed geometry.

B.2 Cubic Lattices

The cubic lattices were made using a similar method to the 2D experimental samples. The 3D geometry of these structures posed an additional problem which was overcome by building up the mould in layers.

B.2.1 (0.60 $\times$ 0.41) Cubic Lattice

The mould used to manufacture 0.60 $\times$ 0.41 cubic lattice is shown in Figure B.2a.The assembled system consisted of a cubic Perpex box (inner side $L = 69.4\pm$ 0.3 mm) which held four layers of interlocking PTFE rods. Each layer was made up of four small diameter (d_1 = 12.54 $\pm$ 0.03 mm) and four large diameter (d_2 =15.16 $\pm$ 0.07 mm) rods. Four holes which matched the diameter of the smaller rods had been machined into each of the large diameter rods with a spacing of 17.20$\pm$ 0.05 mm. The small rods slotted into these holes to create the platforms which were held in place by means of holes in the faces of the Perspex cube. These were arranged in a 4 $\times$ 4 square lattice with an inter-hole spacing of 17.20 $\pm$ 0.05 mm in each plane. In two opposite faces the voids accommodated the smaller PTFE rods, and the remaining two faces the large diameter rods.

The procedure for manufacturing the cubic lattices samples involved constructing the bottom PTFE platform within the mould and injecting Sil AD Soft into

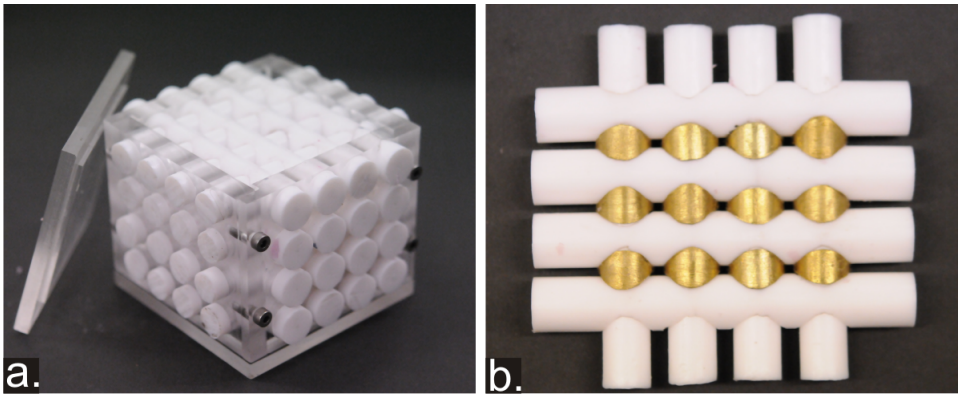

Figure B.2: The 3D mould. (a) The mould consisted of a Perspex box which holds four platforms of interlocking PTFE rods in place. The rods were of contrasting diameter which enabled construction of the platforms. Experimental samples were manufactured by injecting Sil AD Soft in to the gaps between the rods.It was required to equalise the diameter of the two rod sets which was achieved by slotting tapered copper rings onto the small diameter rods as shown in (b). These platforms were used within the mould to manufacture the (0.60 $\times$ 0.60) cubic lattice

the gaps between the rods. This was performed using a syringe to assist the flow of the fluid through small gaps in order to fill the mould. This process was repeated for each of the four layers in succession until the mould was full and the material was then allowed to set for one hour. The mould was dismantled by pushing the small diameter rods out from the mould, followed by the large diameter rods. The faces and base of the mould were then removed. As with the moulding procedure described in Section B.1.1 the components of the mould were initially covered in Vaseline to aid the dismantling process.

B.2.2 (0.60 $\times$ 0.60) Cubic Lattice

The procedure described above was sufficient to manufacture the (0.60 $\times$ 0.41) cubic lattice. A modification was required to equalise the diameters of the rods

in order to create the (0.60 × 0.60) cubic lattice sample. This was achieved by slotting 48 tapered copper rings (inner diameter 12.65 ± 0.17 mm, outer diameter 15.12 ± 0.20 mm) onto the small diameter rods and positioning them between the large diameter rods in each of the platforms. The rings were manufactured such that they matched the curvature of the small diameter rods and maintained the aforementioned inter-hole spacing of the platforms.

An image of a completed platform with the copper spacers in position is shown in Figure B.2b. The mould was constructed, filled and dismantled in the same way as described in Section B.2.1 when using the copper inserts. The copper rings remained within the set material upon removal of the rods and so these components were removed using tweezers at the end of the dismantling process.

B.3 Characterisation Samples

Samples of the bulk material were made every time a batch of the elastomeric material was prepared. This was performed by pouring some of the mixture into three cylindrical aluminium moulds (diameter 10.00 ± 0.05, height 10.03 ± 0.06 mm) and allowing it to set for the same time as the cellular structure which was being made. These rod-shaped *calibration samples* of bulk material were required in order to determine its elastic properties from compression tests. These are described in further detail in Section 2.1 of this thesis.

Appendix C

Discrete Model

A brief overview of the discrete model [56] used predict the buckling stress of two-dimensional cellular structures was given in Chapter 4. Here, this model is discussed in greater depth and this includes a full derivation of the spring constants and the critical stress. Whilst the discussion of the model is primarily focussed on the circular cell matrix, the formalism here can be applied to cells with square and diamond shapes. It is assumed that, whatever the cell shape, the cells are arranged on a square lattice.

The discrete model is constructed by replacing the square lattice of cells with a skeletal frame of crossed rigid rods of length l. The rods form rigid crosses where they overlap and meet at the thinnest part of the interstitial ligament within the lattice. Where two crosses meet, they are attached by means of a hinge equipped with a rotational spring. The stiffness of the springs is denoted ρ and in calculating this value the resistance of the inter-hole ligaments to buckling is concentrated to one point. The spring constants at the boundaries are half of those in the bulk of the structure as they are half the width at this point. As described in Chapter 4, the vertical springs at the top and bottom boundaries are stiffened by a factor $\frac{1}{k}$.

In order to replicate the experimental conditions, the stress σ which is applied uniformly across the top and bottom surfaces of the experimental sample must be discretised. This is performed such that the applied load acts locally on the top and bottom of the columns of rigid bars. It is assumed that this force F is constant on each column with the exception of the two outermost columns where $\frac{F}{2}$ is applied. The buckling of the discrete structure is manifested by the rotation of each of the rigid crosses about an angle α from the initial position ($\alpha = 0$). As observed in Chapter 4, the form taken by the discrete model in this state mimics accurately that of the csa-lattice in its buckled state.

C.1 Buckling

The buckling stress σ_{cr} of the lattice is calculated by considering the total energy $\Pi(\alpha)$ of the structure . The work done by the external compressive load on each of the inner $n-1$ columns is $Fml\cos\alpha$. On the two outermost columns it is $\frac{F}{2}ml\cos\alpha$ according to the discretisation of the force described in Section **??**. The total work done Π_w is

$$\Pi_w(\alpha) = Fnml\cos\alpha \tag{C.1}$$

When the crosses rotate by an angle α about their centres the rotational spring becomes compressed by 2α. Therefore the potential energy stored in each rotational spring is $\frac{\rho(2\alpha)^2}{2}$. Within the $n-1$ inner columns there are m vertical springs and for each of the $m-1$ inner rows there are n horizontally aligned rotational springs. As described in Section **??** the rotational stiffnesses at the boundary of the structure are halved and the vertical springs in the top and bottom rows become stiffened.

$\Pi_{rot}(\alpha)$ is the sum of the rotational energies

$$\Pi_{rot}(\alpha) = \Pi_h(\alpha) + \Pi_v(\alpha) \tag{C.2}$$

where $\Pi_h(\alpha)$ is the sum of the energy contributions from the initially horizontal springs

$$\begin{aligned} \Pi_h(\alpha) &= 2m\frac{\rho}{2}\frac{(2\alpha)^2}{2} + (n-1)\, m\rho\frac{(2\alpha)^2}{2} \\ &= nm\rho\frac{(2\alpha)^2}{2} \\ &= 2nm\rho\alpha^2 \end{aligned} \tag{C.3}$$

and $\Pi_v(\alpha)$ is the total energy contribution from the initially vertical springs

$$\begin{aligned} \Pi_v(\alpha) &= (n-1)(m-1)\rho\frac{(2\alpha)^2}{2} + 2(n-1)\frac{\rho}{2}\frac{(2\alpha)^2}{2} + \ldots \\ &\quad \frac{4\rho}{2k}\frac{(2\alpha)^2}{2} + 2(m-1)\frac{\rho}{k}\frac{(2\alpha)^2}{2} \\ &= m(n-1)\rho\frac{(2\alpha)^2}{2} + \frac{2m\rho}{k}\frac{(2\alpha)^2}{2} \\ &= 2m(n-2)\rho\alpha^2 + \frac{4m\rho\alpha^2}{k} \end{aligned} \tag{C.4}$$

Substituting equations (C.3) and (C.4) into equation (C.2) gives

$$\begin{aligned} \Pi_{rot}(\alpha) &= 2nm\rho\alpha^2 + 2m(n-2)\rho\alpha^2 + \frac{4m\rho\alpha^2}{k} \\ &= 4nm\alpha^2 + 4m\rho\alpha^2\left(\frac{1}{k} - 1\right) \end{aligned} \tag{C.5}$$

and the total energy $\Pi(\alpha)$ therefore has the form

$$\Pi(\alpha) = Flmn\cos\alpha + 4nm\alpha^2 + 4m\rho\alpha^2\left(\frac{1}{k} - 1\right) \tag{C.6}$$

where the only independent variable is the deflection angle α. In order to determine the load value F_{cr} at which the structure buckles, it is necessary to differentiate equation (C.6) with respect to α. The first derivative gives the equilibrium solutions and the second derivative determines the point at which an initially stable state will become unstable [4, 31]. This is found by considering the neutral stability condition, whereby the second differential is equated to 0 and using this it is possible to find F_{cr}. Differentiating equation (C.6) twice with respect to α yields

$$\frac{d^2\Pi(\alpha)}{d\alpha^2} = -Flmn\cos\alpha + 8mn\rho + 8m\rho\left(\frac{1}{k} - 1\right) \tag{C.7}$$

In order to determine the onset of instability of the structure in the trivial state α is set to 0 and equation (C.7) must meet the neutral stability condition described above. Applying these two conditions gives

$$\frac{d^2\Pi(\alpha)}{d\alpha^2}|_{\alpha=0} = -F_{cr}lmn + 8mn\rho + 8m\rho\left(\frac{1}{k} - 1\right) = 0 \tag{C.8}$$

where at the onset of instability $F = F_{cr}$. Rearranging equation (C.8) allows F_{cr} to be calculated

$$F_{cr} \quad = \quad \frac{8\rho}{l} + \frac{8\rho}{nl}\left(\frac{1}{k} - 1\right) \tag{C.9}$$

The final step in determining the critical stress of the structure is to convert F_{cr} from a force to a stress value. F_{cr} acts locally on the top and bottom surfaces of

the structure and so the total force on the surface is nF_{cr}. The area over which this acts is $A = nlw$ where w is the thickness of the sample. The normalised critical stress is calculated by dividing nF by A according to the definition of this measure given in Section 3.2.4 i.e.

$$\begin{aligned} \frac{\sigma_{cr}}{E_s} &= \frac{nF_{cr}}{nlw} \\ &= \frac{8\rho}{wE_s l^2}\left(1 + \frac{1}{kn} - \frac{1}{n}\right) \end{aligned} \tag{C.10}$$

In the above expression E_s and w can be set to unity as the spring constant ρ is shown in the following sections to be linear in these variables, giving .

$$\frac{\sigma_{cr}}{E_s} = \frac{8\rho}{l^2}\left(1 + \frac{1}{kn} - \frac{1}{n}\right) \tag{C.11}$$

C.2 Spring Constants

The equations derived in Section C.1 are generic and the cell shape has not been included in the derivations. In the following three sections ρ is derived for circular, square and diamond cells. The stiffness ρ is calculated by considering the inter-hole ligaments as single rods which are acted on by a bending moment M about its central axis. ρ is calculated such that the springs provide the same resistance to bending and hence the same angular deflection as the rod. From beam theory

$$I(x) = \frac{(2y(x))^3}{12} \tag{C.12}$$

where E_s the Youngs modulus of the material from which the rod is made and $2y(x)$ is its thickness of the rod at a distance x along its central axis. This is specific

to the shape of the cells and is given in the relevant sections. The curvature of the beam is

$$\kappa(x) = \frac{M}{E_s I(x)} \tag{C.13}$$

and the total angular deflection between two ends of the rod is

$$\theta = \int_{\frac{-l}{2}}^{\frac{l}{2}} \kappa(x) dx \tag{C.14}$$

By equating the angular deflection in the original structure (θ) and that in its discrete form (2α), and assuming that the bending moment M is the same in both cases, the following expression for the rotational stiffness ρ is obtained

$$\rho = E_s \left(\int_{\frac{-l}{2}}^{\frac{l}{2}} \frac{1}{I(x)} dx \right)^{-1} \tag{C.15}$$

C.2.1 Circular Cells

For ease of calculation of the tapered beam stiffness, the origin is located at the hinged point, the x-axis is oriented along the beams central axis and the y-axis is orthogonal to this. The thickness of the tapered rod at position x is described as

$$y(x) = \begin{cases} \frac{l}{2} - \frac{d}{2}\sqrt{1 - \frac{4x^2}{d^2}} & \text{if } 0 < |x| < \frac{d}{2} \\ \frac{l}{2} & \text{if } \frac{d}{2} < |x| < \frac{l}{2} \end{cases}$$

In performing the integral over x it is noted that the single tapered rod is symmetrical about the x-axis.

$$\begin{aligned}
\int_{\frac{-l}{2}}^{\frac{l}{2}} \frac{1}{I(x)}dx &= 2\int_{0}^{\frac{l}{2}} \frac{1}{I(x)}dx \\
&= 2\int_{0}^{\frac{d}{2}} \frac{1}{I(x)}dx + 2\int_{\frac{d}{2}}^{\frac{l}{2}} \frac{1}{I(x)}dx \\
&= 2\int_{0}^{\frac{d}{2}} \frac{12}{w(2y(x))^3}dx + 2\int_{\frac{d}{2}}^{\frac{l}{2}} \frac{12}{w(2y(x))^3}dx \\
&= \frac{24}{8w}\int_{0}^{\frac{d}{2}} \frac{1}{(\frac{l}{2} - \frac{d}{2}\sqrt{1-\frac{4x^2}{d^2}})^3}dx + \frac{24}{8w}\int_{\frac{d}{2}}^{\frac{l}{2}} \frac{1}{(\frac{l}{2})^3}dx \\
&= \frac{3}{w}\int_{0}^{\frac{d}{2}} \frac{1}{(\frac{l}{2} - \frac{d}{2}\sqrt{1-\frac{4x^2}{d^2}})^3}dx + \frac{3}{w}\int_{\frac{d}{2}}^{\frac{l}{2}} \frac{1}{(\frac{l}{2})^3}dx
\end{aligned} \tag{C.16}$$

In order to determine the first term in equation (C.16) the integrand $\xi = \frac{2x}{d}$ is introduced. The integral now takes the form

$$\int_{0}^{\frac{d}{2}} \frac{1}{(\frac{l}{2} - \frac{d}{2}\sqrt{1-4x^2})^3}dx = \frac{4}{d^2}\int_{0}^{1} \frac{d\xi}{(a - \sqrt{1-\xi^2})^3} \tag{C.17}$$

where $a = \frac{l}{d}$. The right hand side of equation (C.17) is expressed as $\frac{4}{d^2}\left[C(\xi)\right]_0^1$ where the term $C(\xi)$ has the form

$$C(\xi) = \frac{A^5}{2}\left(C_1(\xi) + \frac{\left[C_2(\xi) + \frac{\xi}{A}\left(C_3(\xi) + C_4(\xi) + C_5(\xi)\right)\right]}{C_6(\xi)}\right) \tag{C.18}$$

where

$$A = \frac{1}{\sqrt{a^2-1}} \tag{C.19a}$$

$$C_1(\xi) = 3a\tan^{-1}(A\xi) \tag{C.19b}$$

$$C_2(\xi) = 3a\left((a^2+\xi^2-1)^2\right)^2 \tan^{-1}\left(\frac{A\xi}{\sqrt{1-\xi^2}}\right) \tag{C.19c}$$

$$C_3(\xi) = 2a^5 + 3a^4\sqrt{1-\xi^2} \tag{C.19d}$$

$$C_4(\xi) = a^3 - a^2(1-\xi^2)^{\frac{3}{2}} \tag{C.19e}$$

$$C_5(\xi) = 3a(\xi^2-1) - 2(1-\xi^2)^{\frac{3}{2}} \tag{C.19f}$$

$$C_6(\xi) = \left(a^2+\xi^2-1\right)^2 \tag{C.19g}$$

It can be seen that $C(0) = 0$ and only $C(1)$ requires calculation in order to determine ρ. In this limit the equations (C.20) reduce to

$$C_1(1) = 3a\tan^{-1}(A)$$

$$C_2(1) = 3a^5\left(\frac{\pi}{2}\right)$$

$$C_3(1) = 2a^5$$

$$C_4(1) = a^3$$

$$C_5(1) = 0$$

$$C_6(1) = a^4$$

and so $C(1)$ has the form

$$C(1) = \frac{A^5}{2}\left(3a\left(\tan^{-1}(A) + \frac{\pi}{2}\right) + \frac{1}{A}\left(2a + \frac{1}{a}\right)\right) \tag{C.21}$$

The second term in equation (C.16) has the form

$$\int_{\frac{d}{2}}^{\frac{l}{2}} \frac{1}{(\frac{l}{2})^3} dx = \frac{4(l-d)}{l^3} \tag{C.22}$$

and the spring stiffness ρ is expressed as follows

$$\rho = \frac{E_s w}{12}\left(\frac{d^2}{C(1)+\frac{d^2(l-d)}{l^3}}\right) \tag{C.23}$$

C.2.2 Square Cells

The spring stiffness can be calculated for the square-celled lattice using equation (C.15). For the square cells of side a, $y(x)$ is given by

$$y(x) = \begin{cases} \frac{l-a}{2} & \text{if } 0 < |x| < \frac{a}{2} \\ \frac{l}{2} & \text{if } \frac{a}{2} < |x| < \frac{l}{2} \end{cases}$$

The integration over x in equation (C.15) can be split up in a similar manner to the circular cell case

$$\begin{aligned} \int_{\frac{-l}{2}}^{\frac{l}{2}} \frac{12}{w(2y(x))^3}dx &= 2\int_0^{\frac{l}{2}} \frac{12}{w(2y(x))^3}dx \\ &= 2\int_0^{\frac{a}{2}} \frac{12}{w(2y(x))^3}dx + 2\int_{\frac{a}{2}}^{\frac{l}{2}} \frac{12}{w(2y(x))^3}dx \\ &= 2\int_0^{\frac{a}{2}} \frac{12}{w(l-a)^3}dx + 2\int_{\frac{a}{2}}^{\frac{l}{2}} \frac{12}{wl^3}dx \\ &= \frac{12a}{w(l-a)^3} + \frac{12(l-a)}{wl^3} \\ &= \frac{12\left(al^3+(l-a)^4\right)}{w(l-a)^3l^3} \end{aligned} \tag{C.24}$$

The stiffness ρ is calculated using equation (C.15).

$$\begin{aligned}\rho &= E_s \left(\int_{\frac{-l}{2}}^{\frac{l}{2}} \frac{1}{I(x)} dx \right)^{-1} \\ &= \frac{E_s w (l-a)^3 l^3}{12\left(a l^3 + (l-a)^4\right)}\end{aligned} \tag{C.25}$$

C.2.3 Diamond Cells

For the case of diamond shaped cells with diagonal b, $y(x)$ has the form

$$y(x) = \begin{cases} \frac{l-b}{2} + |x| & \text{if } 0 < |x| < \frac{b}{2} \\ \frac{l}{2} & \text{if } \frac{b}{2} < |x| < \frac{l}{2} \end{cases}$$

Again, the spring constant can be calculated using equation (C.15).

$$\begin{aligned}\int_{\frac{-l}{2}}^{\frac{l}{2}} \frac{12}{w(2y(x))^3} dx &= 2\int_0^{\frac{l}{2}} \frac{12}{w(2y(x))^3} dx \\ &= 2\int_0^{\frac{b}{2}} \frac{12}{w(2y(x))^3} dx + 2\int_{\frac{b}{2}}^{\frac{l}{2}} \frac{12}{w(2y(x))^3} dx \\ &= 2\int_0^{\frac{b}{2}} \frac{12}{(w(l-b)+2x)^3} dx + 2\int_{\frac{b}{2}}^{\frac{l}{2}} \frac{12}{wl^3} dx \\ &= \frac{2}{-4}\left(\frac{12}{w(l-b+b)^2}\right) - \frac{2}{-4}\left(\frac{12}{w(l-b)^2}\right) + \frac{12(l-b)}{wl^3} \\ &= -\frac{12}{2wl^2} + \frac{12}{2w(l-b)^2} + \frac{12(l-b)}{wl^3} \\ &= \frac{6}{w}\left(\frac{-1}{l^2} + \frac{1}{(l-b)^2} + \frac{2(l-b)}{l^3}\right) \\ &= \frac{6}{w}\left(\frac{l^3 + 2(l-b)^3 - l(l-b)^2}{(l-b)^2 l^3}\right)\end{aligned} \tag{C.26}$$

Using equations (C.15) and (C.26) together it is found that

$$\begin{aligned}\rho &= E_s \left(\int_{\frac{-l}{2}}^{\frac{l}{2}} \frac{1}{I(x)} dx \right)^{-1} \\ &= \frac{w}{6} \left(\frac{E_s (l-b)^2 l^3}{l^3 + 2(l-b)^3 - l(l-b)^2} \right) \end{aligned} \tag{C.27}$$

C.2.4 Comparing Cell Shape

The variation of the ρ values calulated using equations (C.23), (C.25) and (C.27) for circular (blue), diamond (red) and square (green) voids has been plotted in Figure C.1. This confirms the experimental observation that the csa-lattice is the stiffer of the three types, however there is little difference between the dsa- and ssa-lattices.

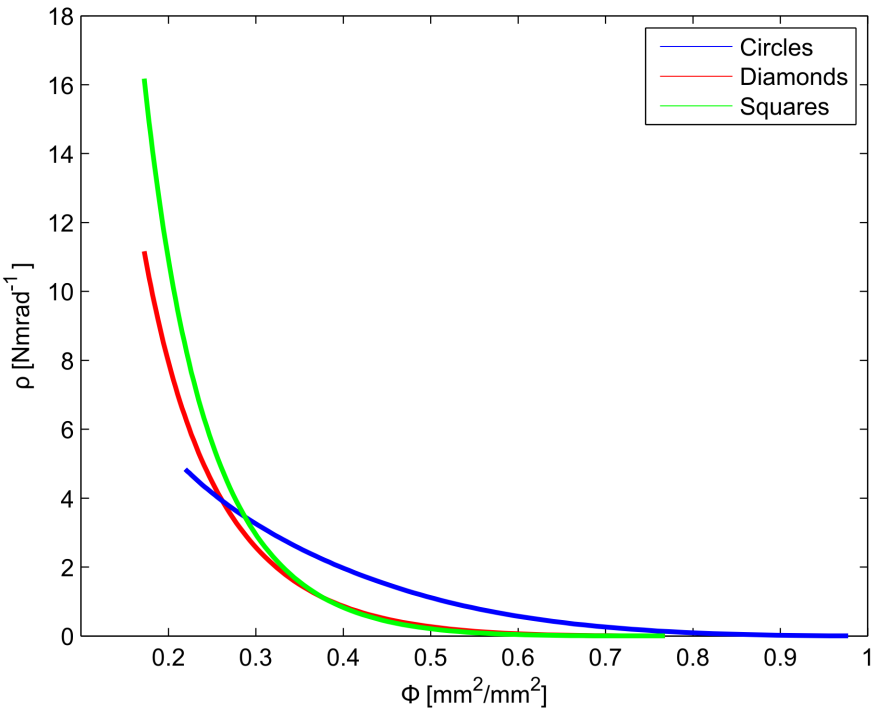

Figure C.1: The variation of ρ with Φ for the csa-(blue), dsa-(red) and ssa-(blue)lattices.

Bibliography

[1] V. S. Deshpande, M. F. Ashby, and N. A. Fleck. Foam topology: bending versus stretching dominated structures. *Acta. Mater.*, **49**, 2001.

[2] T. Mullin, S. Deschanel, K. Bertoldi, and M. C. Boyce. Pattern transformation triggered by deformation. *Phys. Rev. Lett.*, **99**, 2007.

[3] L. J. Gibson and M.F Ashby. *Cellular Solids, Structure and Properties*. Cambridge University Press, 1997.

[4] S. Strogatz. *Nonlinear Dyamics and Choas*. Perseus Books, 1994.

[5] S. Papka and S. Kyriakides. Experiments and full-scale numerical simulations of in-plane crushing of a honeycomb. *Acta. Mater.*, **46**:2765–2776, 1998.

[6] K. Bertoldi, P. M. Reis, S. Willshaw, and T. Mullin. Negative Poisson's ratio behavior induced by an elastic instability. *Adv. Mat.*, **22**:361–367, 2010.

[7] K. Zhang, H.L. Duan, B.L. Karihaloo, and J.X. Jianxiang. Hierarchical multilayered cell walls reinforced by recycled silk cocoons enhance the structural integrity . *Proc. Nat. Acad. Sci. USA*, **107**, 2010.

[8] C.W.W. Pirk, H.R. Hepburn, S.E. Radloff, and J. Tautz. Honeybee combs: construction through a liquid equilibrium process? *Naturwissenschaften*, **91**, 2004.

[9] S. C. Pratt. Gravity independent orientation of honeycomb cells. *Naturwissenschaften*, **87**, 2000.

[10] Q. Zhou and R. R. Mayer. Characterization of aluminium honeycomb failure in large deformation compression, shear and tearing. *J. Eng. Mater. Technol.*, **124**, 2002.

[11] C. Chen, T.J. Lu, and N.A. Fleck. Effect of inclusions and holes on the stiffness and strength of honeycombs. *Int. J. Mech. Sci.*, **43**, 2001.

[12] C. Chen, T.J. Lu, and N.A. Fleck. Effect of imperfections on the yielding of two-dimensional foams. *J. Mech. Phys. Sol.*, **47**, 1999.

[13] S. Papka and S. Kyriakides. Biaxial crushing of honeycombs - part 1:experiments. *Int. J. Mech. Sol. Struc.*, **436**:4367–4396, 1999.

[14] T. C. Hales. The honeycomb conjecture. *Disc. Comp. Geometry*, **25**, 2001.

[15] L. Monette and M. P. Anderson. Elastic and fracture properties of the two dimensional triangular and square lattices. *Modelling Simul. Mter. Sci. Eng.*, **2**, 1994.

[16] G. J. McShane D. D. Radford, V. S. Deshpande, and N.A. Fleck. Dynamic compressive response of stainless steel square honeycombs. *Trans. ASME*, **74**, 2007.

[17] N. Ohno, D. Okumura, and Niikawa T. Long-wave buckling of elastic square honeycomb subject to in-plane biaxial compression. *Int. J. Mech. Sci.*, **46**:1697–1713, 2004.

[18] A. J. Wang, R. S. Kumar, and D. L. McDowell. Mechanical behaviour of extruded prismatic cellular metals. *Mech. Adv. Mater. Struct.*, **12**, 2005.

[19] J. Michel et al. Microscopic and macroscopic instabilities in finitely strained porous elastomers. *J. Mech. Phys. Sol.*, **55**:900–938, 2007.

[20] R. G. Hutchinson, N. Wicks, A. G. Evans, N. A. Fleck, and J. W. Hutchinson. Kagome plate structures for actuation. *Int. J. Sol. Struct.*, **40**, 2003.

[21] D. D. Symons and N. A. Fleck. The imperfection sensitivity of isotropic two-dimensional elastic lattices. *J. App. Mech.*, **75**, 2008.

[22] N. Triantafyllidis, M.D. Nestorovic, and M.W. Schraad. Failure surfaces for finitely strained two-phase periodic solids under general in-plane loading. *J. App. Mech.*, **73**:505–515, 2006.

[23] M. F. Ashby. The properties of foams and lattices. *Phil. Trans. Roy. Soc. A*, **364**, 2006.

[24] J. Maxwell. On the calculation of the equilibrium and stiffness of frames. *Philosophical Mag.*, 1864.

[25] T. Mullin, I. Zuriguel, and R. Arevalo. Stress dip under a two-dimensional semipile of grains. *Phy. Rev. E*, **77**, 2008.

[26] K. Bertoldi, M.C. Boyce, S. Deschanel, S.M. Prange, and T. Mullin. Mechanics of deformation-triggered pattern transformations and superelastic behavior in periodic elastomeric structures. *J. Mech. Phys. Sol.*, **56**:2642–2668, 2008.

[27] W. E. Warren and A. M. Kraynik. Foam mechanics: the linear elastic response of two-dimensional spatially periodic cellular structures. *Mech. Mater.*, **6**, 1987.

[28] R. von Mises. The critical external pressure of cylindrical tubes. *J. Ass. Ger. Eng.*, **58**, 1914.

[29] T. Mullin. *The Nature of Chaos.* Oxford, 1993.

[30] R.W. Ogden. *Non-Linear elastic deformations.* Wiley, 1984.

[31] P. G. Drazin. *Nonlinear Systems.* Cambridge University Press, 1992.

[32] E. A. Matsumoto and R. D. Kamien. Elastic-instability triggered pattern formation. *Phys. Rev. E*, **80**, 2009.

[33] C. Kittel. *Introduction to Solid State Physics - Eighth Edition.* Wiley, 2005.

[34] H. X. Zhu and N. J. Mills. The in-plane nonlinear compression of regular honeycombs. *Int. J. Sol. Struct.*, **37**:1931–1949, 2000.

[35] J. Chung and A. M. Waas. Compressive response of circular cell polycarbonate honeycombs under in-plane biaxial static and dynamic loading. *Int. J. Imp. Eng.*, **27**, 2002.

[36] S. Singamaneni, K. Bertoldi, S Chang, J. Jang, S. L. Young, E. L. Thomas, M. C. Boyce, and V. V. Tsukurk. Bifurcated mechanical behaviour of deformed periodic porous solids. *Adv. Func. Mat.*, **19**:1426–1436, 2000.

[37] L. L. Hu, T. X. Yu, Z. Y. Gao, and X. Q. Huang. The inhomogeneous deformation of polycarbonate circular honeycombs under in-plane compression. *Int. J. Mech. Sci*, **50**, 2008.

[38] Y. Zhang, E. A. Matsumotu, A. Peter, P.C. Lin, R. D. Kamien, and S. Yang. One-step nanoscale assembly of complex structures via harnessing of elastic instability. *Nano Letters*, **8**:1192–1196, 2008.

[39] S. Singamaneni and V.V. Tsukruk. Buckling instabilities in periodic composite polymeric materials. *Soft Matter*, **6**:5681–5692, 2010.

[40] K. Bertoldi and M.C. Boyce. Wave propagation and instabilities in monolithic and periodically structured elastomeric materials undergoing large deformations. *Phys. Rev. B*, **78**, 2008.

[41] X. Shu, Y. Zhang, D. Chandra, S. Cheng, J. M. Kikkawa, and S. Yang. Two-dimensional photonic crystals with anisotropic unit cells imprinted from poly(dimethylsiloxane) membrance under elastic deformation. *App. Phys. Lett.*, **93**, 2008.

[42] G. Gallot and J. B. Masson. Coupling between surface plasmons in subwavelength hole arrays. *Phys. Rev. B*, **73**, 2006.

[43] S. Singamaneni, K. Bertoldi, S. Chang, J. Jang, S. L. Young, E. L. Thomas, M. C. Boyce, and V. V. Tsukurk. Instabilities and pattern transformation in periodic, porous elastomeric solid coatings. *App. Mater. Interfaces*, **1**, 2009.

[44] Y. Zhang, J.C. Reed, and S. Yang. Creating a library of complex metallic nanostructures via harnessing pattern transformation of a single PDMS membrane. *ACS Nano* , **3**:2412–2418, 2009.

[45] A. Alderson and K. Alderson. Auxetic Materials. *J. Aero. Eng.*, **221**, 2007.

[46] R. S. Lakes. Foam structures with a negative Poisson's ratio. *Science*, **235**:1038–1040, 1987.

[47] L.J. Gibson, K.E. Eastering, and M.F. Ashby. The structure and mechanics of cork. *Proc. Roy. Soc. A.*, **377**:99–117, 1981.

[48] D. Attard and J. N. Grima. Auxetic behaviour from rotating rhombi. *Phys. Stat. Sol. B.*, **245**:2395–2404, 2008.

[49] J.N. Grima, A. Alderson, and K.E. Evans. Auxetic behvaiour from rotating rigid units. *Phys. Stat. Sol. (b).*, **242**:561–575, 2005.

[50] M.C. Boyce, D.M. Parks, and A.S. Argon. Large inelastic deformation of glassy polymers, part 1: rate dependent constitutive model. *Mech. Mater.*, **7**:15–33, 1988.

[51] C. M. Roland. Mechanical behaviour of rubber at high strain rates. *J. Chem. Rub* , **79**:429–459, 2006.

[52] M. Boyce. Lecture Notes in Nonlinear Elasticity. *MIT Lecture Course*, 2006.

[53] H. Kurzwell and B. Stellmacher. *The Theory of Finite Groups: An Introduction.* Springer, 2003.

[54] S. Balawi and J. L. Abot. The effect of honeycomb relative density on its effective in-plane elastic moduli: An experimental study. *Comp. Struct*, **84**, 2008.

[55] University of Virginia SEAS. Periodic cellular materials:topology (website). *http://www.ipm.virginia.edu/newres/pcm.topo/* , last accesed: 03/03/2012.

[56] G. Károlyi. Private Communication. *Department of Civil Engineering Mechanics, Technical University of Budapest, Müegyetem rpk. 3, H-1521 Budapest, Hungary.*

[57] B. W. Rosen. *Fibre Composite Materials.* American Society for Metals, 1965.

[58] C.D. Babcock A. M. Waas and W.G. Knauss. A Mechanical Model for Elastic Fiber Microbuckling. *J. App. Mech.*, **57**, 1990.

[59] W. H. Francis. *MSc Thesis:Mechanics of Post-Microbuckld Compliant Matrix Composites.* University of Colorado, 2008.

[60] L. J. Gibson, K.E. Eastering, and M.F. Ashby. The structure and mechanics of cork. *Proc. R. Soc. London. Ser. A.*, **377**:99–117, 1981.

[61] B. Moore, T. Jaglinski, D. S. Stone, and R. S Lakes. On the bulk modulus of open cell foams. *Cell. Polym.*, **26**:1–10, 2007.

[62] P. Vukusic and J. R. Samples. Photonic structures in biology. *Nature*, **424**:852–855, 2003.

[63] K. Dwarak. *Optomechanics of two- and three-dimensional soft photonic crystals*. Univ. Illinois, 2011.

[64] Y. Seung-Man. Patterned polymer photonic crystals using soft lithography and holographic lithography. *Synth. Metals.*, **148**:99–102, 2005.

[65] N. D. Lai et al. Fabrication of two- and three-dimensional periodic structures by multi-exposure of two-beam interference technique. *Opt Express.*, **13**:9605–9611, 2005.

[66] J. H. Hubbell. Common volume of two intersecting cylinders. *J. Res. Nat. Bur. Stan. C*, **69C**, 1965.

[67] T. L. Heath. *The method of Archimedes*. Dover, NY, 1953.

[68] L. Bauer, H. K. Keller, and E. L. Reiss. Multiple eigenvalues lead to secondary bifurcation. *SIAM Review*, **17**:101–122, 1975.

[69] H.M. Jaeger, S.R. Nagel, and R.P. Behringer. Granular solids, liquids and gases. *Rev. Mod. Phys.*, **68**:1259 – 1273, 1996.

[70] P.M. Reis, T. Sykes, and T. Mullin. Phases of granular segregation in a binary mixture. *Phys. Rev. E*, **74**, 2006.

[71] J.M. Ottino and D.V. Khakhar. Mixing and segregation of granular materials. *Ann. Rev. Fluid Mech*, **32**:55–91, 2000.

[72] E.B. Herbold. Tunable frequency band-gap and pulse propagation in a strongly nonlinear diatomic chain. *Acta Mech.*, **205**:85–103, 2009.

[73] R. L. Doney. Energy partitioning and impulse dispersion in the decorated, tapered strongly nonlinear granular alignment. *J. Appl. Phys.*, **106**, 2009.

[74] V. F. Nesterenko. Energy trapping and shock disintegration in a composite granular medium. *Phys. Rev. Lett.*, **96**, 2006.

[75] R.S. Elliott. Reversible stress-induced martensitic phase transitions in a bi-atomic crystal. *J. Mech. Phys. Sol.*, **59**:216–236, 2011.

[76] K. Bertoldi, F. Göncü, J. Shim, J. Cusack, S. Luding, T. Mullin, and S. Willshaw. Deformation induced pattern transformation in a soft granular crystal. *Soft Matter*, **7**:2321 – 2324, 2011.

[77] K. Bertoldi. Private Communication. *School of Engineering and Applied Sciences, Harvard University, Cambridge, MA 02138, USA*.

[78] S. Luding and Fatih Göncü. Private Communication. *Multi Scale Mechanics, University of Twente,7500 AE Enschede, Netherlands.*

[79] F. Göncü. Mechanics of granular materials: Constitutive behavior and pattern transformation. *PhD Thesis*, Submission Pending.

[80] A. Hazel. Private Communication. *School of Mathematics, Manchester University, Manchester, UK.*